8-2004

A Study of Charging in the Presence of a Gaseous Environment

Xiaohu Tang
University of Tennessee - Knoxville

Recommended Citation

Tang, Xiaohu, "A Study of Charging in the Presence of a Gaseous Environment. " PhD diss., University of Tennessee, 2004.
https://trace.tennessee.edu/utk_graddiss/2248

To the Graduate Council:

I am submitting herewith a dissertation written by Xiaohu Tang entitled "A Study of Charging in the Presence of a Gaseous Environment." I have examined the final electronic copy of this dissertation for form and content and recommend that it be accepted in partial fulfillment of the requirements for the degree of Doctor of Philosophy, with a major in Materials Science and Engineering.

David C. Joy, Major Professor

We have read this dissertation and recommend its acceptance:

Anthony J. Pedraza, R. A. Buchanan, Bin Hu, J. E. Spruiell

Accepted for the Council:
Dixie L. Thompson

Vice Provost and Dean of the Graduate School

(Original signatures are on file with official student records.)

To the Graduate Council:

I am submitting herewith a dissertation written by Xiaohu Tang entitled "A study of charging in the presence of a gaseous environment." I have examined the final electronic copy of this dissertation for form and content and recommend that it be accepted in partial fulfillment of the requirements for a degree of Doctor of Philosophy, with a major in Materials Science and Engineering.

David C. Joy

Major Professor

We have read this dissertation
and recommend its acceptance:

Anthony J. Pedraza

R. A. Buchanan

Bin Hu

J. E. Spruiell

Accepted for the Council:

Anne Mayhew

Vice Chancellor and
Dean of Graduate Studies

(Original signatures are on file with official student records.)

A STUDY OF CHARGING IN THE PRESENCE OF A GASEOUS ENVIRONMENT

A Dissertation Presented for the Doctor of Philosophy Degree
The University of Tennessee, Knoxville

Xiaohu Tang
August 2004

DEDICATION

This dissertation is dedicated to my parents, Keqin Tang and Renyuan Pi, great role models, and the rest of the family, for consistently supporting me, inspiring me, and encouraging me.

ACKNOWLEDGMENTS

I would like to thank my parents for their consistent support and encouragement these years. I specially express my deepest appreciation to my advisor, Dr. David C. Joy, for his patient, friendly, and unfailing support over the past four years. He inspired me in my research with his brilliant ideas and enthusiasms. I also want to thank my committee members Dr. R. A. Buchanan, Dr. J. E. Spruiell, Dr. A. J. Pedraza, and Dr. Bin Hu for their highly support and instructive on my thesis.

I wish to thank everybody in our group, and the unforgettable time with them. Truly thanks to Jing He, and Satya M. Prasad for their sincere help. I would like to thank Dr. Carolyn for her grand help, and to Jennifer Trollinger for her kindness. Thanks to Dr. Yeong-Uk Ko, Young Choi, Alexander Thesen, Toshihide Agemura, Jihoon Kim, Wei Li, and Yinghong Lin for their support.

I would also like to thank Yang Liu for her encouragement and support.

ABSTRACT

Charge accumulation in insulating or semiconducting samples due to electron beam irradiation is one of the key problems in electron microscopy. One of the most promising techniques for reducing the severity of such charging is to surround the sample with a low-pressure atmosphere of a gas. The charging behavior of a number of materials, surrounded by a variety of gases, has been determined to identify the important factors which control charging under these conditions. The magnitude of the surface potential was deduced from an analysis of X-ray spectra from the surface. The relationship between surface charge, gas pressure, and gas type are measured, and the charging reduction efficiency (CRE) is compared.

In addition, the use of localized gas jets to alleviate charging without causing beam broadening has been investigated. The gas distribution emanating from the pipe is simulated by a molecular dynamics Monte Carlo model. The effect of the pipe shape on gas distribution is studied. A method to obtain a desired gas distribution by optimizing the gas jet arrangement is proposed.

As a part of this thesis, a simple technique which provides a rapid way of visualizing charging phenomena is described and its spatial characteristics is examined. The migration of small particles to form a Lichtenberg image is driven by the surface potentials, which are a direct function of the distribution of high-energy electrons at the surface. The Lichtenberg patterns qualitatively and quantitatively demonstrate the distribution of the surface electric field resulting from the surface charging. The combination of the PPM, nanoparticles, and the Lichtenberg technique might permit high-resolution direct metal imprinting.

TABLE OF CONTENTS

LIST OF TABLES

LIST OF FIGURES

LIST OF SYMBOLS

A	Scanning area
C	Capacitance of the surface-charging layer
$\overline{c'^2}$	Mean value of the square of the thermal velocity components
d	Gas path length
d_m	Mass density
d_p	Thickness of negative charge layer
d_s	Thickness of positive charge layer
$\overline{d}$	BSE path length
E_{DH}	Duane-Hunt limit
E_0	Incident electron energy
E_2	Beam energy for charge balance
e	Electron charge
e_{int}	Specific energy associated with the internal modes
g_i	The radiation-induced conductivity
I'	Total electron current induced by electric field
I_P	Primary beam current
I_p'	Total ion current generated by PE
I_s'	Ion current generated by SE
I_{SC}	Specimen current
i_l	Leakage current
j_p	Primary electron current density
K_n	Knudsen number
k_B	Boltzmann constant
l	Characteristic flow dimension
M	Magnification
m	Number of collisions experienced by an electron
m_p	Mass of the particle
N	True count rate to calculate
N_A	Avogadro’s number
N'	Measured count rate
Q	Charge
P	Gas pressure
P^*	Gas pressure for charge balance
R	Depth of electron penetration
R_s	Resistivity of insulator
r	Position vector

r_s	Beam radius duo to gas skirt
S_{BSE}	Ionization efficiencies of BSE
S_{PE}	Ionization efficiencies of PE
T	Temperature
T_{int}	Internal temperature
T_{tr}	Translational kinetic temperature
t	Time
U	Overvoltage
U_{C_2}	The secondary critical energy where s is equal to unity
V	Peculiar velocity
v	Molecular velocity
Z	Atomic number of the gas
z	Sample thickness
V_s	Potential from the surface
V_m	Potential from the bulk
a	Townsend's first ionization coefficient
b	Number of ion pairs per unit path length per unit gas pressure by PE
b'	An ionization efficiency corresponding to electron with lower energy than PE
g	Electron emission ratio due to ion impact in unit time from surface
d	Secondary electron emission coefficient
d_{BS}	SE yield by backscattered electron
d_P	SE yield by incident beam
d_q	SE yield at sample tilt angle q
d_0	SE yield at normal incidence
e	Relative permittivity of the dielectric
e_0	Permittivity in vacuum
h	Backscattered electron emission coefficient
q	Sample tilt angle
k	Electrical conductivity
l	Gas mean free path
l_{swl}	Short wave cutoff
l_T	Townsend second ionization coefficient
r	Dose density
r_m	Molecular density
r_T	Resistivity
r_+	Positive charge density
r_-	Negative charge density
s	The sum of the backscattered electron and secondary electron coefficients
t	Dead time in seconds
j	Angular variable in cylindrical coordinates

Ω	The unit of resistivity
x	Number of internal degrees of freedom

Abbreviations

BSE	Backscattered electron
CRE	Charging reduction efficiency
MFP	Mean free path
PE	Primary electron
PLA	Pressure-limiting aperture
RND	Random number
SE	Secondary electron
WD	Working distance

CHAPTER I INTRODUCTION

1.1 *Why SEM?*

Scanning electron microscopes (SEMs) are widely used in many fields due to their features like high resolution, large depth of field, easy operation, and easy sample preparation, et al. These days, SEMs are especially essential to the semiconductor industry – 2 out of every 3 SEMs works in an area associated with device manufacture. The SEM is the best available tool for the characterization of semiconductor materials, which offers increased resolution capability in comparison to optical microscopy and is a commonplace technique for inspection and dimensional measurements (metrology) of circuits [Postek et al. 1987][Larrabee et al. 1993][Scarce 1994]. Many different modes of operation are important including Electron Beam Induced Current (EBIC), Cathodic Luminescence (CL), and voltage contrast. The form of the incident electron interaction with solid is listed in figure 1.1.

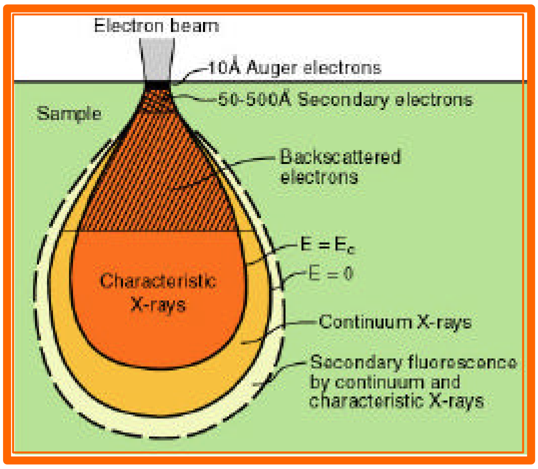

Figure 1.1 The interaction volume of electron beam with solid and the related signals

1.2 Problems in Conventional SEM

Conductors, semiconductors, and insulators comprise the entire spectrum of materials in the real world. Specifically to the semiconductor industry, the active device components are composed of semiconductors; conductors are extensively used for interconnection applications; insulators, most commonly polymers, are widely used as inter-level dielectrics and packaging materials for electronic equipment [Soane et al. 1989][MacDonald et al. 1989]. In biology and pharmaceutics, most of the samples are insulators. When charged particles irradiate insulator, dielectric, or semiconductor during various types of analytical techniques as Auger electron spectroscopy (AES), x-ray photoelectron spectroscopy (XPS), secondary ion mass spectroscopy (SIMS), electron probe microanalysis (EPMA), etc., the spectra received from insulators are badly distorted due to the electric field in the surface originating from the inequality between the incident particles and the emitted electrons, resulting the qualitative and quantitative errors in microanalysis [Jbara et al. 1997][Cazaux et al. 1992]. Such phenomena are usually called "charging effects" and occurs in a wide range of insulator materials like polymers, ceramics, glass, biological samples, even on many metals and semiconductors because they can be easily oxidized when exposed to air so as to form an insulating layer [Cazaux 1999]. Since the charged-up surface generates an electric field which will skirt the incident electron beam, the contrast of the image thus may become abnormal and unstable, and the resolution of the image may degrade [Witty et al. 1975][Shaffner et al. 1976][Pfefferkorn et al. 1972][Pawley 1972][Fuchs et al. 1978][Taylor et al. 1976]. Such instability leads to disturbance of the x-ray spectra making analysis impossible, the shifting of spectra on the energy scale gives difficulties in interpreting chemical states, and excessive charge may damage the sample [Pantano et al. 1981][Cros 1992][Pireaux et al. 1992]. In electron beam lithography, pattern placement error has been reported as the result of the resist charging [Bai et al. 1999]. Charging of the devices during scanning microscopy makes accurate metrology difficult because of the deflection of the electron beam by the electric field on the sample and a very small beam deflection around a feature can move the beam one or two pixel points and introduce substantial error into critical dimensions (CD) measurements. Figure 1.2 shows the negatively and positively charged surface on a photolithography mask respectively.

1.2.1 Charging Mechanism

There are many models that have been proposed to account for the origination of charging but most of them have the common feature is that the incident electrons interact with localized electrons or holes inside the band gap due to the impurities or structural defects, which are produced by irradiation or pre-exist inside the sample [Vigouroux et al. 1985]. Following are two commonly used models to explain the charging mechanism.

1.2.1.1 Electron Current Model

The theory of insulator charge-up under the bombardment of charged particles has been studied for a long time [Crawford 1979]. It is believed that the surface charging of insulators and semiconductors comes from the formation of space charge which is due to the incident electron trapping [Song et al. 1996]. Assume the current of the incident particle leaving the final aperture is equal to the current striking the sample surface as I_P, the specimen current I_{SC} is given by the charge conservation equation as

$$I_{SC} = I_P - I_{SE} - I_{BSE} \tag{1.1}$$

which only applies when the steady state is reached [Newbury 1976][Farley et al. 1990]. Here I_{SE} and I_{BSE} are secondary and back-scattered electron current respectively. Or this equation can be rewritten as

$$I_{SC} = I_P (1 - d - h) \tag{1.2}$$

d and h are the secondary and back-scattered electron yield coefficient respectively. But generally the sum of I_{SE} and I_{BSE} is treated as I_{SE} only, as figure 1.3 shows

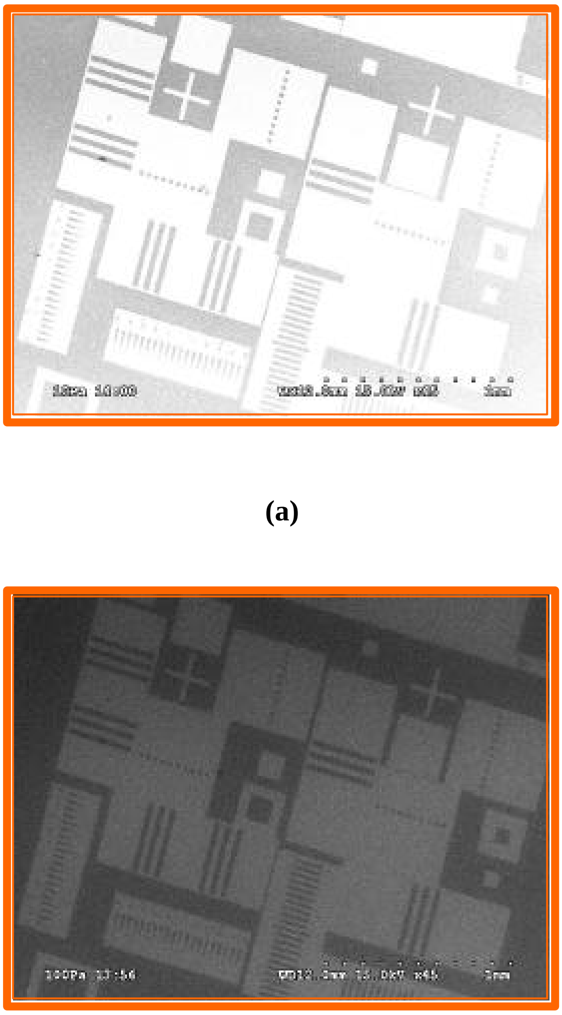

(a)

(b)

Figure 1.2 Comparison of the negative and positive charging on the surface of photolithography mask: (a) negative charging (b) positive charging

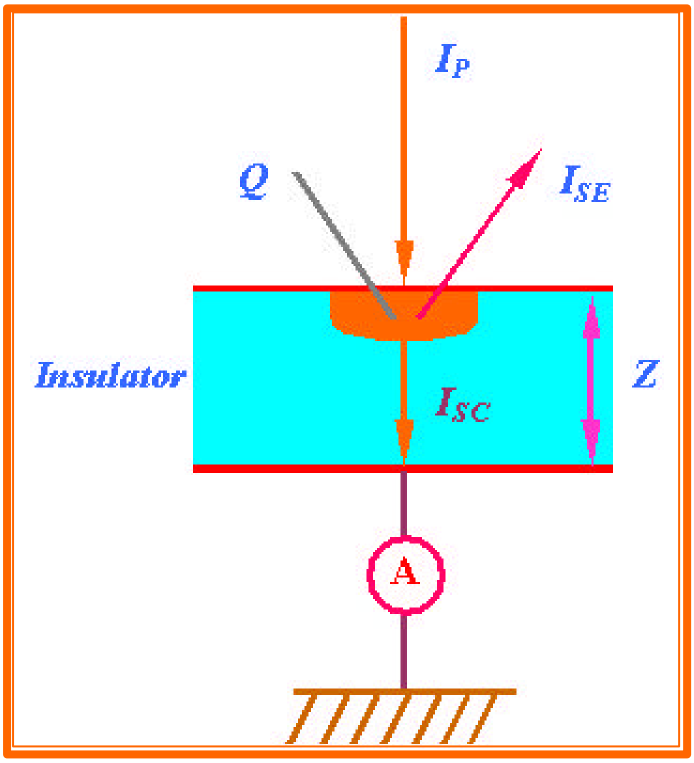

Figure 1.3 Schematically drawing the X-ray Photo-emission Spectroscopy (XPS) charging mechanism

.

The surface can obtain positive charging if the irradiation sources are positively charged particles (like protons) or neutral particles (x-ray photons) because the emitted particles from surface are mostly secondary electrons thus leave positive holes in the surface layer. In addition, the positively charged surface will attract the emitted secondary electrons so as to lower the SE yield, resulting a stable surface charging state.

When negative particles as electrons are used, the surface potential can be positively or negatively charged which depends on the incident electron energy E_0. As figure 1.4 shows, when $E_1 < E_0 < E_2$, where $d + h > 1$, the surface will be positively charged and will keep changing until the balance $d + h = 1$ is reached because the positive surface potential will increase the kinetic energy of the incident electrons and d will be affected by the variation of primary electron energy [Cazaux et al. 1992].

When E_0 is larger than E_2 or less than E_1, the surface potential is negative, which means the number of incident electrons is larger than that emitted. In this case the incident electrons are slowed down by the surface voltage so the secondary electron yield d increases, varying with the curve in figure 1.4. The variation of d helps to reduce the surface potential, so unlike the positive particle case, the surface potential can reach a large negative value. Assuming the specimen current is I_{SC} and treating the insulator as the capacitor media while the insulator surface and the grounded sample stage are the capacitor plates, the specimen current induced by charge conservation is then:

$$\frac{dQ}{dt} = I_{PE}(1 - d - h) - I_{SC} \qquad 1.3$$

here dQ/dt is the rate at which charge accumulates [Moncrieff et al. 1978]. With the charge growing (dQ/dt remains finite), the surface voltage keeps increasing until it reaches the dielectric breakdown voltage. The charge dissipates in the form of sample leakage current. Such charge and discharge processes continue alternatively. It is similar to the case of charge and discharge on a capacitor by external circuit. At this time, the specimen current is not stable but varies periodically.

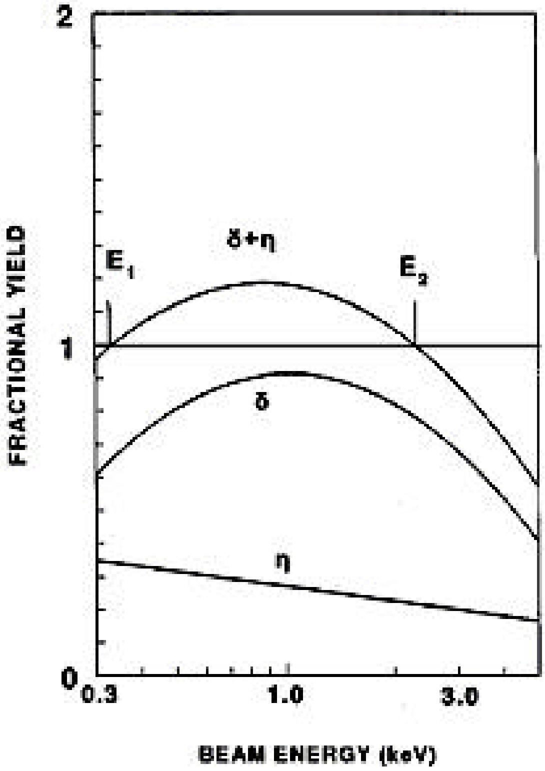

Figure 1.4 The total yield of electrons as the function of incident beam energy

But if the surface pertains stable state at a surface potential under the bombardment of charged particles (dQ/dt is zero), the specimen current observes the Ohm's law thus it can be measured as a fairly stable value. The surface potential V_s can be calculated as

$$V_s = Q/C = \frac{\int_0^t [I_{PE}(1-d-h) - I_{SC}]dt}{C} \qquad 1.4$$

here C is the capacitance of the surface-charging layer.

1.2.1.2 Dynamic Double Layer Model

The electron current model is based on the conservation of electron current but does not consider the fine structure of the surface. Figure 1.5 shows the general form of the charging distribution of an insulator which demonstrates how the double layer model works. The incident primary electrons are assumed to be enclosed in a homogeneously charged cylinder with charge Q_m, located at the depth R which is dependent on the primary electron beam energy, given by the following equation [Seiler 1982].

$$\frac{R}{nm} = \frac{1.15 \times 10^5}{d_m/(kg/m^3)} \left(\frac{E_{PE}}{keV} \right)^{1.35} \qquad 1.5$$

here d_m is sample mass density, E_{PE} is the primary electron energy. R also can be evaluated from a power law of the form

$$R(nm) = CE_0^n(keV) \qquad 1.6$$

where n is often chosen to be ~5/3 or $n = 1.7$, and C is a material constant [Reimer 1985][Cazaux 2001].

It is assumed that the secondary electrons are all emitted from a cylindrical volume close to the insulator surface, leaving a homogeneous charging layer with the positive charge Q_s. The potential distribution $V(z)$ along the incident axis can be obtained by the electrostatics laws. The charge in each cylinder contributes to the surface potential V_s and the potential V_m at the

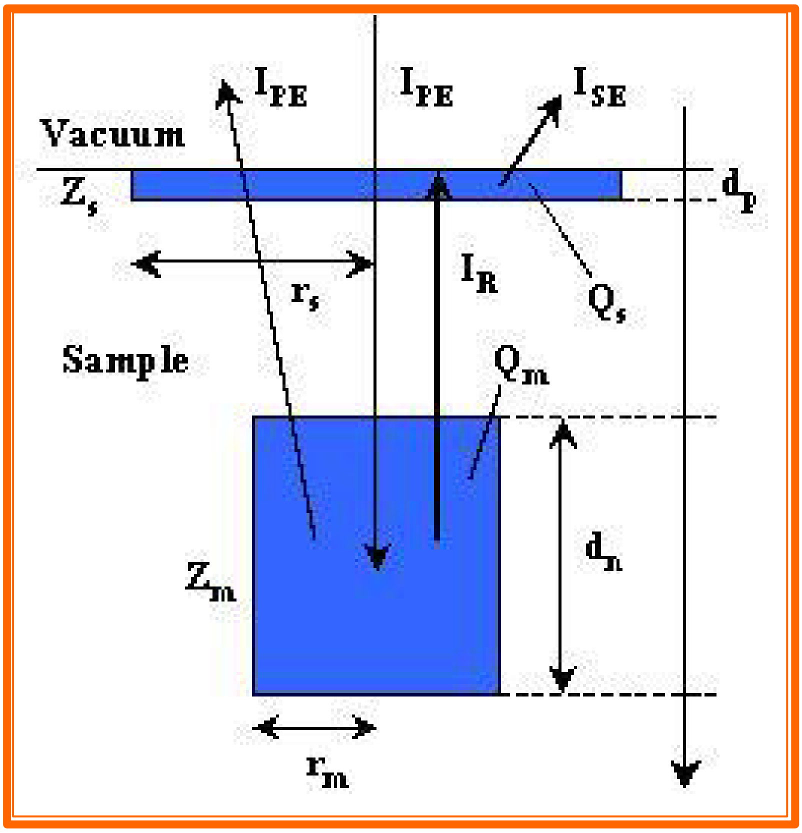

Figure 1.5 Schematically drawing of charge distributions and electron currents in the double layer model

maximum penetration depth of the primary electron R. The variation curves of V_s, V_m, and the sum of them as V_z are plotted in figure 1.6.

$$\begin{aligned} V_s &= \frac{Q_s}{C_{11}} + \frac{Q_m}{C_{12}} \\ V_m &= \frac{Q_s}{C_{21}} + \frac{Q_m}{C_{22}} \end{aligned} \qquad 1.7$$

The capacity coefficients C_{ij} in equation 1.7 are the functions of the geometry parameters and the dielectric constant of the double-charged layers. Here the double layer charge distribution with the positively charged layer is larger than that of the negatively charged layer in the insulator surface. Such phenomena can be explained by the role of the backscattered electrons. The positively charged layer of the surface is the result of the emitted secondary electrons and the contributions to the SE yield are considered as: the SE_1 electrons d_P, induced by the incident electron beam PE entering into the sample; the SE_2 electrons d_{BS}, induced by the backscattered electron BSE emitted out of the specimen, accounts for 40% to 80% secondary electrons emission. Then the secondary electron yield has the following form

$$d = d_P + d_{BS} \qquad 1.8$$

where d_{BS} is proportional to the backscattered electron yield h, $d_{BS} = hd_p$. Figure 1.7 schematically shows the source of secondary electrons [Cazaux 2004].

The positive charge layer created by SE excitation will spread into a relatively wider region since the backscattered electrons can reach the surface over a range larger than the primary electron beam diameter. On the contrary, the lateral dimension of the negatively charged layer, which comes from the trapped primary electrons, is determined by the primary electron scattering inside the insulator.

Another important feature of this model is the time dependent charging behavior. It assumes that only the charges are time dependent, not the geometry parameters, thus the variation of charging vs. time is in equation 1.9 [Melchinger et al. 1995].

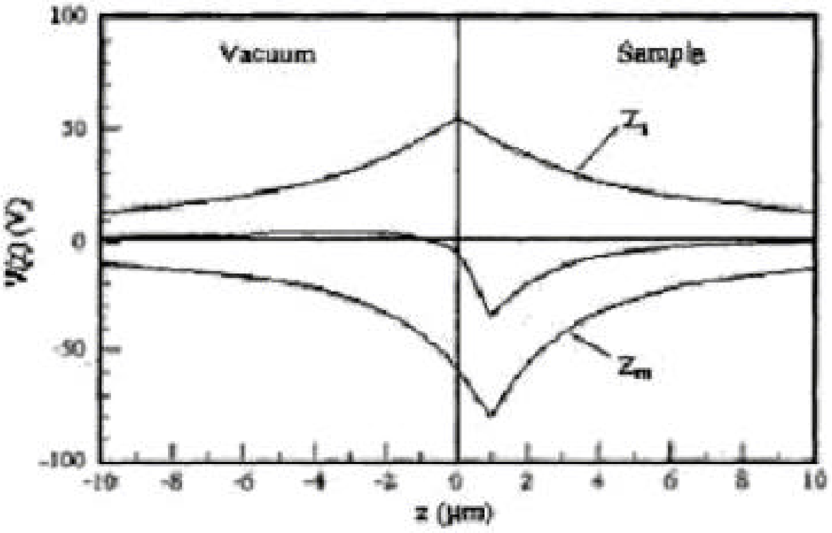

Figure 1.6 Calculated potential V_z of an insulator and charge distribution as shown in figure 1.5

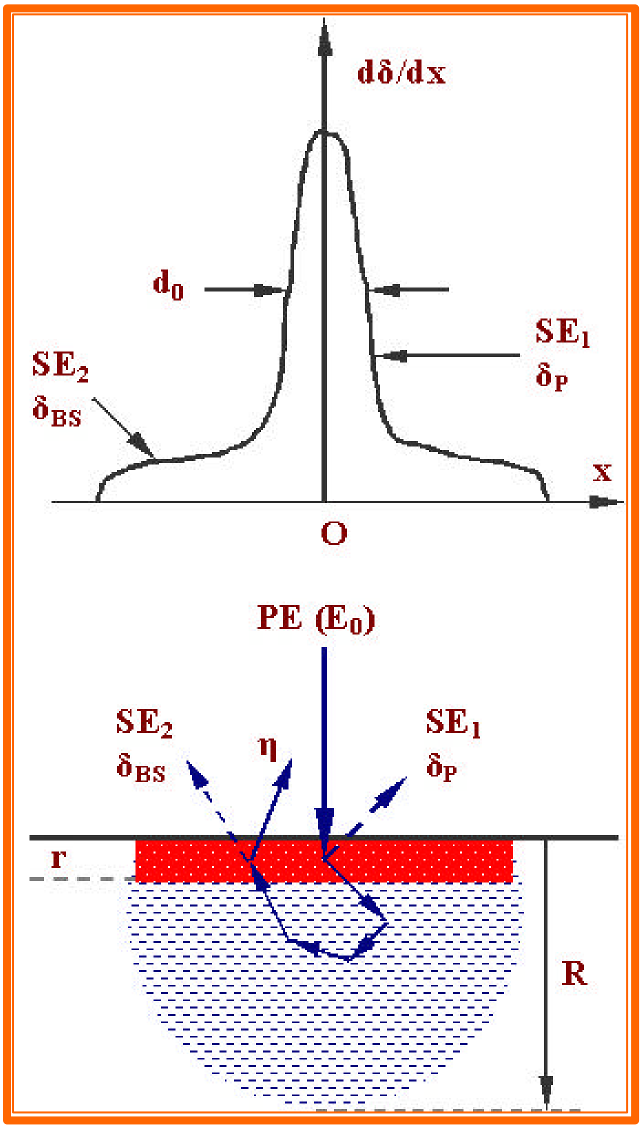

Figure 1.7 Upper drawing schematically shows the distribution of secondary electron emission with the SE_1 contribution due to the direct excitation of primary beam and the SE_2 contribution due to the backscattered electrons. Bottom drawing is the sketch of the charging distribution with the excess positive charges in the surface region with thickness r, and the excess negative charges within the depth of r and R.

$$
\begin{aligned}
\frac{dQ_s}{dt} &= -I_{SE}(Q_s, Q_m) + I_R(Q_s, Q_m) \\
\frac{dQ_m}{dt} &= +I_{PE} - I_{BSE} - I_R(Q_s, Q_m)
\end{aligned} \qquad 1.9
$$

1.2.2 Methods to Alleviate Charging

There are many methods have been reported to alleviate the charging phenomena under SEM observation on insulator or semiconductor sample. Coating a thin metal layer on the sample surface is an effective way to alleviate charging because it drains away charge to the grounded specimen stage, but the coating may reduce topographic and chemical composition contrast, and obscure crystallographic channeling or electron backscatter patterns [Moncrieff et al. 1978][Ichinokawa et al. 1974]. Reducing the incident beam energy is another possible solution to charging since this can increase the SE yield from the sample until the charge injected by the beam is balanced by the charge (SE+BSE) emitted by the sample [Ichinokawa et al. 1974][Cazaux 1999][Joy et al. 1996]. However, lower beam energies may result in poorer resolution, and there are some practical problems in applying this method to an inhomogeneous surface [Newbury 2002]. Surface pre-irradiation by x-rays can increase the entire specimen volume conductivity so as to decrease the charging effect, but it is only successful in cases where metals are freed by photolysis [Pfefferkorn et al. 1972]. Surface charge-up also can be controlled by a beam of very low energy ions in real time [Crawford 1979]. The advantages of this method include: ion independence of the nature of the insulating surface, no sputtering effect on surface, not ion flow to the secondary collector. On the other hand, the drawbacks are also obvious: not as effective for buried charge effects, unwanted instrumental interactions. By placing a conductive grid above the sample surface, the surface charging can be alleviated in some degree [Newbury 2000]. A practical solution to such problems is to surround the sample with a low-pressure gas, and the principle is based on the surface charge neutralization by the ionized gaseous particles

[Pfefferkorn et al. 1972][Tang et al. 2003][Robinson 1975a]. Nowadays the development of the VP-SEM (variable pressure SEM) and ESEM (environmental SEM) permits the SEM working pressure up to 1000Pa, which makes this method as a fast, convenient, easy-operating way to reduce the surface charging. The mechanism is suggested as the continuous discharge of the surface charging by ionization current from the interaction between electrons and gas molecules [Moncrieff et al. 1978][Bolon et al. 1989]. This is discussed in detail in chapter II.

CHAPTER II VP-SEM

2.1 How does the VP-SEM Work?

Figure 2.1 schematically shows the relationship between incident beam energy and surface charging under vacuum condition and a fixed gas pressure, which indicates that the gas inside the chamber plays an important role on the charging behavior. At all incident beam energies the presence of a gaseous atmosphere reduces the surface potential from typically thousands of volts to just a few hundred volts. Similar observations have also been made in X-ray Photoelectron Spectroscopy (XPS) experiments, which indicates the peak shape and peak position are dependent on gas pressure [Yu et al. 1990].

Figure 2.2 indicates the geometry generally employed in VP-SEMs, the use of the differential pumping systems and pressure-limiting apertures (PLA) makes the scanning electron microscopes work under the gaseous environment in the range of 1 to 270 Pa (for Hitachi S-3500N) or even higher, up to 1000Pa (for Hitachi S-4300SE/N), while the electron gun and column remains at high vacuum (<0.13mPa) [Danilatos 1988]. There is a positively biased ring electrode located right above the sample and centered on the one side of the objective lens in order to preserve and amplify the secondary electron signals (as figure 2.2 shows). The neutralization of the negative surface charging by gas ionization is supposed to take place by a flow of positive ion current towards the surface by the electric field which is composed by the electrode bias and the surface voltage [Moncrieff et al. 1978]. The GPL (gas path length) is defined as the distance between the PLA (pressure limit aperture) and the specimen surface. Possible ionization events are given in figure 2.2 and the initiating particles can be (1) primary electron (2) back-scattered electron (3) secondary electron (4) the positive ions liberated by gas ionization. Suppose each ionization collision produces a secondary electron and a positive ion. At equilibrium, the charged particles inside the SEM chamber can be (1) PE (2) BSE (3) SE by PE

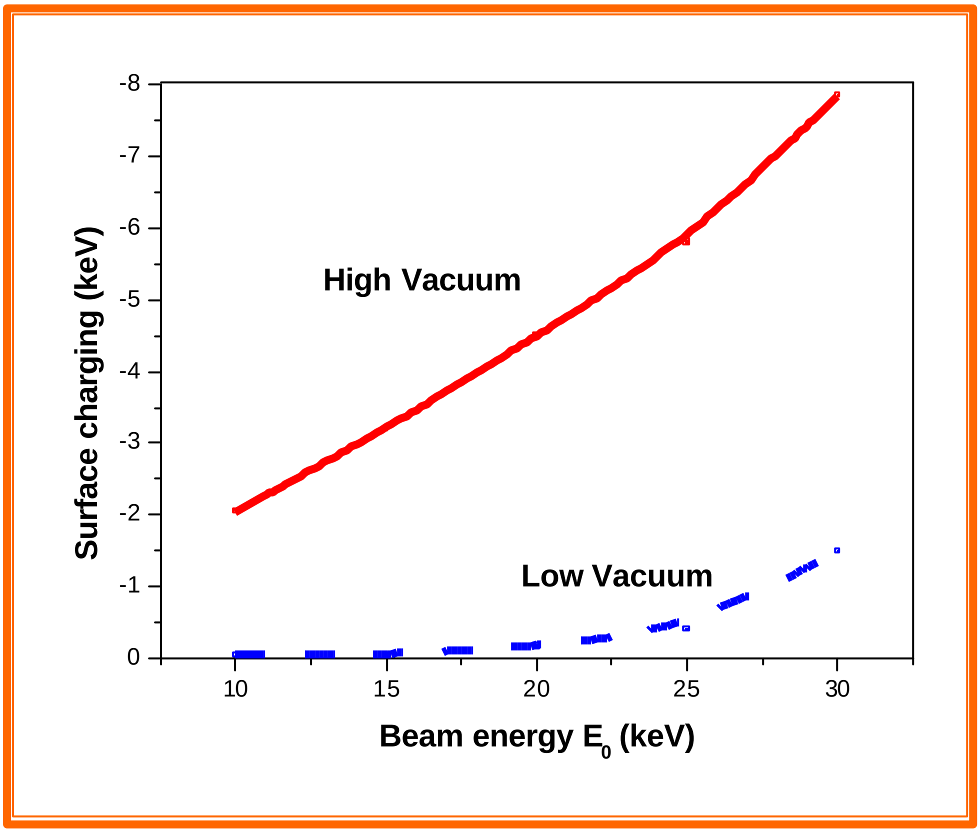

Figure 2.1 The experimental dependence of incident beam energy and surface charging in vacuum and fixed gas pressure for mica (4×2× 0.2cm). The acquisition time for the x-ray spectrum was 100 seconds. The electric resistivity of mica is 1E+16Ω·m (CRC materials Science and Engineering Handbook). The plate electrode of the SE detector is present inside the chamber with 250volts bias voltage in standard SE mode (SSE).

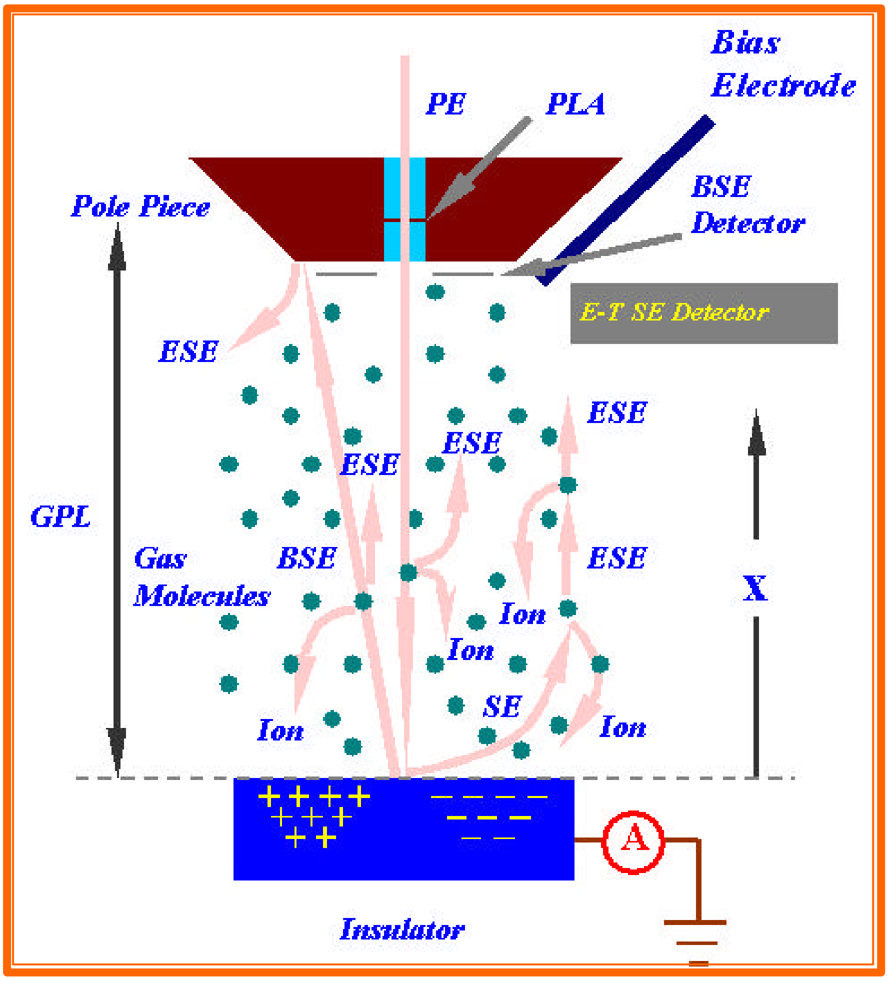

Figure 2.2 Schematic diagram of ionizing collisions in a low-pressure gas above a charged non-conducting specimen.

impacting surface (SE1) (4) SE by BSE impacting surface (SE2) (5) SE by PE ionizing gas (ESE1) (6) SE by BSE ionizing gas (ESE2) (7) SE by positive ion ionizing gas (ESE3) (8) SE by SE ionizing gas (ESE4) (9) SE by BSE hitting pole piece (ESE5). Further ionization events continue because each ionizing collision produces a low energy electron which can be accelerated by the electric field existing above the specimen until its energy is larger than the critical ionization energy of gas molecule and forms the gas ionization cascade. This process has been proved to be an effective way to alleviate charging and has been used in semiconductor inspection and metrology [Mathieu 1999][Postek et al. 2004].

Assume each accelerated electron generates a ion pairs per unit length in direction x (figure 2.2). When the saturated current condition is reached

$$dI'/dx = aI' \tag{2.1}$$

here I' is the total electron current induced by electric field. The electron current $I'(x)$ at a position x is then

$$I'(x) = I'(0)\exp(ax) \tag{2.2}$$

where $I'(0)$ is the electron current at $x = 0$, a can be taken as the Townsend's first ionization coefficient when the specimen surface and the SEM chamber are treated as the two parallel electrode plates in the Townsend theory of electrical breakdown in gas [Townsend 1915].

Suppose each primary electron generates b ion pairs per unit path length per unit gas pressure, the increment of a primary current I'_p due to the gas ionization at each point x' will be

$$dI'(x') = -I'_p bPdx' \tag{2.3}$$

where P is the gas pressure, the negative sign means dx' is in the opposite direction to dx, and the electrons produced in this increment will involve in the multiplication process described in equation 2.2. The increment of electron from x' to x will be

$$dI'(x) = -I'_p bPdx' \exp[a\,(x - x')] \tag{2.4}$$

The ionization events occur within the distance of the specimen surface and the PLA, or gas path length (GPL). Under saturation conditions, the total electron current reaching the sample surface $I'(d)$ equals to the total ion current $I_p{}'$ generated by the primary beam.

$$I'_p = I'(d) = -\int_d^0 I'_p bP \exp[a\,(d - x')]dx' = \frac{I'_p bP}{a}[\exp(ad) - 1] \qquad 2.5$$

where d is the gas path length (GPL).

The secondary electrons produced by the primary electron striking on the specimen surface are also contributed to the ionization process as the type of equation 2.2. The ion current $I_s{}'$ is equal to the net effect of the secondary electron current, that is

$$I'_s = I'(d) - I'(0) = I'_p d \exp(ad) - I'_p d = I'_p d[\exp(ad) - 1] \qquad 2.6$$

where d is the secondary electron yield coefficient.

Because the backscattered electrons pass through the same distance d (GPL) but follow the opposite direction of the primary beam, they have a similar effect on the ionization. The contribution of the BSE to the ion current is

$$I_{bs} = \frac{hI'_p b'P}{a}[\exp(ad) - 1] \qquad 2.7$$

here b' denotes an ionization efficiency corresponding to electron with lower energy than the primary electron.

The ion current reaching the specimen surface is determined by equations 2.5, 2.6, and 2.7

$$I_0 = I_p + I_s + I_{bs} \qquad 2.8$$

If the low-energy electrons released from the specimen surface by positive ion striking are considered as the process of equation 2.2, again released ions will start another process in an endless cycle. Hence, the total ion current is

$$I = I_0(1+g[\exp(ad)-1]+g^2[\exp(ad)-1]^2+...) = I_0\left(\frac{1}{1-g[\exp(ad)-1]}\right) \qquad 2.9$$

here g is the electron emission ratio due to ion impact in unit time from the specimen surface.

Assume the surface charging is counteracted by ion current, thus the surface charging equation is

$$\frac{dQ}{dt} = I_P\left(1-h-d-\frac{(1+g)A}{1-g[\exp(ad)-1]}\right) \qquad 2.10$$

$$A = d[\exp(ad)-1]+\left[(b+hb')\frac{P}{a}\right][\exp(ad)-1] \qquad 2.11$$

This formula indicates that such charging neutralization process is time-dependent [Moncrieff et al. 1978].

2.2 Limitations of VP-SEM

On the other hand, the drawbacks of gas inside the VP-SEM are as following: gas scatters and broadens the electron probe; reduces the current available for imaging and analysis; modifies the effect of the beam-sample interaction by adding secondary charge; limits the application of the secondary electron signal because the SEs are too low energy to travel through the gas.

The electron beam suffers collisions with gas molecules which can be separated into two categories: elastic collisions, whose consequences are to reduce the beam current within the focused probe and redistribute it to a wider skirt region, degrading the resolution and contrast; and inelastic collision, generating the continuous and characteristics x-rays from the gas atoms, which contribute to the measured x-ray spectrum [Moncrieff et al. 1979]. But the x-ray production from gas ionization is a relatively rare event [Newbury 2002]. The number of collisions m experienced by an electron varies as

$$m = GPL/l \qquad 2.12$$

here GPL is gas path length and l is the gas mean free path. The fraction of an electron beam reaching the sample surface without scattered is $\exp(-m)$. The Rutherford theory is used to estimate the mean scattering angle at the specimen surface [Danilatos 1988]

$$r_s = \frac{364Z}{E}\left(\frac{p}{T}\right)^{1/2} WD^{3/2} \qquad 2.13$$

here r_s is the skirt radius, Z atomic number of the gas, E beam energy, P gas pressure, T temperature, WD (working distance) is the beam path length in gas. Schematic drawing the beam skirt effect in figure 2.3 [Newbury 2002].

Equation 2.13 quantitatively describes some factors affecting the final probe size due to the gas skirt. The broadening varies as $P^{1/2}$, which means increasing gas pressure is not always good for image resolution though it is helpful to remove charging. The broadening is also inverse proportional to the beam energy, which makes the low-voltage operation difficult. The working distance is the most rapidly varying term, which affects the beam broadening as the gas path length $(GPL)^{3/2}$, so it must always be kept as small as possible. The amount of broadening is proportional to the atomic number of the gas. This is a guide to help us to choose the right gas for charge neutralization.

Above all, the limitations of VP-SEM are: a short working distance is essential; charge-induced contrast is absent; the image resolution is degraded; the contrast is low (the beam is skirted by gas) and the S/N ratio is poor (due to the ion signal). But VP-SEM still has the superior ability to observe insulator or other samples with low conductivity due to the convenience of operation and instrument.

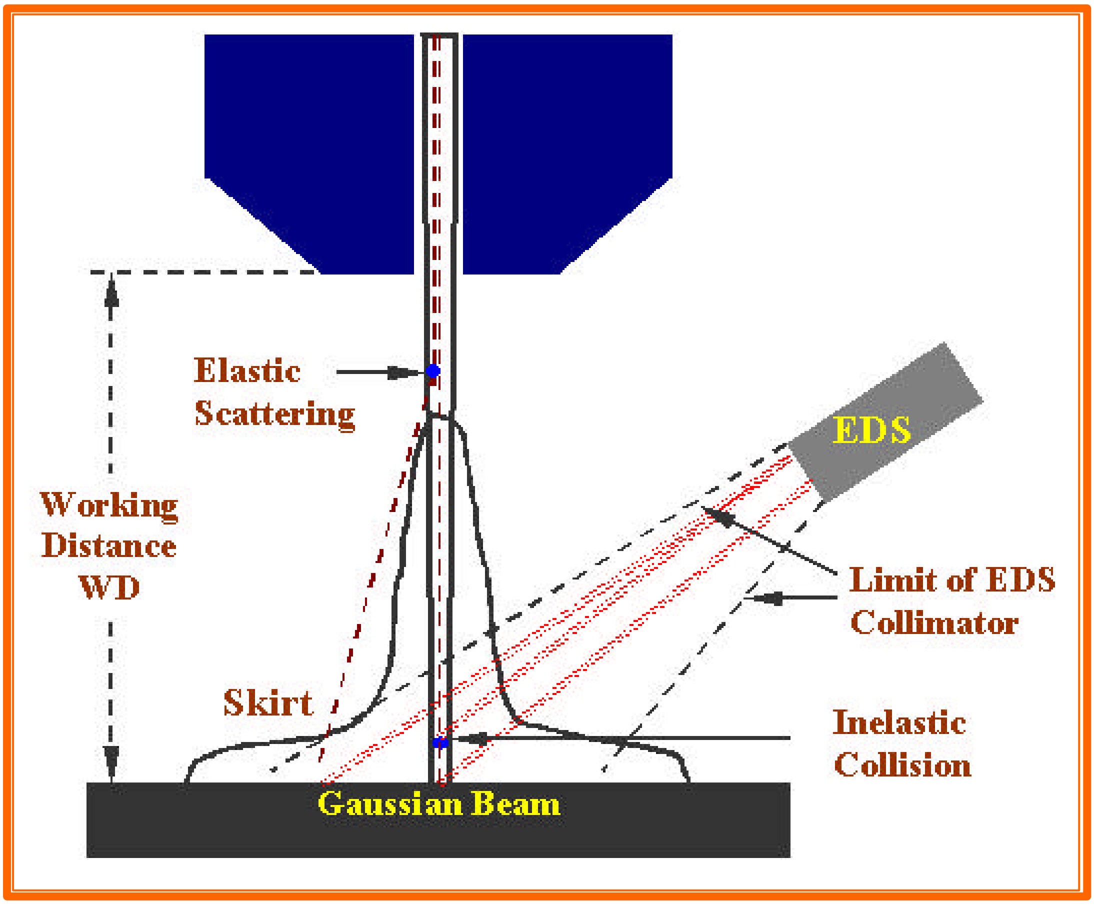

Figure 2.3 Schematically illustrate the formation of electron scattering skirt around the unscattered electron. Assume the average electrons are scattered at the midpoint of the gas path.

2.3 Quantitative Measurement of Surface Charging

The principles of the VP-SEM indicate that the sample surface charging is dependent on many factors, including SEM settings and introduced gas. Thus the quantitative measurement of the surface charging as the function of experimental parameters is critical to understand the mechanisms of charging so as to effectively alleviate the surface charging by optimizing instrumental parameters in many areas.

2.3.1 Mirror Effect

This method is based on the classic laws of electrostatics to determine the distribution of the voltage around the trapped charges, and the electron energy stored also can be evaluated. It is assumed that the impinged charge q as a point charge, which corresponding to the point scanning condition with no apparent charge diffusion around that point, is produced by an accelerating voltage V_0. The principles of measuring voltage distribution are schematically shown in figure 2.4 [Gressus et al. 1991].

If the accelerating voltage changes to V_1 and $V_1 < V_0$, the incident electron beam will be tilted, or even be reflected by the equipotential of the previously charged specimen. Such reflected electrons of the incident electron may hit one spot inside the SEM chamber, and the generated secondary electrons are collected by the secondary electron detector and form the image of the SEM chamber [Gong et al. 1993]. The trapped charges can be determined by such virtual images, and the potential V along the incident beam axis at a distance r from the surface is

$$V = \frac{K}{4\pi\varepsilon_0} \int_0^{\infty} \frac{\rho(x) 2\pi x dx}{\left(r^2 + x^2\right)^{1/2}} \qquad 2.14$$

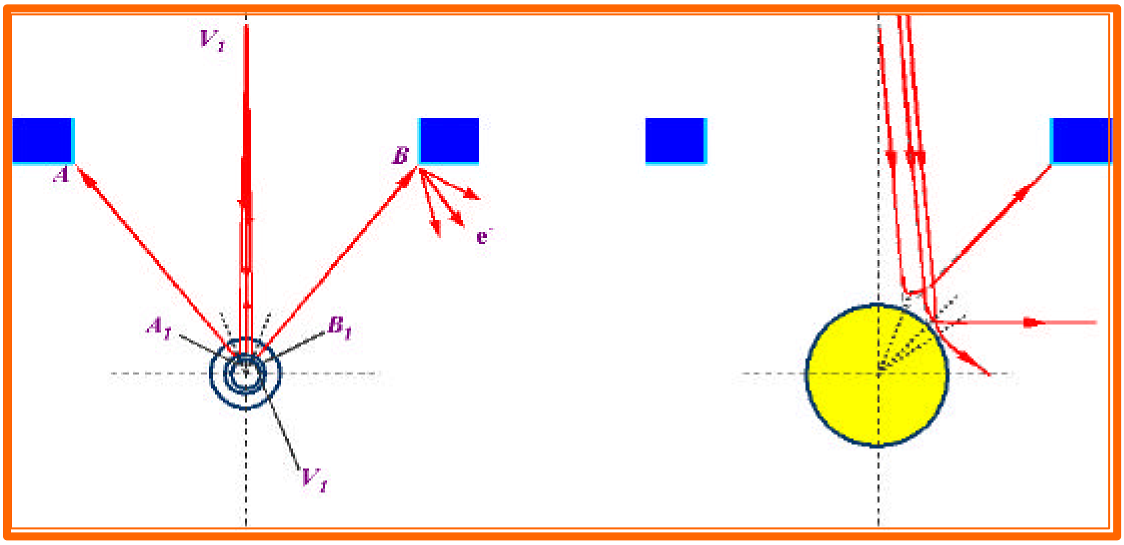

Figure 2.4 Schematically drawing the principle of mirror effect

where $K = 2e_0/(e + e_0)$ is the effective static dielectric constant, $r(x)$ the radial density of charge per unit area at a distance x from the axis, e and e_0 are the relative permittivity of the dielectric and the permittivity in vacuum respectively. Meanwhile, assuming the charges are uniformly distributed inside the small volume, the total charge Q stored in the insulator is

$$Q = \int_0^\infty r(x) 2pxdx \qquad 2.15$$

This method is commonly used in a conventional scanning electron microscope, but also can be applied in an Auger scanning microscope provided it has a functioning optical column [Le Gressus et al. 1992]. The problem of this method is that the trapped charges could diffuse and the shape of equipotential field is not as of sphere as model described. So the use of the Coulomb's law is not very appropriate until the field is located very far away, at which is almost impossible to obtain the mirror image of field at low accelerating voltage [Gong et al. 1993]. Figure 2.5 shows the virtual images of the lens aperture of the scanning microscope by mirror effect [Le Gressus et al. 1991].

2.3.2 Electron Spectroscopy Energy Shift

In surface analysis, the observed charging effects are the shift of the energy and peak distortion of the characteristic (photo and Auger) electron lines. They are independent of the experimental techniques and only related to the specimen itself. The surface potential V_s measured by the Auger Electron Spectroscopy (AES) comes from the energy shift ΔE, which is defined as the difference between the energy value of measured Auger peak line and the standard Auger peak value as figure 2.6 shows.

The surface voltage thus can be determined by

$$\Delta E = -eV_s \qquad 2.16$$

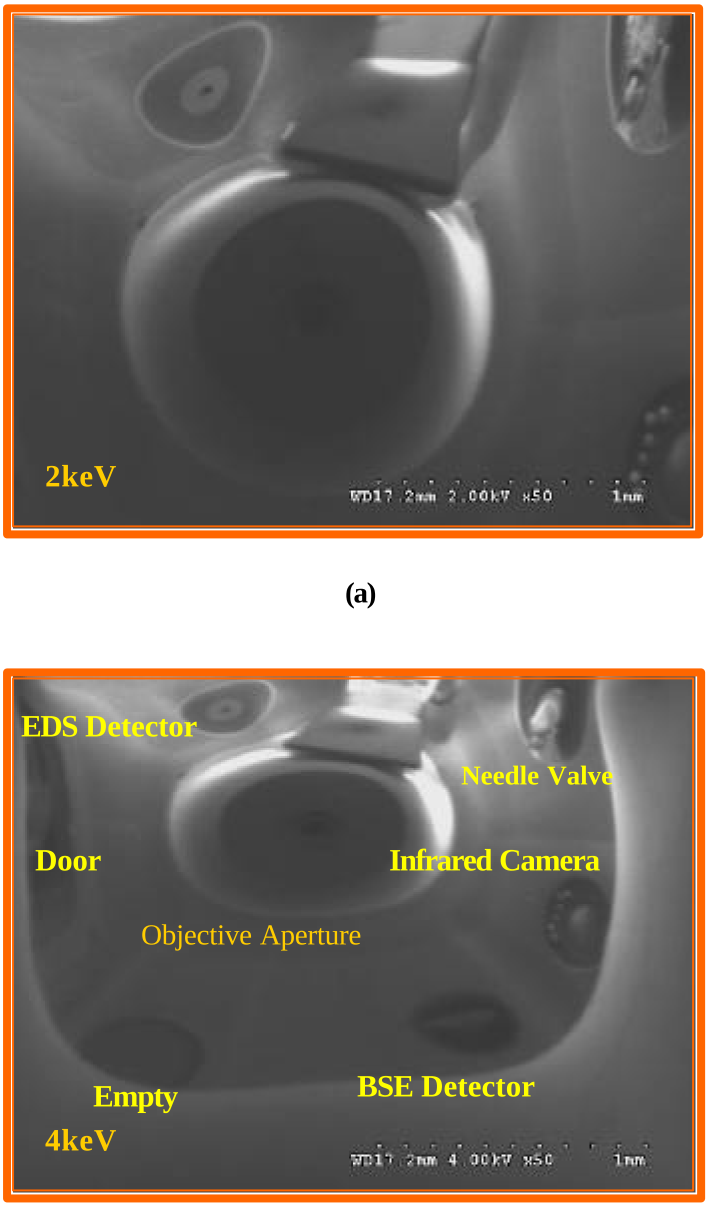

(a)

(b)

Figure 2.5 Virtual images of the microscope chamber were taken under the mirror effect. Quartz is pre-irradiated by 15keV beam energy with magnification 50×, and then imaged by decreasing beam energies to (a) 2keV and (b) 4keV respectively after 10 seconds pre-irradiation.

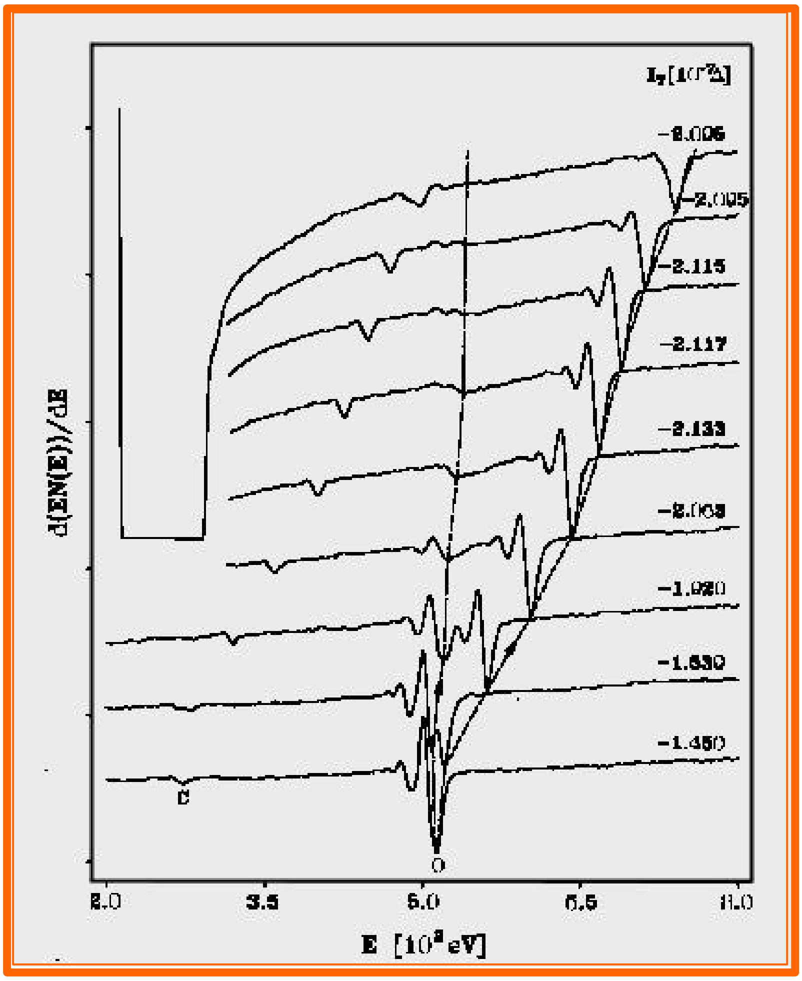

Figure 2.6 The splitting of the O $KL_{2,3}L_{2,3}$ peak at the start of charging on Al_2O_3. Sample is bombarded with 2keV electrons at normal incidence [Guo et al.1997].

here e is the electron charge, ΔE is the peak shift value, V_s the surface voltage, the negative symbol means that the positive value of ? E corresponds negative surface potential [MacDonald et al. 1976]. According to Hofmann [Hofmann 1992], the surface charging potential in AES can be expressed as:

$$V_s = \left(I_{PE} - I_{SE}\right) \times R \text{ or } V_s = r \times z \times j_p \left(1 - d\right) \qquad 2.17$$

where V_s is the surface charge potential, I_{PE} beam current, I_{SE} total secondary emission current, R is the resistivity of insulator, z sample thickness, j_p primary electron current density, d is the secondary emission coefficient.

From the X-ray Photoelectron Spectroscopy (XPS) measurement, the surface charge is reflected from the deviations of photoelectron peak position, peak width, and peak area when comparing the charged and standard spectra [Cazaux 1999][Yu et al. 1990][Baer et al. 2002].

2.3.3 Image Distortion

The distortion images are frequently observed on a charged up surface, and increase with the scanning time. Figure 2.7 schematically shows how to quantitatively measure the surface potential by image distortion [Ichinokawa et al. 1974].

Here the distortion originates from the deflection of the incident beam by the surface electric field. The points 1, 2, and 3 correspond to surface potential of negative, zero, and positive, respectively. By using a copper grid above the aluminum plate with an adjustable external battery, the calibration curve of the surface potential V_s and the image displacement d can be obtained. Then replacing the copper grid by insulating specimen and with the same arrangement, the surface potential V_s can be determined by the measured image displacement d from the calibration curve.

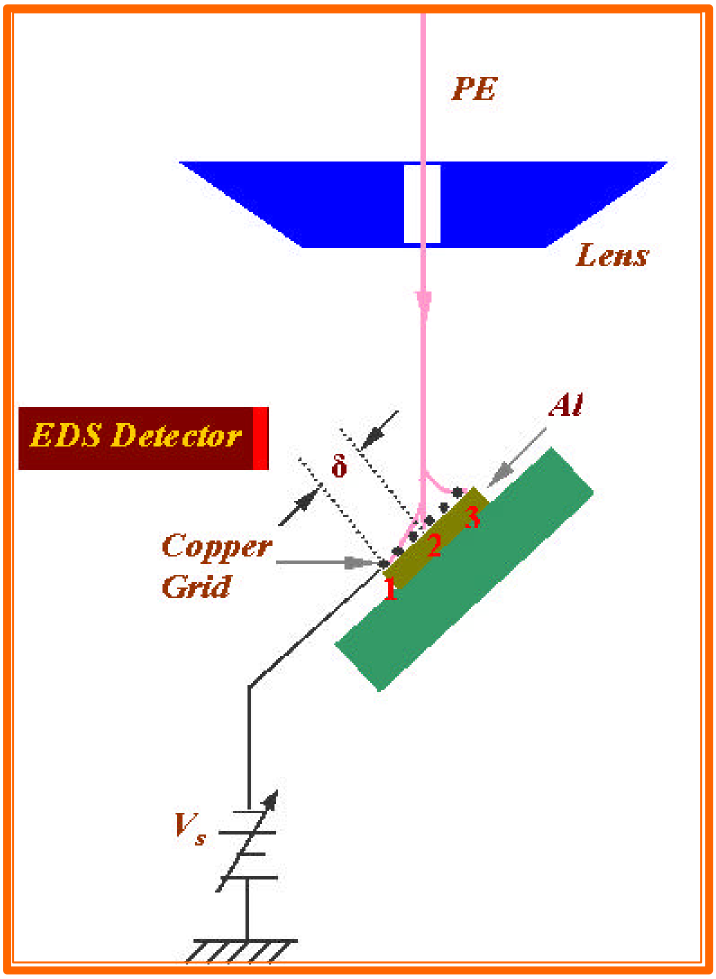

Figure 2.7 Schematically show an experimental arrangement to measure the surface potential V_s

2.3.4 Time-Resolved Current Method

When insulator surface is irradiated by electron beam I_0 under the point scan, the backscattered and emitted secondary electrons are combined as current i_{bs}. The incident electrons will be trapped at the defects sites inside sample and from a space charge distribution. As the space charge intensity increases, the internal electric field may reach strength to detrap the trapped electron. The charge trapping process will produce a displacement current i_d on the backside when electrons are trapped on the front side. The leakage current i_l comes from the carrier diffusion due to the electron detrapping and flow process. By the conservation of current, a general formula is derived as

$$I_0 = i_{bs} + i_d + i_l \qquad 2.18$$

as figure 2.8 shows [Gross et al. 1974].

The saturated trapped charge, defined by Q_s when the equilibrium is obtained between electron trapping and detrapping, can be calculated as

$$Q_s = \frac{(1 - sU_0)I_0}{\dfrac{g_i}{e_0 e_r} + \dfrac{(1 - s U_0)I_0}{pe_0(e_r + 1)R(U_0 - U_{C_2})}} \qquad 2.19$$

here s is the sum of the backscattered electron and secondary electron coefficients, U_0 beam voltage, R the electron penetration depth, g_i the radiation-induced conductivity, U_{C_2} is the secondary critical energy where s is equal to unity. This method can be solved to find the charge stored inside the surface, then according to the simple Coulomb's law

$$V(r) = KQ/(4pe_0 r) \qquad 2.20$$

by neglecting the higher order terms of 1/r. Here Q is a point charge (point scan mode), $K = 2/(e + 1)$, e and e_0 the relative permittivity of the dielectric and the permittivity in vacuum respectively [Song et al. 1996].

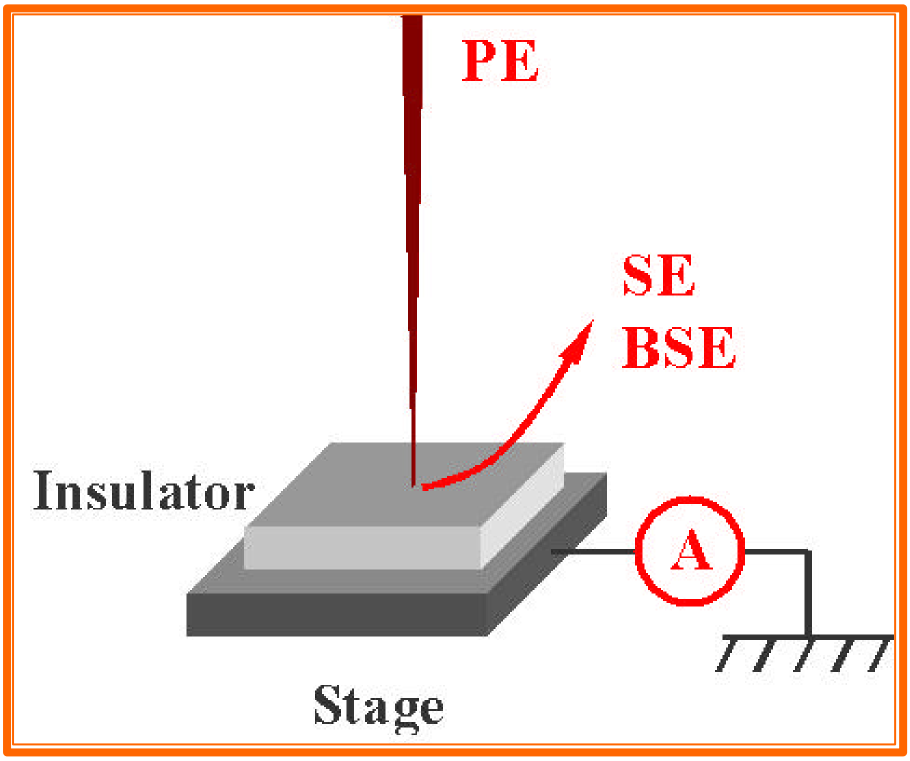

Figure 2.8 Experimental setup for the measurement of time-resolved current

2.3.5 Duane-Hunt Limit Method

The general x-ray spectrum consists of two parts: continuum x-rays which are produced by slowing down the beam electrons in the Coulomb’s field of the sample atoms; characteristic x-rays which are formed by ionization of the inner shell electrons. The characteristic x-rays appear as peak form and superimpose on the continuum x-rays. The Duane-Hunt bremsstrahlung limit is a good diagnostic to detect sample charging, which depends on a measurement of the high-energy cut-off, the Duane-Hunt limit of the fluorescent x-ray continuum from the specimen [Newbury 2000][Tang et al. 2003a][Duane et al. 1915][Belhaj et al.2001]. The Duane-Hunt limit (in EDS) or the short wavelength cutoff (in WDS) is defined as the energy E_{DH} with wavelength

$$\lambda_{swl} = 12.4keV / E_0 \tag{2.21}$$

E_{DH} can be measured by dropping the voltage across a high value resistor in series with a voltmeter, or can be determined on electron probes or scanning electron microscopes equipped with Energy Dispersive Spectrometers (EDS) [Solosky et al. 1972]. The intensity of the x-ray spectrum in the vicinity of E_{DH} decreases linearly to a near zero count level at E_{DH} while at higher energies there is also a linear decrease in counts. The intersection of these two lines provides an accurate measure of E_{DH}, as figure 2.9 shows. Since no emitted x-ray photon can have more energy than the incident electron which generated it then if the D-H limit occurs at some energy E_{DH}, and the incident electron is of energy E_0 then the surface potential is given as

$$eV_s = E_0 - E_{DH} \tag{2.22}$$

where e is the charge of the electron. The true Duane-Hunt energy limit can be experimentally determined by using the slope of the continuous spectrum and extrapolating to find the intersection [Myklebust et al. 1990].

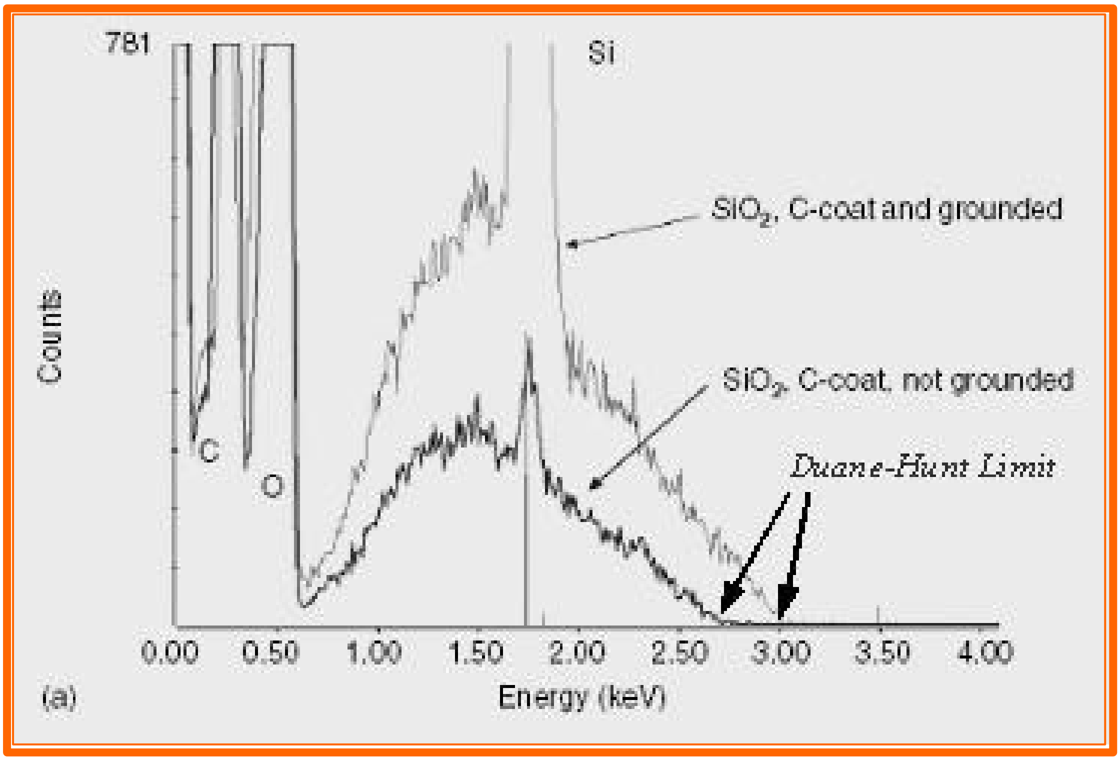

Figure 2.9 Spectra of SiO_2 with a thin conductive carbon layer irradiated by 3keV electron beam with and without grounded

CHAPTER III QUANTITATIVE MEASUREMENTS OF CHARGING IN A GASEOUS ENVIRONMENT

3.1 Introduction

The aim of alleviating the surface charging can be achieved from the origin of surface charging: surface charging in insulator is the result of surplus electrons in surface due to the inequality between the incident electrons and the emitted electrons. Negative charging means the number of incident electron is larger than that of the emitted electrons. Such inequality can be achieved by lowering the beam energy, tilting sample, or introducing gas inside the SEM chamber. The basic principal of using gas suggested that gas molecules are ionized and positive ions will flow to the negatively charged region to neutralize the charge. These ionization and neutralization processes are affected by many parameters such as beam energy, gas pressure, and gas type [Tang et al. 2002]. Quantitative measurement of surface charging in the presence of a gaseous environment is important to elucidate and helpful to understand these processes.

3.2 Experimental Method

A Hitachi S-3500 (Hitachi High Tech America, Pleasanton, CA) variable pressure scanning electron microscope (VP-SEM), which can operate from high vacuum up to a pressure level equal to 270 Pa, was employed in these experiments. The chosen gas is introduced through a computer operated leak valve controlled by a feedback loop so as to maintain a relatively stable pressure.

A capacitance manometer gauge (MKS Inc., Andover, MA), which has a reading independent of the type of the gas, was used to measure the pressure achieved around the specimen. Although the microscope can be operated over the energy range from 1 to 30kV, the experiments discussed here were centered in the range 3 to 30kV because the methods of data analysis were not reliable at low x-ray count rates. A specimen which is not charged-up has a surface potential of zero volts with reference to ground. When this sample acquires a charge then this potential can become positive or negative. A measurement of the surface potential therefore quantifies most of the charge states of the specimen. An ideal charge measurement technique would allow the surface potential to be monitored in real-time and at high precision, without interfering with the specimen and its environment in any way. The two techniques proposed here only approximates this ideal case but, because they rely on the use of the energy dispersive x-ray detector attached to the VPSEM, they are simple and convenient to implement and offer reliable results.

3.2.1 Duane-Hunt Limit

The first method depends on a measurement of the high-energy cut-off, the Duane-Hunt limit of the fluorescent x-ray continuum from the specimen [Duane et al. 1915]. Since the energy of the incident electron is always higher than that of the emitted x-ray photon then the surface potential is given as

$$eV_s = E_0 - E_{DH} \qquad 3.1$$

where e is the charge of the electron, E_{DH} the D-H limit, and E_0 the incident electron energy. The measurement is performed by recording into a Multi-Channel Analyzer (MCA) the x-ray spectrum from the sample as it is irradiated by the incident beam. The EDS arrangement inside SEM is shown in figure 3.1. A regression fit is then made to the top 50 or so channels of the spectrum before the continuum goes to zero to find the actual cut-off value (figure 3.2 (a)). The precision of this measurement is limited by the energy resolution of the detector. Here a Gresham (Gresham Scientific Instruments, Marlow, UK) detector with a resolution of 135eV at MnKα was used. The method is generally reliable but if the sample charges very strongly negative then the

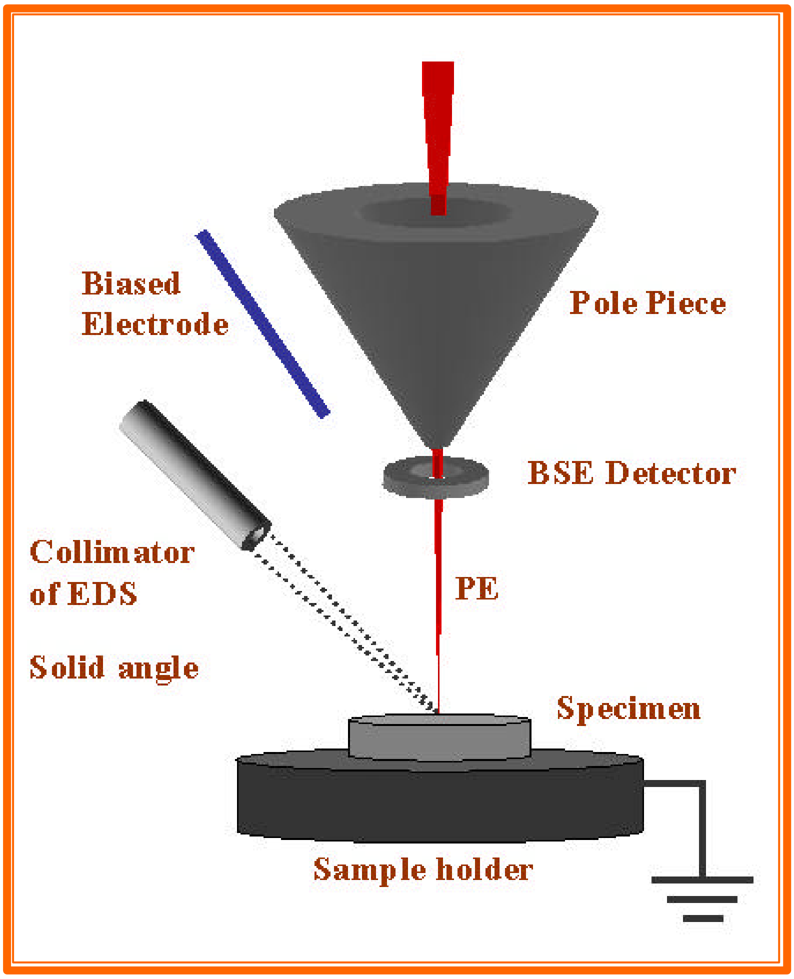

Figure 3.1 Schematically show the arrangement of the EDS inside the SEM

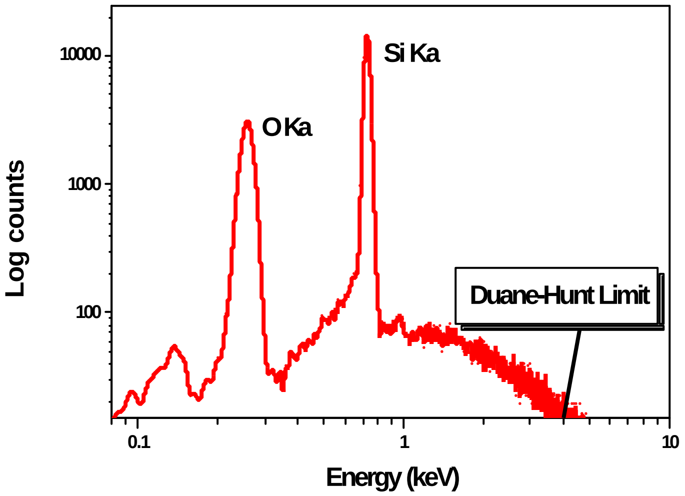

(a) Duane-Hunt Limit

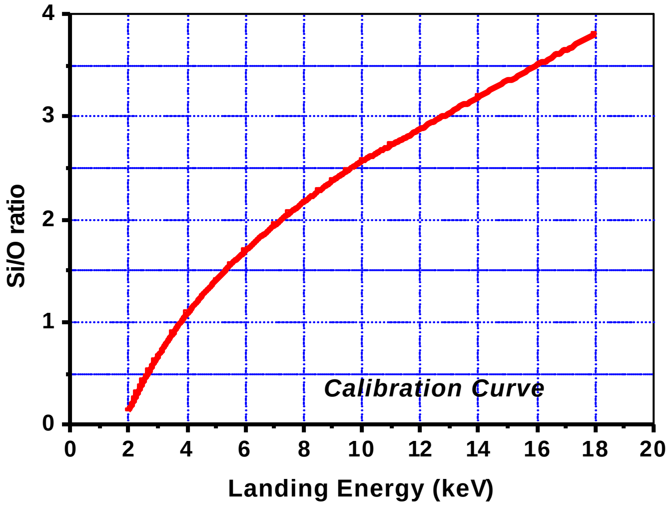

(b) Peak Ratio method

Figure 3.2 Two methods to measure the surface potential under charging condition on quartz (a) Duane-Hunt limit (b) Peak Ratio method secondary electrons emitted from the sample are re-accelerated by the field resulting from the charge, strike the bottom of the lens or the walls of the sample chamber at high energies, producing a spurious x-ray spectrum which can confuse the measurement. If there is a characteristic x-ray line too close to the Duane-Hunt limit, the spectrum appears curved and the precision in the determination of D-H limit degrades. The spectrum should be accumulated for a sufficient length of time and at a low detector dead time so as to achieve statistically reliable results and to minimize pulse pile-up.

3.2.2 Peak Ratio Method

The x-ray spectrum will be badly distorted by surface charging when the incident electron energy is close to the characteristic x-ray line. It is not precise to directly extrapolate the slope of the spectrum to obtain the Duane-Hunt limit under such circumstance. The peak ratio method, or by measuring the peak area data for the ratio of two x-ray emission lines on x-ray spectrum from the sample can reflect the dynamic effect on the Duane-Hunt limit due to charging. These can be either for example, the K- and L- lines of the same element, or lines from two elements with different excitation energies. For example on quartz the ratio of the Si-K and O-K lines can be used. In all cases the ratio is a sensitive function of the incident beam landing energy E_L, as shown in figure 3.2 (b). In our work a calibration curve of peak ratio vs. E_L for the sample of interest was generated by using spectrum simulation capability in Desktop Spectrum Analyzer (DTSA) [Fiori et al. 1992]. As a complementary method to the Duane-Hunt limit, the peak ratio method is mainly used at low beam energies (less than 5keV).

The Duane-Hunt limit method depends on measuring the high-energy cutoff of the continuous bremsstrahlung x-ray spectrum while the peak ratio method relies on the characteristic x-ray peak. The efficiency of characteristic x-ray generation from a solid target depends strongly on the overvoltage U

$$I \propto (U-1)^n \qquad 3.2$$

where $U = E_0 / E_c$, E_0 is the incident beam energy, E_c is the critical excitation energy for the atomic shell of interest, and the exponent n is in the range 1.3-1.7 [Goldstein et al. 1992]. As U? 1, the peak intensity decreases sharply as figure 3.3 shows for a value of $n = 1.35$. When charging phenomenon occurs on surface, the electric field decelerates the incident beam, altering the effective value of E_0. The x-ray excitation is thus sensitive to charging effect in low-voltage regime.

On the other hand, the x-ray spectrum collected by the EDS is just part of the x-ray signal produced as factors such as sample absorption, and detector collection efficiency are also important. Figure 3.4 illustrates the effect of gas pressure on the shape and peak height of the x-ray characteristic peaks on quartz under 10keV electron beam irradiation. As the gas pressure increases, which corresponding to a more positive surface potential, the peak ratio of two elements (Si/O) has an increasing tendency though the single peak intensity may fluctuate.

From equation 3.2, the peak ratio of x-ray characteristic spectra can be deduced, assuming the constant n is as 1.35. Replace $E_{OK} = 0.55keV$, $E_{SiK} = 1.7keV$ into them

$$\frac{I_{SiK}}{I_{OK}} = C_1 + C_2 (1 - \frac{1.15}{E_0 - 0.55})^{1.35} \qquad 3.3$$

here C_1, C_2 are constants. This equation illustrates the relationship of peak ratio and incident beam energy (landing energy), as figure 3.5 shows.

Figure 3.5 shows the production curve of the characteristic peaks as the function of landing beam energy. The actual x-ray spectrum received by EDS detector is just part of the total x-ray signal produced due to the factors as sample absorption, detector collection efficiency. In order to calculate the actual landing energy of electron by the peak ratio method, a calibration curve is needed, as figure 3.6 shows. An x-ray spectrum taken from quartz surface by 15keV incident beam in 20Pa air environment is used as reference and the beam landing energy is measured by Duane-Hunt limit. Then Desktop Spectrum Analyzer (DTSA) software is used to

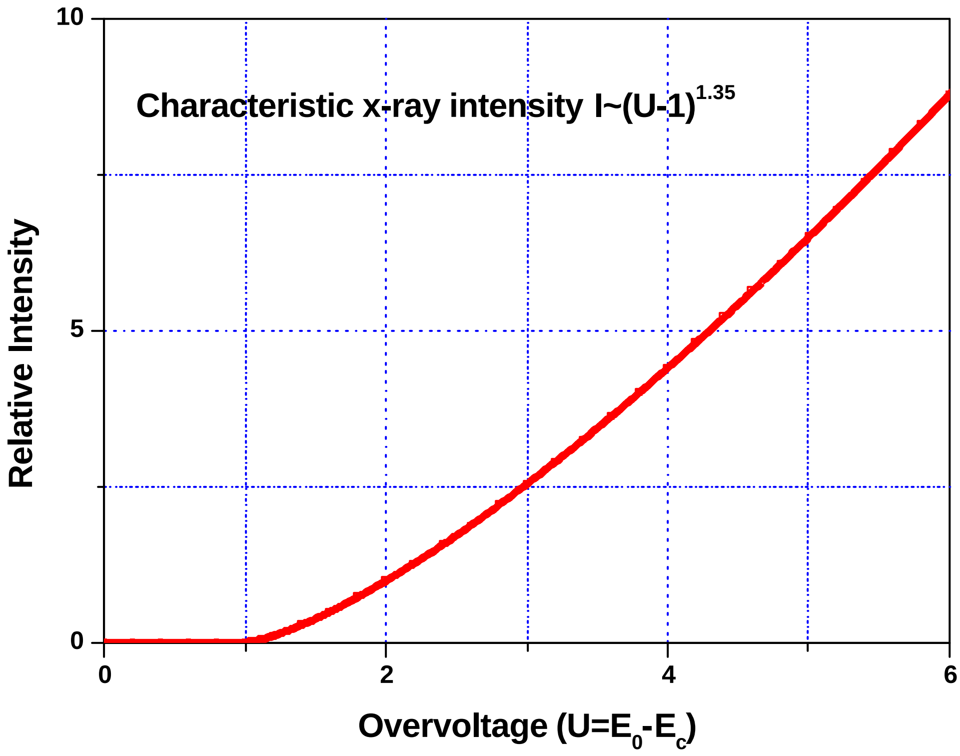

Figure 3.3 Relative intensity of characteristic x-ray varies with overvoltage U. $I \propto (U-1)^n$, where $U = E_0 / E_c$, E$_0$ is the incident beam energy, E$_c$ is the critical excitation energy, and $n = 1.35$ in this example.

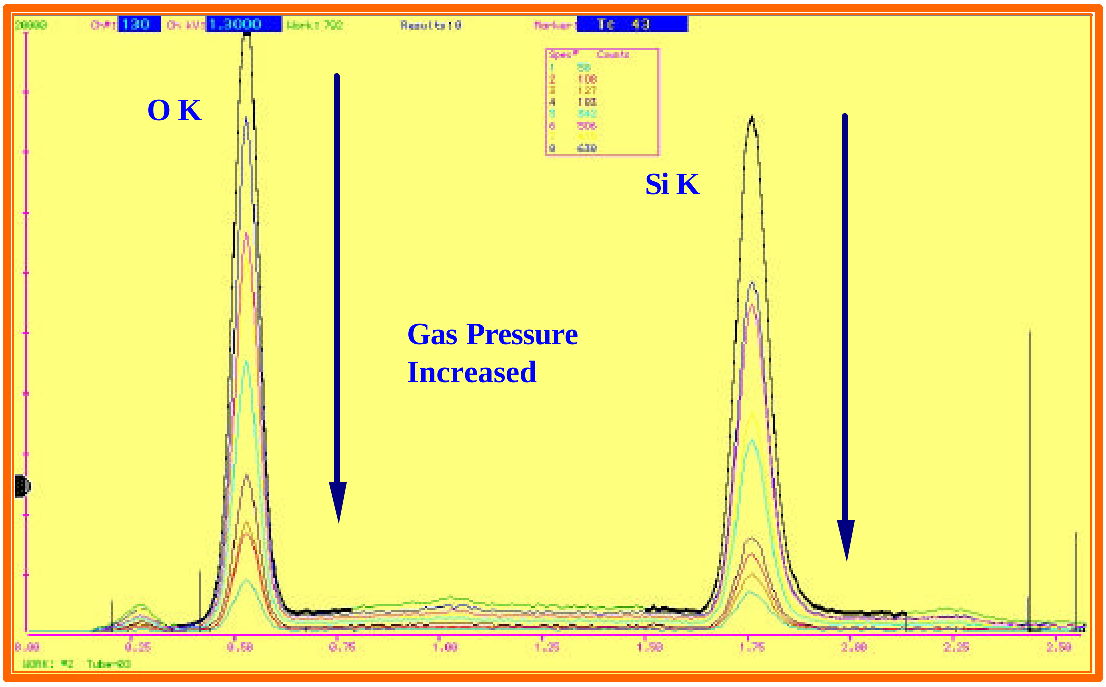

Figure 3.4 The variation in spectra of quartz excited with a 10keV electron beam as a function of gas pressure

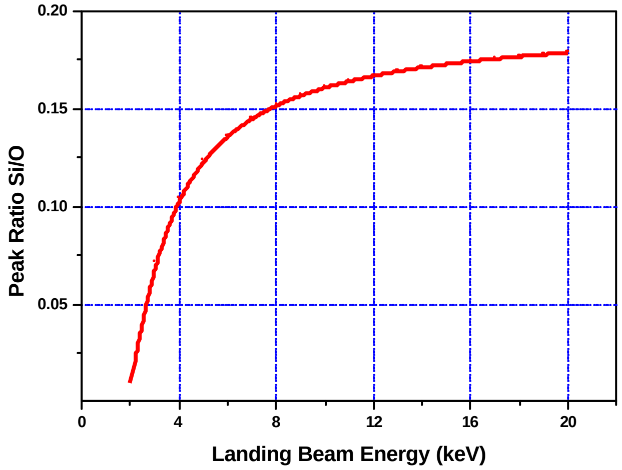

Figure 3.5 Relationship curve of the peak ratio Si/O with the landing beam energy

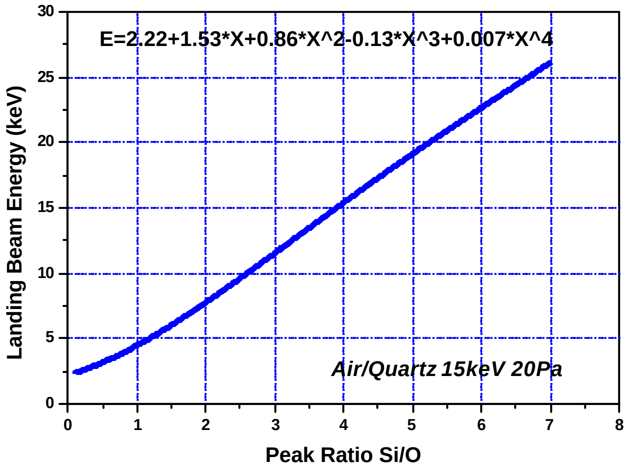

Figure 3.6 The calibration curve of peak ratio Si/O on landing beam energy. Quartz is irradiated by 15keV beam energy in 20Pa air environment. The equation represents the regression fit to the experimental data.

simulate the spectrum, which has the same Duane-Hunt cutoff value and Si/O peak ratio by adjusting the relative composition of silicon and oxygen. By changing the landing beam energy, a series of x-ray spectra are simulated and the relationship of landing energy and the peak ratio of Si/O is obtained. For a given x-ray spectrum, the landing beam energy can be derived from its Si/O peak ratio by this calibration curve.

3.3 Experimental Procedure

Specimens were locally irradiated in the Hitachi S-3500 SEM at a working distance (the distance between sample surface and pole-piece) of 12mm (chosen to optimize the EDS detector efficiency), a magnification of ×90, and fast scanning mode (50 frames per second). The x-ray energy-dispersive-spectra (EDS) were obtained using a Gresham x-ray detector. All experiments were performed using four insulating, flat and featureless samples - mica (Si, Al, K, O, F), sapphire (Al_2O_3), quartz (SiO_2), and COG (chrome on glass) mask and the spectrum recording time was set as 100 seconds. In order to minimize the influence of the remaining charge from the former irradiation, the successive irradiation must be performed at fresh area. The plate electrode of the SE detector is always present inside the chamber with 250volts bias voltage at standard SE mode (SSE). The experimental procedures were as follows for each of the gases and samples used.

1. At a given electron beam energy and pressure, the dead time of the x-ray spectrometer was adjusted to 30% by changing the current of the condenser lens to vary the beam current. The surface current was measured by a GW (GW Electronics, Gwinnett, GA) Type 31 specimen current amplifier which is connected with the sample holder.
2. The gas pressure was varied from 270Pa, then down to 200Pa, 100Pa, 30Pa, 10Pa, 3Pa and finally to 1Pa and move to fresh area each operation so as to minimize any effects from residual ionization from previous runs.
3. The above procedure was repeated at various beam energy.

4. For each spectrum recorded, the surface potential was derived from the real D-H limit.

Dead time is defined as the time required for the tube to recover sufficiently accepting the next pulse and is often expressed as a percentage of real time. The dead time relationship is

$$N = \frac{N'}{(1 - tN')} \qquad 3.4$$

where N' is the measured count rate, N is the true count rate to calculate, and t is the dead time in seconds. Low dead time results in poor spectrum statistics while too high a dead time means wasting time. In the experiment, 30% dead time was used based on the tradeoff between optimum collection efficiency and spectrum quality.

An analysis of the surface potential variation with pressure shows a behavior of the type shown in figure 3.7. At the lowest pressure (<1Pa) the charge is pinned at the value found for high vacuum irradiation. At the highest pressures the potential again stabilizes to a constant value independent of the actual pressure. Within the intermediate-pressure region, the surface potential varies logarithmically with pressure as:

$$V_s = A + K * \log(P) \qquad 3.5$$

here V is the surface potential, P the gas pressure, A is a constant, and K the charging reduction efficiency (CRE), which is defined as the change of surface potential with pressure under steady state condition. While in both low-pressure and high-pressure regimes, the surface potential is pressure independent but different stable potential values are obtained respectively. The actual surface potential will also depend on the magnitude of the beam current although the functional form of the variation with pressure remains the same. In order to illustrate this behavior the charging profile with gas pressure will be studied as a function of material, the type of the gas, beam energy, and other parameters.

Since the gas pressure value read from the SEM gauge meter is the value closed to the gauge detector which is situated near the leak valve but not the actual pressure on the sample surface and different gas has different partial pressure, the gas pressure calibration curve is thus

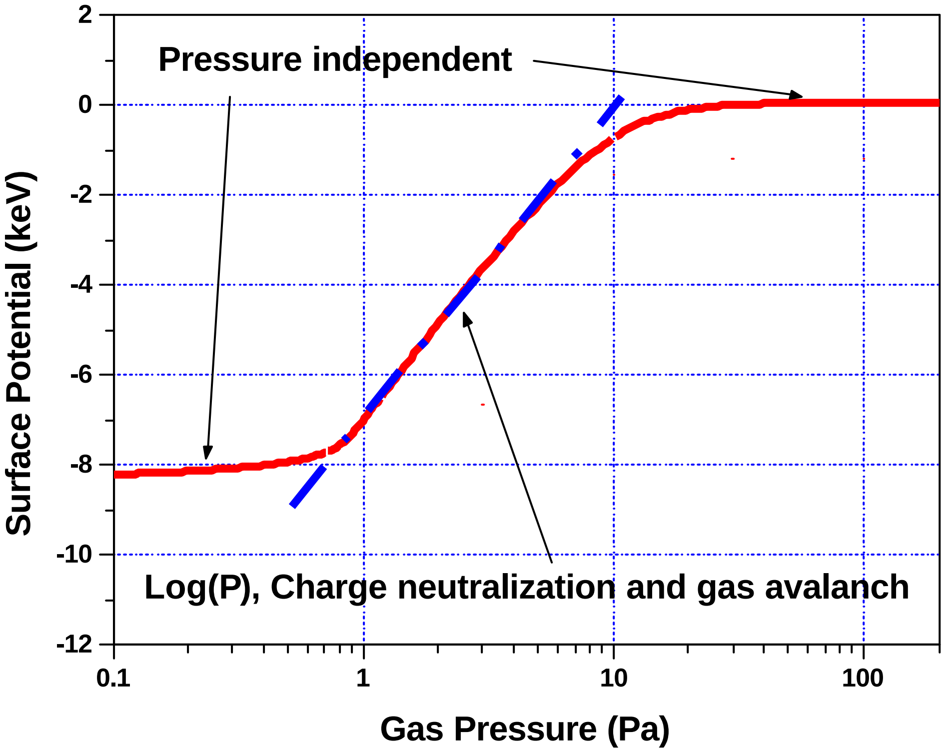

Figure 3.7 Two competing processes of charging reduction on sapphire in helium environment include the gas-ionization avalanche with the charge neutralization and the ion-electron recombination. Sample size is $2\times 2\times 0.2$cm. The electric resistivity of sapphire is 2E+11 $\Omega\cdot m$ [Shackelford et al. 2000]. The electrode is presented inside the chamber with 250volts bias voltage in standard SE mode (SSE). The primary beam energy is 10keV.

needed to monitor the real pressure value. Only the pressure near the surface can demonstrate the function of the gas used. Following figure 3.8 is the calibration curve relating the nominal value and the real value.

In an environmental SEM or VPSEM, the pressure is controlled by a computer operated leak valve and a suitable feedback circuit monitoring the pressure read by a Pirani gauge. Typically this leads to a condition in which the pressure cycles slowly with time about the nominal value as the valve opens and closes, and results in the difficulty of the correct determination of the gas pressure, as figure 3.9 shown. This problem can be alleviated by a longer collection time. Furthermore, this reading is strongly dependent on the chemical composition of the gas to which the gauge is being exposed [Bigelow 1994].

To overcome the limitations of the Pirani gauge supplied with the VPSEM, a MKS Baratron® 626A Capacitance Manometer (with 0.25% accuracy) was installed in the S-3500N VPSEM. The Capacitance Manometer transducer is an active sensor, which makes gas composition independent pressure measurements and provides a real-time digital readout. Pressure is determined by measuring the change in capacitance between the diaphragm and an adjacent dual electrode. The type 626A Absolute Pressure Transducer (~0.25% accuracy) applied in our experiments could give reliable and repeatable pressure measurements in the range from 10^5 Pa to as low as 10^{-3}pa.

With the employment of the Capacitance Manometer, much more accurate and reliable chamber gas pressure reading could be obtained both because of the gas independence of the measurements, and because of the position of the gauge inside the specimen chamber. This step enhances the accuracy of the surface charging measurement.

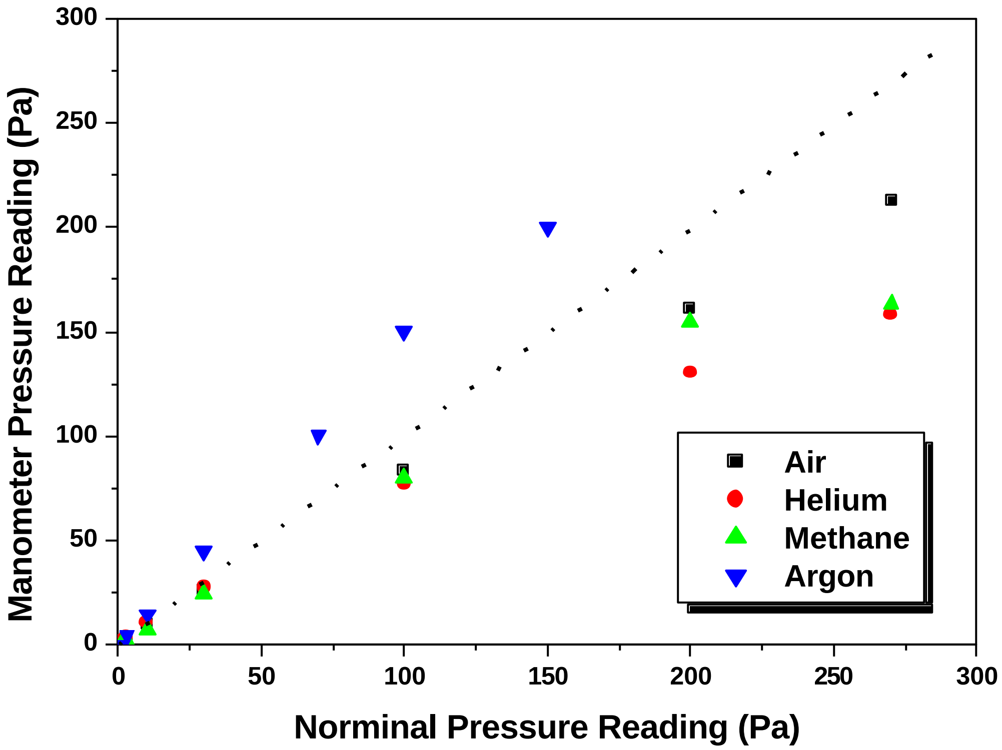

Figure 3.8 Pressure readings by capacitance manometer and Pirani gauge

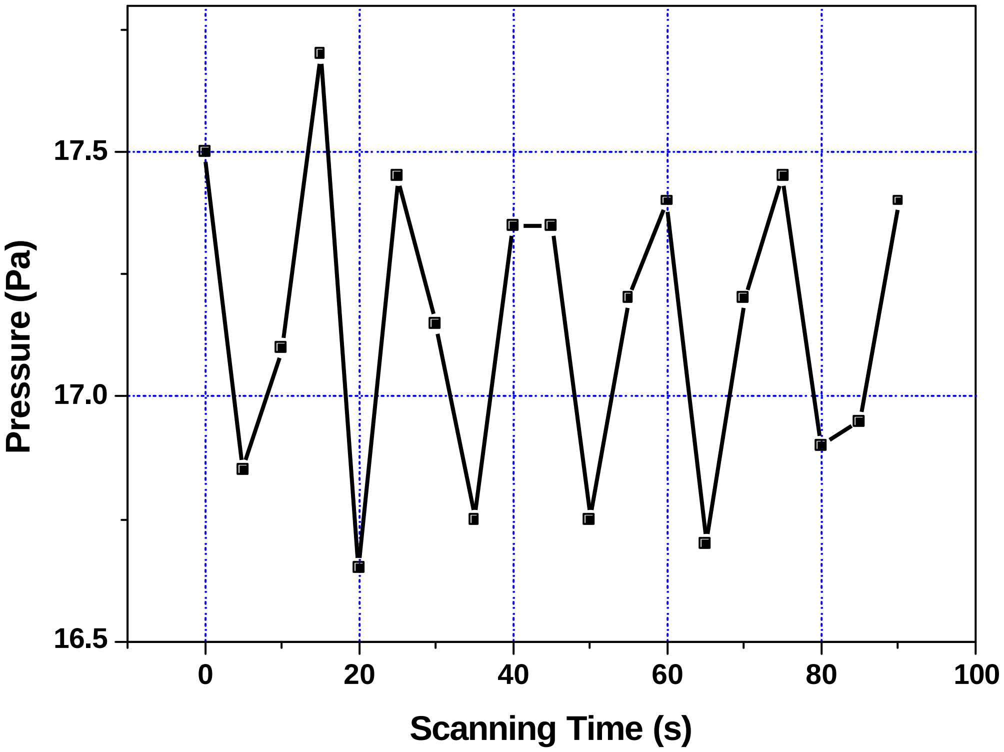

Figure 3.9 Periodic variation of pressure with scanning time

3.4 Experimental Results

Table 3.1 lists some characteristic parameters of the specimens used in the experiment.

3.4.1 Effect of Gas Type on Charge Reduction

Mica was irradiated under 10keV electron beam in the gas atmosphere of air, helium, and argon. The results of surface potentials changing with gas type and gas pressure under the irradiation of 10keV beam are shown in figure 3.10. The sample charged badly under the beam irradiation at high vacuum and the initial potential is different for each of gases at around 1Pa. As the gas pressure is raised beyond 1Pa the surface potential becomes less negative. The variation with pressure follows the generic relationship of equation 3.5 but the slope K varies with gas. K can be regarded as a measure of the charge reduction efficiency (CRE) $\Delta V / \Delta \log P$. Eventually the surface potential charge goes through zero at some pressure, which can be called the charge balance pressure and is related with the gas type used (11Pa for helium, 12Pa for air, and 22Pa for argon at the gas path length of 12mm employed here). Finally the surface reaches a stable potential which may be zero, negative, even positive and which remains constant up to the maximum accessible pressure. These curves all contain the same feature as figure 3.7 but with different parameters such as the stable value of surface potential, the CRE, and the pressure at which charge balance occurs.

Mica was irradiated under 15keV electron beam in the gas atmosphere of air, helium, methane, and argon, and the results of surface potentials varying with gas type and gas pressure is shown in figure 3.11. They have similar trend as that of figure 3.7 except the charging balance value: methane 22Pa, helium 80Pa, air 110Pa, and argon 34Pa.

As the irradiation beam energy changes to 20keV and the gas atmosphere of air, helium, methane, and argon on the surface of mica, the results of surface potentials variation with gas

Table 3.1 Material constant for some samples used in experiment

	Mica*	Sapphire	Quartz	Teflon (PTFE)	Silicon
Composition	SiO_2, Al_2O_3, K_2O, Fe_2O_3, MgO, CaO, Hg_2O	Al_2O_3	SiO_2	PolyTetraFluoroEthylene	Si
Dielectric Constant (at 1MHz)	5.4-8.7	10.1	4	2.1	11.7
Volume Resistivity ($\Omega \cdot m$)	4×10^{15}	10^{16}	10^{11}	$>10^{20}$	10^{6}
Thermal Conductivity ($W \cdot k / m$)	0.75	32	1.1	0.25	145.7
Size (cm)	$4\times 2\times 0.2$	$2\times 2\times 0.2$	$4\times 2\times 0.2$	$\Phi\, 2\times 0.01$	$2\times2\times 0.1$

* SiO_2 (45.09) Al_2O_3 (34.50) K_2O (9.51) Fe_2O_3 (3.19) MgO (2.10) CaO (0.22) Hg_2O (0.6)

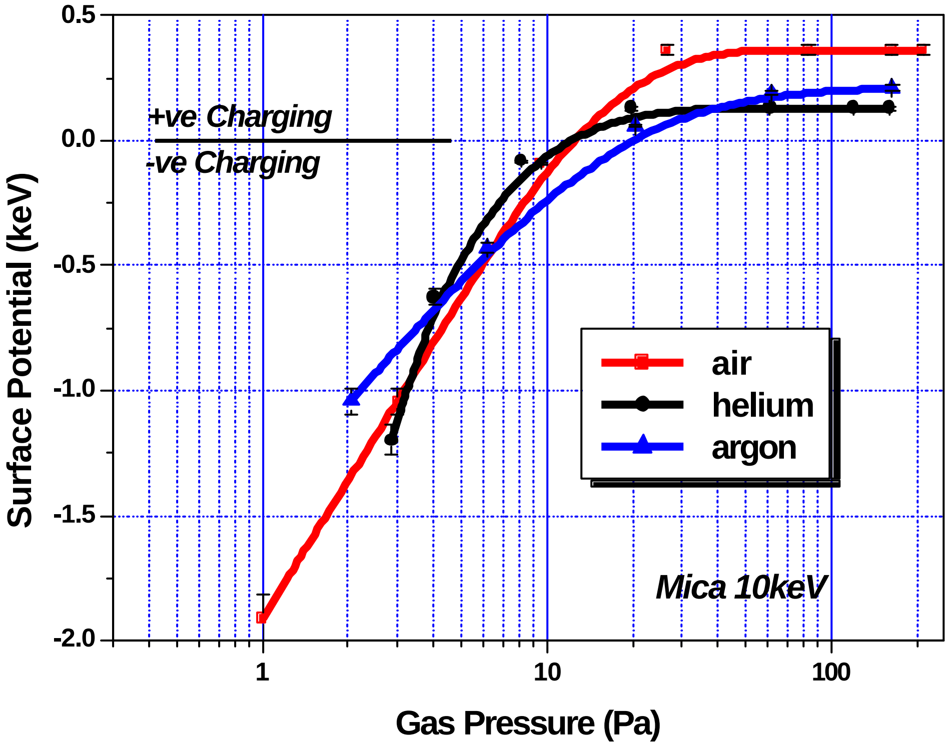

Figure 3.10 The charging potentials vary with gas pressure inside the gaseous environment of air, helium, and argon on mica by 10keV beam irradiation. The acquisition time for the x-ray spectrum was 100 seconds. The plate electrode of the SE detector is in SSE mode (250 volts). No objective aperture. The magnification is 90×. Working distance is 12mm.

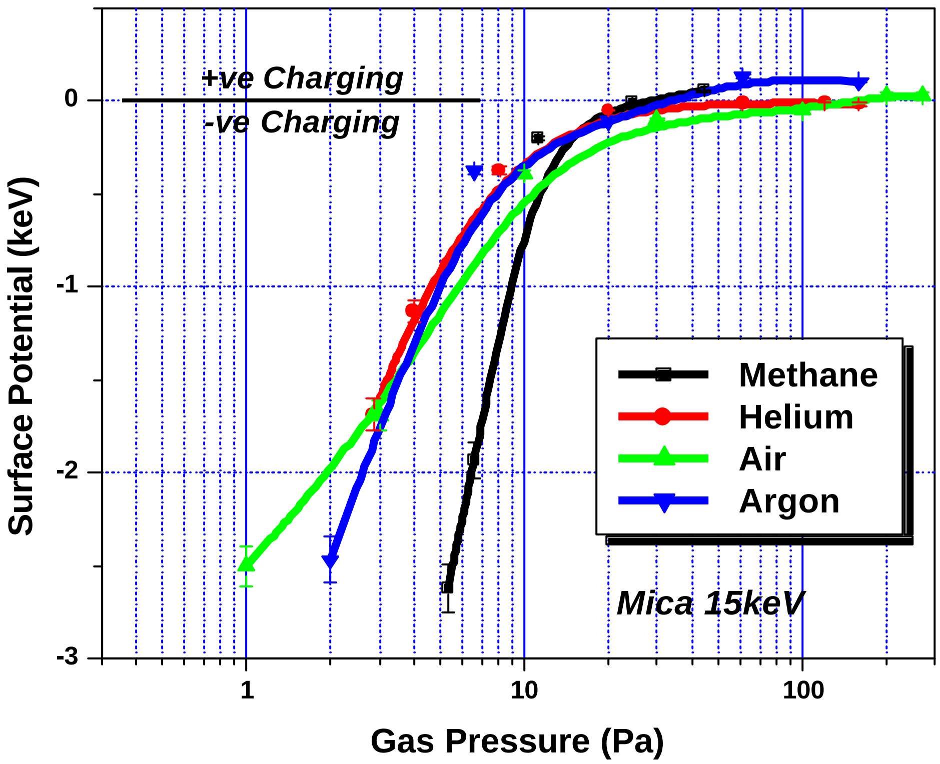

Figure 3.11 The charging potentials vary with gas pressure inside the gaseous environment of methane, helium, air and argon on mica by 15keV beam irradiation. The acquisition time for the x-ray spectrum was 100 seconds. The plate electrode of the SE detector is in SSE mode. No objective aperture. The magnification is 90×. Working distance is 12mm.

type and gas pressure are shown in figure 3.12. Although these curves have the same tendency as in figure 3.10 and figure 3.11, some of them cannot reach the charging balance which due to the beam energy effect (the charging balance values as 25Pa for methane and 52Pa for argon).

All the parameters related with the charging curve as the function of the incident beam energy are listed in table 3.2, including the charging balance pressure P^*, the charging reduction efficiency K, and the stable surface potential V_{stable}.

3.4.2 Effect of Beam Energy on Charging Reduction

The surface potential on sapphire was measured in a helium environment with beam energies of 10, 15, 20, 25, and 30keV. These results are shown in figure 3.13. The difference between the curves indicates how the beam energy can affect surface charging behavior. Although in all cases the surface potential becomes less negative as the pressure increased, the lower beam energy curve always lies above the higher beam energy profile. As the result while at 10keV the surface can be taken to charge balance (at 25Pa) and reaches a stable positive potential (~+100Volts), at 30keV the surface never achieve charge balance and stabilizes at a negative potential. This is consistent with the hypothesis that charge compensation occurs as the result of gas ionization caused by secondary electron emission. Since the SE yield falls with beam energy, charge compensation is less effective. Also the sensitivity of surface potential with gas pressure is different for various beam energies at lower gas pressure region.

The surface potential on sapphire was measured inside air environment with beam energies of 5, 7.5, 10, 15, and 30keV. These results are shown in figure 3.14. Although at higher beam energy curves have the similar shape as in figure 3.7, the surface potential of lower beam energy (less than 10keV) curves is independent with the gas pressure variation. For very low beam energy condition, the surface is even positively charged and independent of gas pressure.

Figure 3.15 shows the relationship between surface potential and gas pressure as the

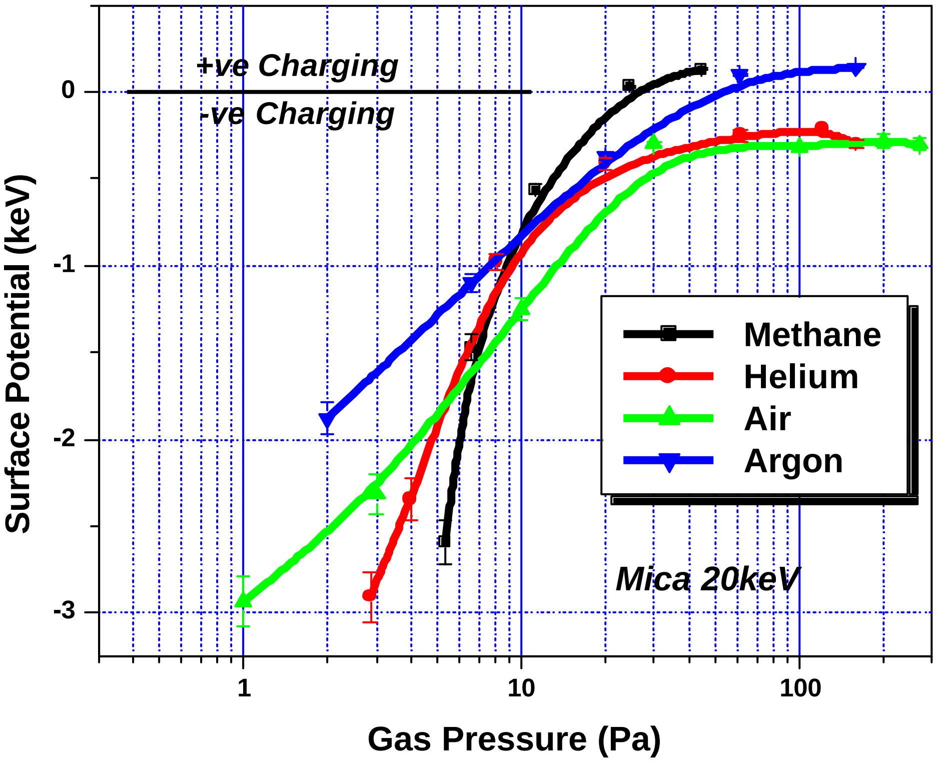

Figure 3.12 The charging potentials vary with gas pressure inside the gaseous environment of methane, helium, air and argon on mica by 20keV beam irradiation. The acquisition time for the x-ray spectrum was 100 seconds. The plate electrode of the SE detector is in SSE mode. No objective aperture. The magnification is 90×. Working distance is 12mm.

Table 3.2 Comparison P^* and CRE for different beam energy and gas type on mica

Gas Type	10keV			15keV			20keV		
	P^*	K	V_{stable}	P^*	K	V_{stable}	P^*	K	V_{stable}
Air	12	1.86	0.36	110	2.11	0.03	NA	1.69	-0.3
Helium	11	2.46	0.13	80	2.89	-0.02	NA	4.25	-0.2
Methane	--	--	--	22	7.45	0.05	25	6.25	0.13
Argon	22	1.1	0.21	34	4.03	0.1	52	1.79	0.1

Note: P^* (Pa) is the value of the charging balance pressure, K can be regarded as a measure of the charge reduction efficiency (CRE) $\Delta V / \Delta \log P$, and V_{stable} (keV) is the value of the surface potential at the stable state. All the data are from the surface of mica.

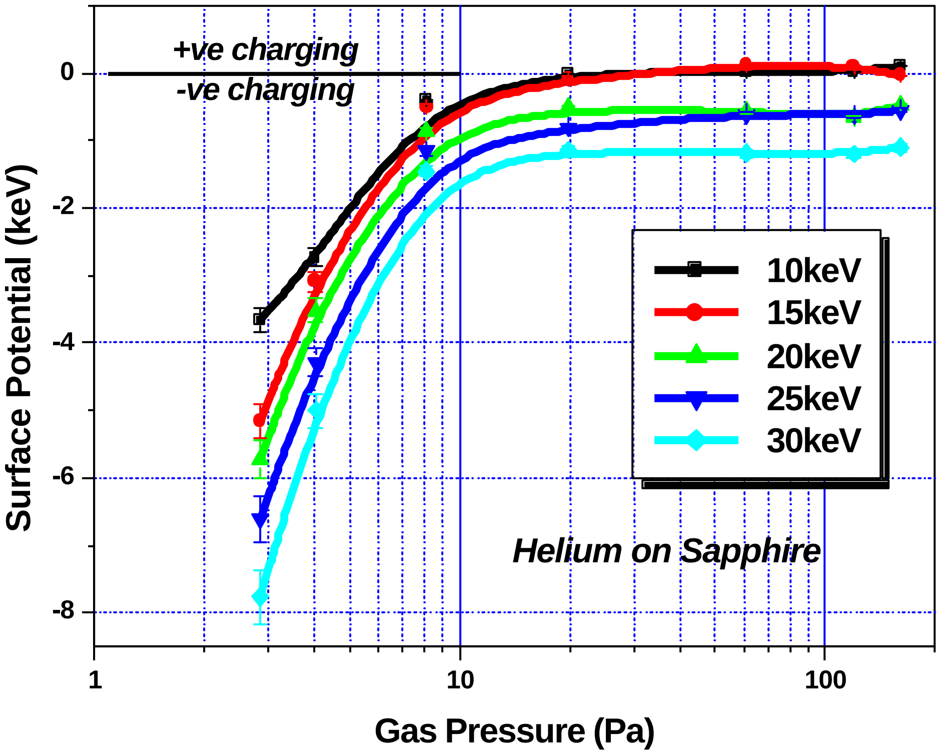

Figure 3.13 The relationship of surface potentials and helium gas pressure under different incident beam energies (10, 15, 20, 25, and 30keV) on sapphire. The acquisition time for the x-ray spectrum was 100 seconds. The plate electrode of the SE detector is in SSE mode. No objective aperture. The magnification is 90×. Working distance is 12mm.

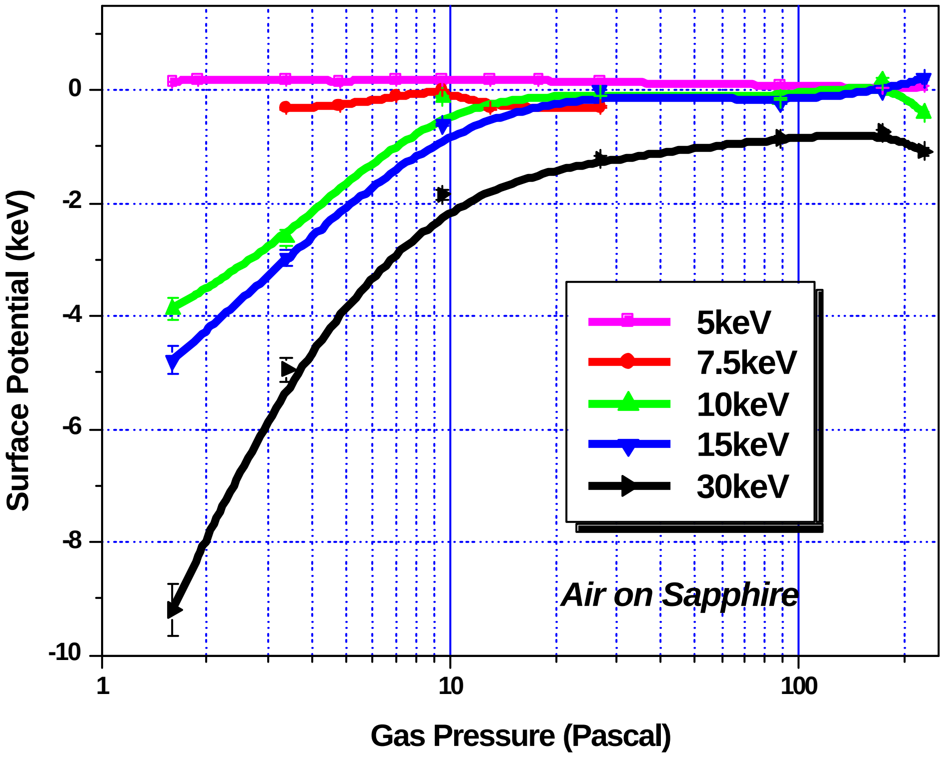

Figure 3.14 The relationship of surface potentials and helium gas pressure under different incident beam energies (5keV, 7.5keV, 10keV, 15keV, and 30keV) on sapphire. The acquisition time for the x-ray spectrum was 100 seconds. The plate electrode of the SE detector is in SSE mode. No objective aperture. The magnification is 90×. Working distance is 12mm.

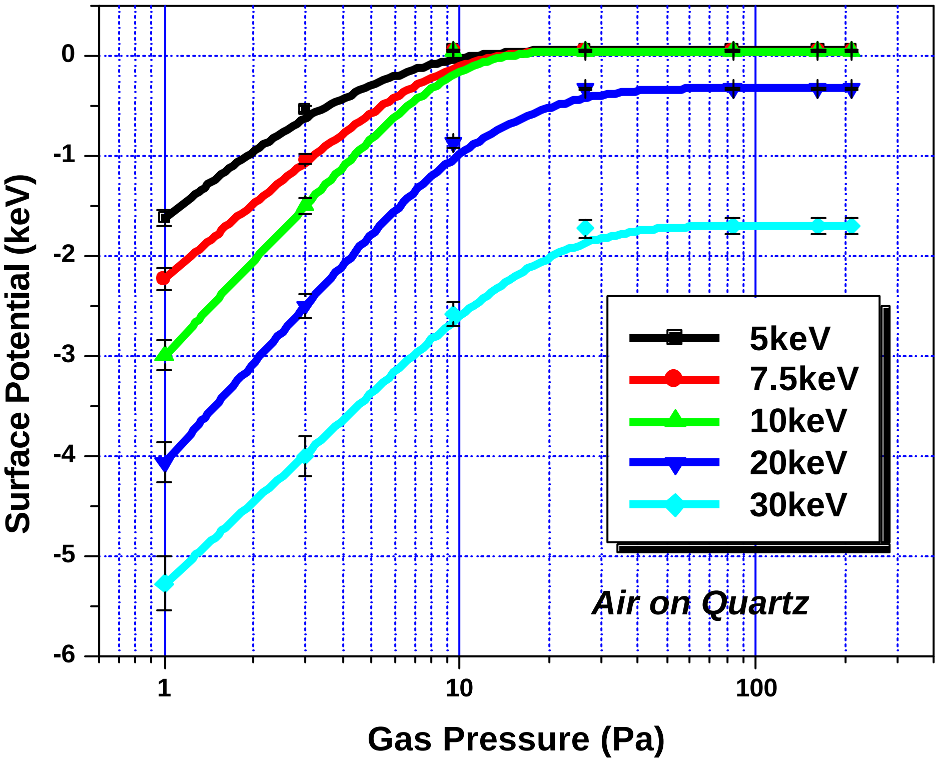

Figure 3.15 The relationship of surface potentials and air pressure under different incident beam energies (5keV, 7.5keV, 10keV, 15keV, and 30keV) on quartz. The acquisition time for the x-ray spectrum was 100 seconds. The plate electrode of the SE detector is in SSE mode. No objective aperture. The magnification is 90×. Working distance is 12mm.

function of incident beam energy (5, 7.5, 10, 20, and 30keV). All the curves have the characteristic tendency of figure 3.7, even at the low beam energy. In general higher beam energy corresponds to a larger CRE value and a lower stable surface voltage, but it is more difficult to reach the charging balance condition.

Figure 3.16 shows the charging characteristic curves (the surface potential vs. gas pressure) of Teflon in air atmosphere under various incident beam energies (5, 7.5, and 10keV). As the incident beam energy increases, the initial surface potential corresponding to lower gas pressure negatively increases and the charging reduction efficiency also increases since all three curves are tend to merge together at high gas pressure part. The curve in figure 3.17 indicates the correspondent variation of the specimen current. Noticeably, the relationship of the sample current vs. gas pressure is similar to that of the surface potential vs. gas pressure, which is shown in figure 3.7 as the general charging characteristic style. Details about the relationship of figure 3.16 and 3.17 based on theoretical calculation are stated in following discussion.

Parameters inside table 3.3, including the charging balance pressure, the charging reduction efficiency, and the surface potential at the stable state, indicate how the surface potential is affected by the incident beam energy for various gases and materials. As the beam energy increases, the charging reduction efficiency also increases and the charging balance pressure keeps constant or slowly rise, while the stable surface potential moves more negative.

Figure 3.18 shows the relationship of the incident beam energy and the surface potential on quartz surface under vacuum, 5Pa, 10Pa, 15Pa, and 20Pa air condition. The shape of V_s~E_P curve varies as the gas pressure increased. It clearly illustrated that the surface potential decreases with increasing incident beam energy at lower beam energy range, but reaches stable state at higher beam energy part in low gas pressure environment. As the gas pressure increases, the shape of such relationship curves also change. It must notice that the surface potential can reach a positive value when the incident beam energy is below 5keV. The beam energy vs. secondary electron yield curve is shown in figure 3.19. Assume the incident beam density as I_P and the

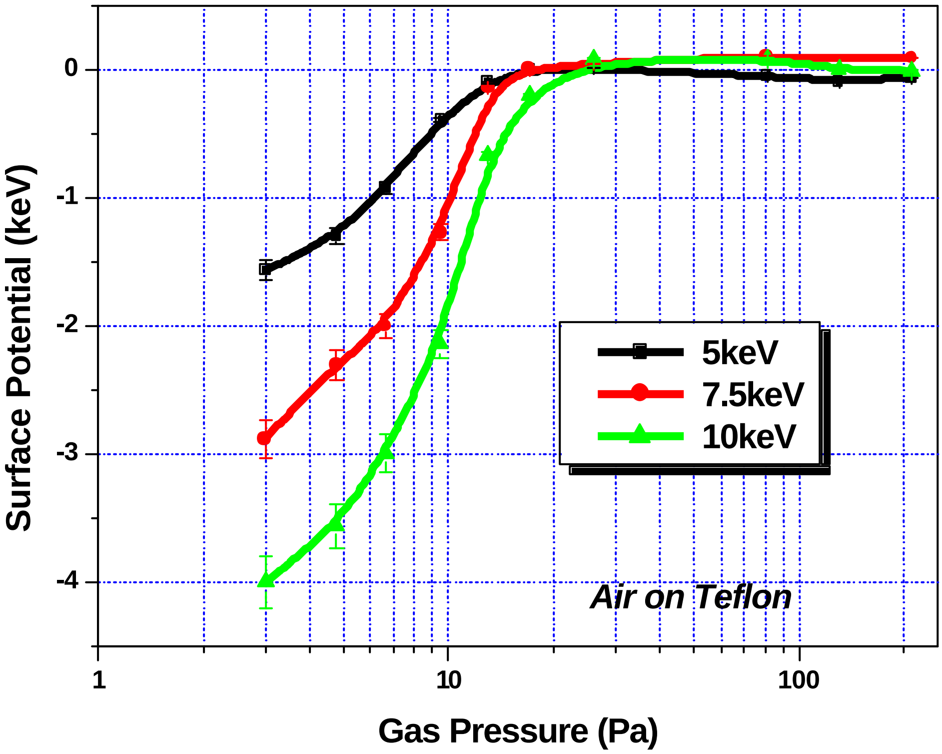

Figure 3.16 The relationship of surface potentials and air pressure under different incident beam energies (5keV, 7.5keV, and 10keV) on Teflon. The acquisition time for the x-ray spectrum was 100 seconds. The plate electrode of the SE detector is in SSE mode. No objective aperture. The magnification is 90×. Working distance is 12mm.

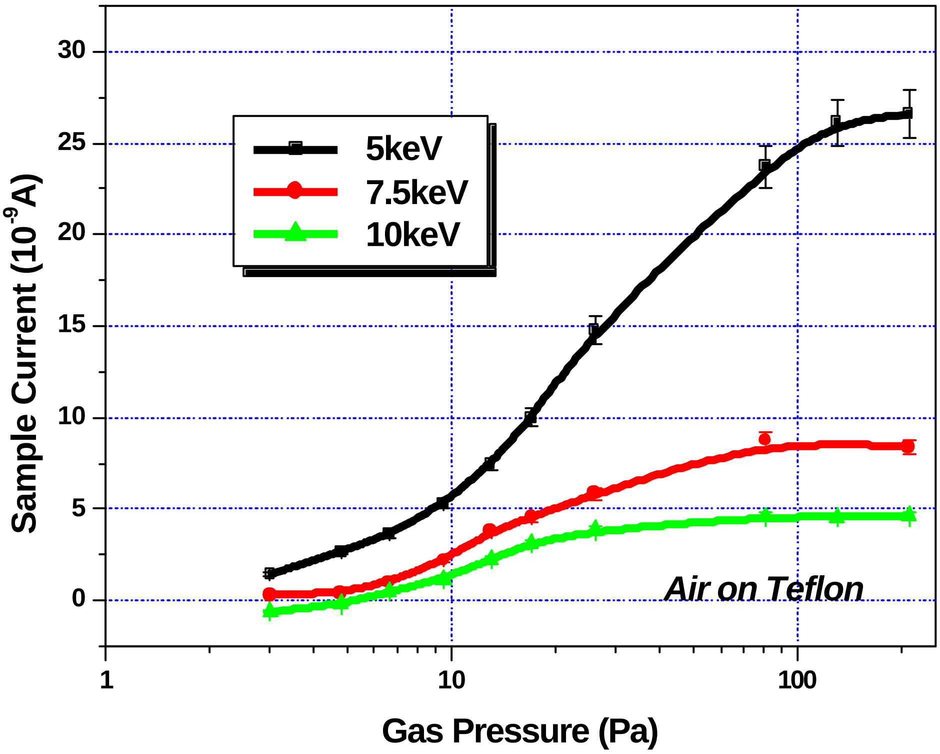

Figure 3.17 The specimen current varies as the function of gas pressure and incident electron energy at 5, 7.5, and 10keV on Teflon. The plate electrode of the SE detector is in SSE mode. No objective aperture. The magnification is 90×. Working distance is 12mm.

Table 3.3 Comparison P^*, CRE, and V_{stable} for different beam energy and gas type

Beam Energy (keV)	Helium on Sapphire			Air on Sapphire			Air on Quartz			Air on Teflon		
	P^*	K	V_{stable}	P^*	K	V_{stable}	P^*	K	V_{stable}	P^*	K	V_{stable}
5	--	–	--	NA	0	0.16	11	1.7	0.05	11	2.8	-0.1
7.5	--	–	--	9	0.7	-0.3	14	2.3	0.04	11	6.3	0.1
10	30	7.2	0.1	NA	4.9	-0.1	19	3.1	0.04	11	7.9	0.1
15	32	10.3	0.1	NA	5.4	-0.2	–	--	--	--	--	--
20	NA	10.7	-0.6	--	--	--	NA	3.3	-0.33	--	--	--
25	NA	12	-0.6	--	--	--	–	--	--	--	--	--
30	NA	13.9	-1.2	NA	16.2	-0.8	NA	2.8	-1.7	--	--	--

Note: P^* (Pa) is the value of the charging balance pressure, K can be regarded as a measure of the charge reduction efficiency (CRE) $\Delta V / \Delta \log P$, and V_{stable} (keV) is the value of the surface potential at the stable state. For air on sapphire at 5keV, the surface potential keeps positive value.

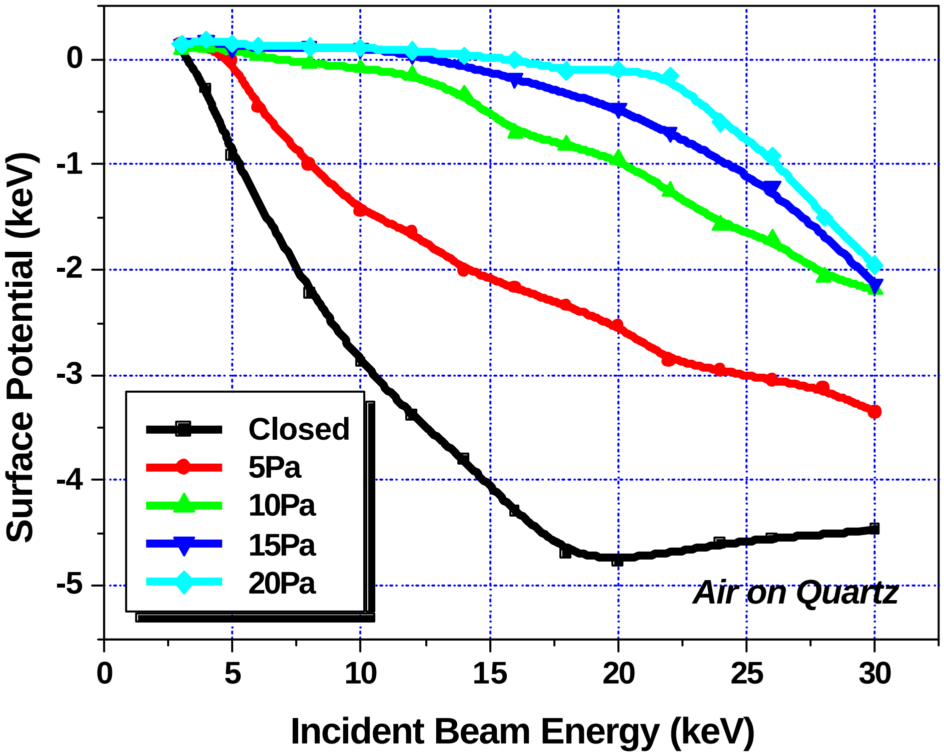

Figure 3.18 The experimental relationship of incident beam energy and surface potential under the condition of vacuum and 5Pa air on quartz. The acquisition time for the x-ray spectrum was 100 seconds. The plate electrode of the SE detector is in SSE mode. The magnification is 90×. Working distance is 12mm. No objective aperture.

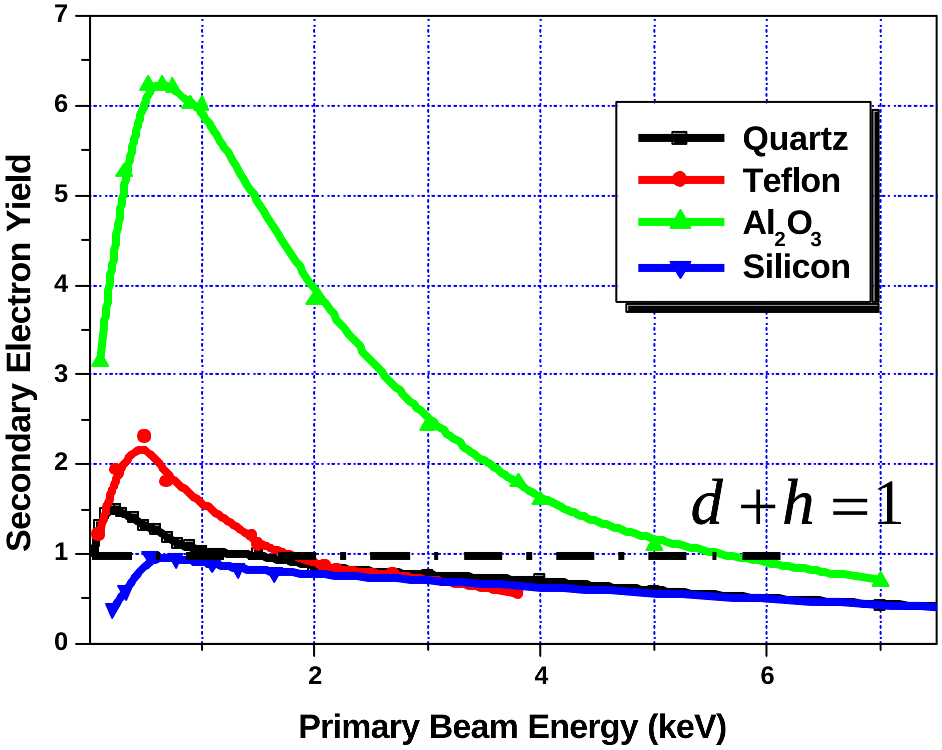

Figure 3.19 Illustration of the secondary electron yield curve as the function of the incident beam energy based on samples of quartz, Teflon, Al_2O_3, and silicon

secondary electron yield and the back-scattering electron yield as d and h respectively, then the surface charging can be defined as positively charging when $d + h > 1$, $d + h < 1$ for negatively charging, and surface neutralization when $d + h = 1$. Different materials have different SE yield curves and so display different E_2 energies.

3.4.3 Effect of Material on Charge Reduction

As shown in figure 3.20, for a given beam energy (10keV) and gas (helium), the surface potential achieved with pressure also depends on the material being irradiated. It is evident that the surface potential on the sapphire drops much faster than that on the mica, corresponding to a larger CRE value. Thus these two curves can merge together at high gas pressure though sapphire has a lower surface potential initially. Charge balance occurs on sapphire at 25Pa but only 11Pa for mica and both materials ultimately stabilize at a positive surface potential. This difference can be attributed to the variation in secondary electron yield between the materials.

In addition, the relationship between the surface potential and gas pressure with different materials (mica, sapphire, quartz, and Teflon) and incident beam energies inside air atmosphere are shown from figure 3.21 through figure 3.25. Overall the relationship is similar with that of figure 3.7, in which the surface potential varies logarithmically with gas pressure at lower gas pressure part and independent with gas pressure at higher gas pressure region. The effect of materials on the shape of the curve exists on the initial surface potential value, the charging reduction efficiency, the charging balance pressure, and the value of the stable state surface potential. It is also shown that sample characteristic properties, including composition, dielectric constant, and permittivity, strongly influence local charge effects, which can significantly affect the primary electron landing energy and consequently the resultant emitted x-ray signal under low-pressure environments [Griffin 2003].

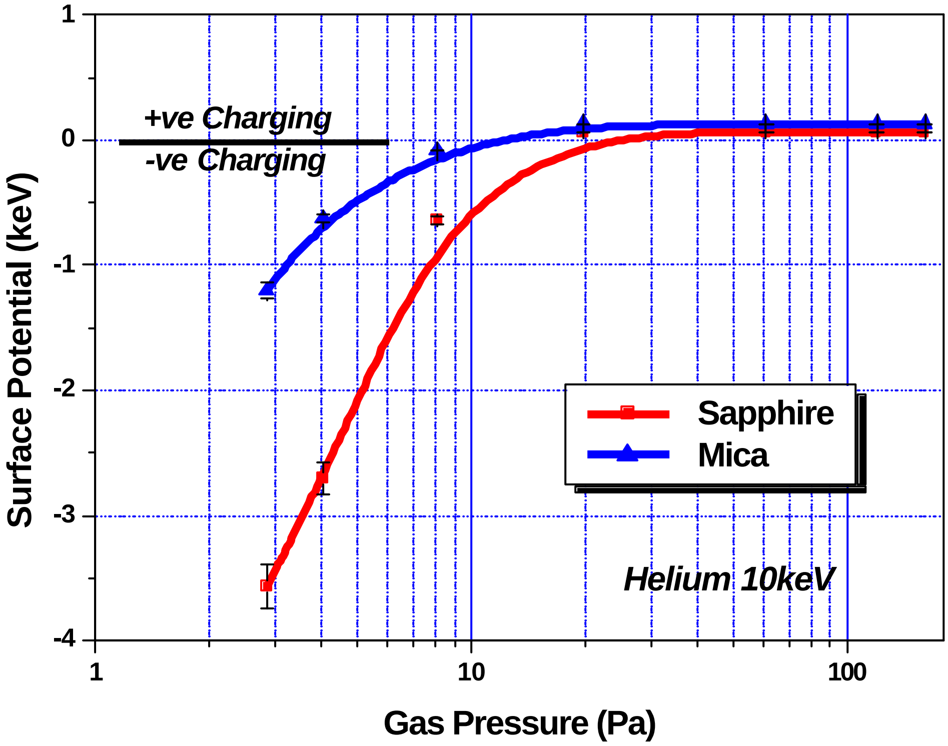

Figure 3.20 Surface potential on sapphire and mica varies as a function of gas pressure by 10keV beam irradiation within helium atmosphere. The acquisition time for the x-ray spectrum was 100 seconds. The plate electrode of the SE detector is in SSE mode. The magnification is 90×. Working distance is 12mm. No objective aperture.

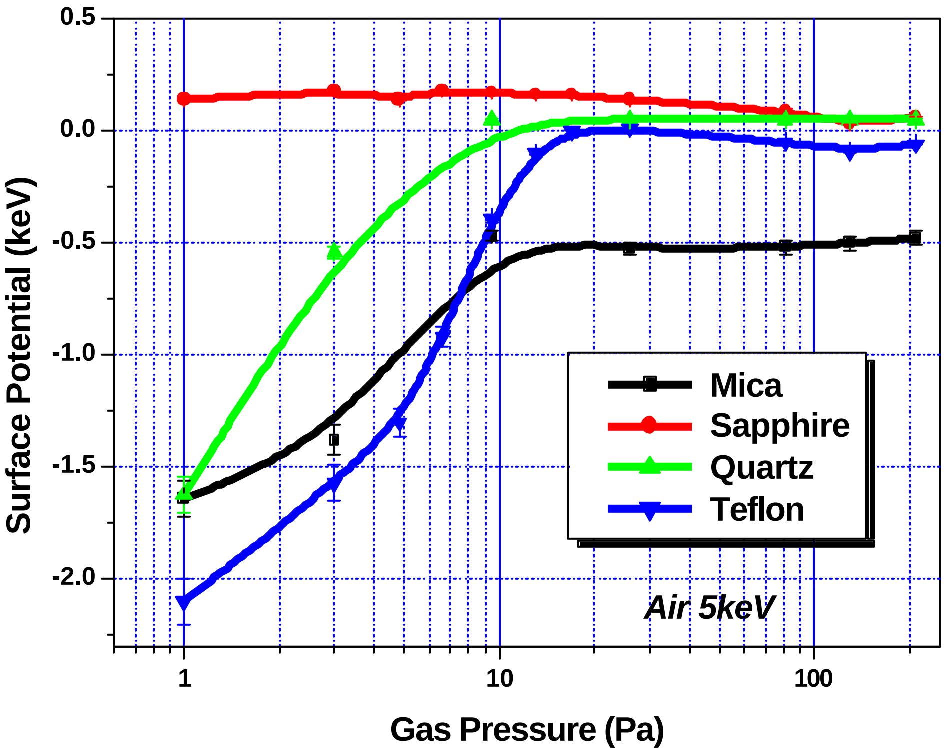

Figure 3.21 Surface potentials on sapphire, mica, quartz, and Teflon vary as a function of gas pressure by 5keV beam irradiation within air atmosphere. The acquisition time for the x-ray spectrum was 100 seconds. The plate electrode of the SE detector is in SSE mode. The magnification is 90×. Working distance is 12mm. No objective aperture.

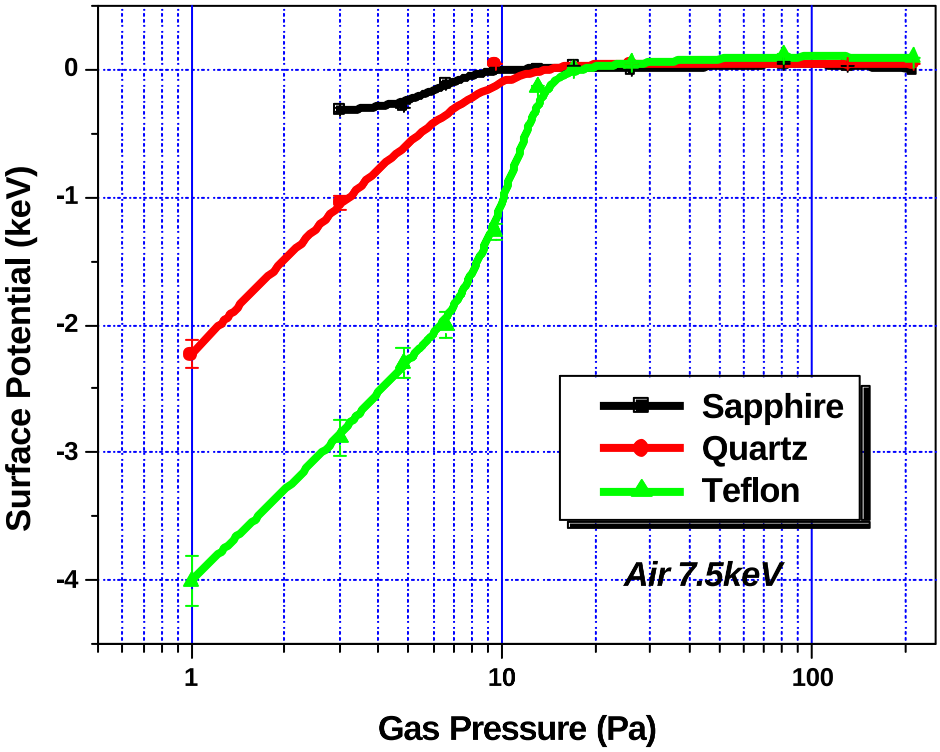

Figure 3.22 Surface potentials on sapphire, quartz, and Teflon vary as a function of gas pressure by 7.5keV beam irradiation within air atmosphere. The acquisition time for the x-ray spectrum was 100 seconds. The plate electrode of the SE detector is in SSE mode. The magnification is 90×. Working distance is 12mm. No objective aperture.

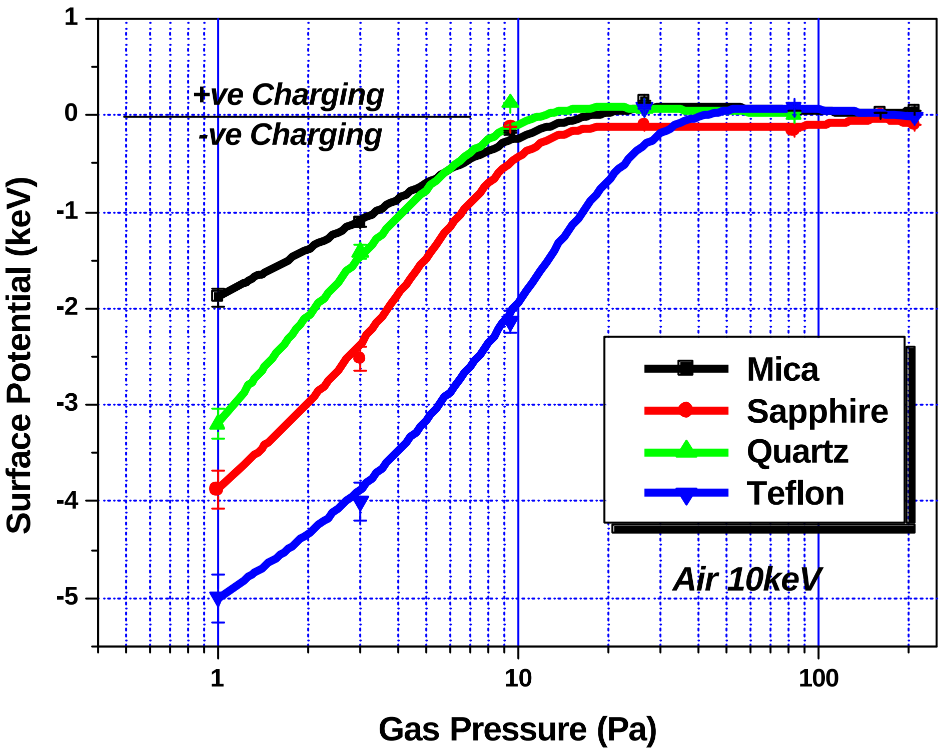

Figure 3.23 Surface potentials on sapphire, mica, quartz, and Teflon vary as a function of gas pressure by 10keV beam irradiation within air atmosphere. The acquisition time for the x-ray spectrum was 100 seconds. The plate electrode of the SE detector is in SSE mode. The magnification is 90×. Working distance is 12mm. No objective aperture.

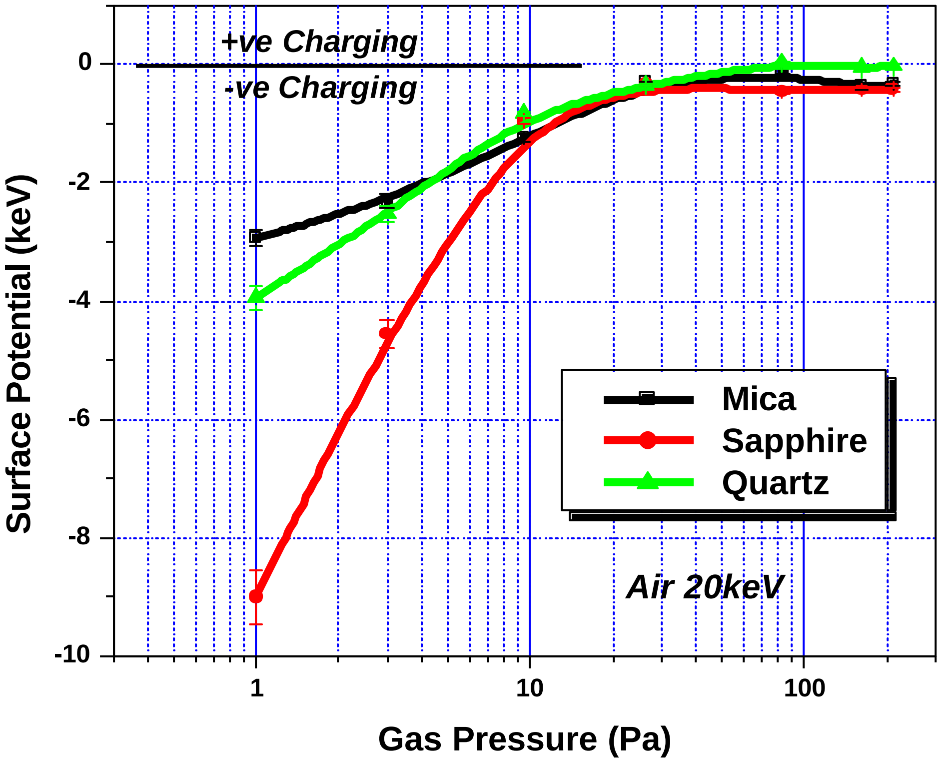

Figure 3.24 Surface potentials on sapphire, mica, and quartz vary as a function of gas pressure by 20keV beam irradiation within air atmosphere. The acquisition time for the x-ray spectrum was 100 seconds. The plate electrode of the SE detector is in SSE mode. The magnification is 90×. Working distance is 12mm. No objective aperture.

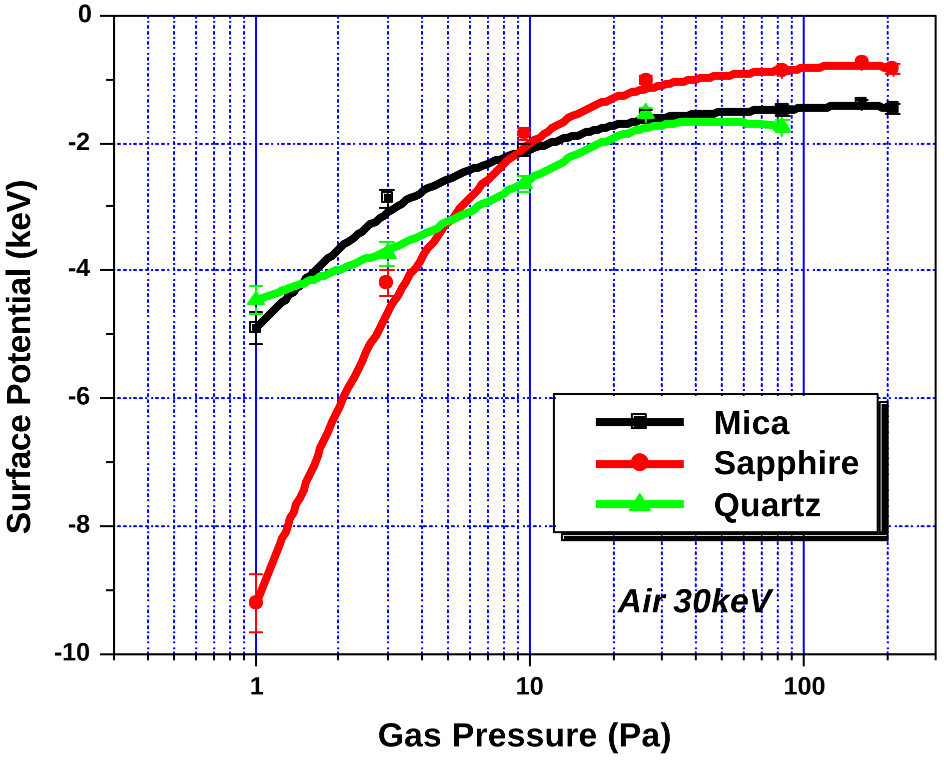

Figure 3.25 Surface potentials on sapphire, mica, and quartz vary as a function of gas pressure by 30keV beam irradiation within air atmosphere. The acquisition time for the x-ray spectrum was 100 seconds. The plate electrode of the SE detector is in SSE mode. The magnification is 90×. Working distance is 12mm. No objective aperture.

Data listed in table 3.4, which including the charging balance pressure, the charging reduction efficiency, and the surface potential at the stable state, show the effect of material type on the surface for various gases and materials. As the beam energy increases, the charging deduction efficiency also increases and the charging balance pressure keeps constant or slowly rise, while the stable surface potential moves more negative.

Figure 3.26 shows the relationship of surface potential and gas pressure as the function of beam energy on the surface of EUV reflective mask (Mo/Si multi-layer on Si wafer). As a kind of conductive layer, the surface potential is always stay positively except when the beam energy reaches 30keV, which is attributed by the penetration of incident electrons passing through multi-layer and reaching the substrate.

3.4.4 Effect of Surface Roughness on Charge Reduction

Figure 3.27 shows the variation of the surface potential with gas pressure (air) and surface roughness on mica at a given beam energy (20keV). Apparently the smooth surface was charged more negative than that of the rough surface within the whole pressure range, but the difference between these two curves decreases from about 800 volts in the low-pressure region to about 60 volts when surface stabilizes. On the other hand, each curve has the same CRE in lower pressure region. In both cases, the surface potential stabilized at a negative value. Surface roughness, on a scale comparable with the beam interaction volume, enlarges the effective surface area and hence the secondary electron emission. It is this effect that leads to the observed charging reduction. This effect has been used to example difficult materials. For example Teflon "roughened" by plasma etching can be viewed readily without coating in many cases.

The phenomena above can be explained by the production principle of the secondary electron. The SE yield of rough surface is larger than that of smooth surface because the rough surface equals to enlarge the effective area, or the real area. The surface potential is closely

Table 3.4 Comparison P^*, CRE, and V_{stable} for different beam energy and materials type in air environment

Beam Energy (keV)	Mica			Sapphire			Quartz			Teflon		
	P^*	K	V_{stable}	P^*	K	V_{stable}	P^*	K	V_{stable}	P^*	K	V_{stable}
5	NA	1.2	-0.5	NA	0	0.16	11	1.7	0.05	11	2.8	-0.1
7.5	--	–	--	9	0.7	-0.3	14	2.3	0.04	11	6.3	0.1
10	12	1.86	0.04	NA	4.9	-0.1	19	3.1	0.04	11	7.9	0.1
15	11	2.11	0.03	NA	5.4	-0.2	–	--	--	--	--	--
20	NA	2.14	-0.35	NA	9.3	-0.4	82	3	-0.1	--	--	--
30	NA	4.25	-1.4	NA	16.2	-0.8	NA	2.8	-1.7	--	--	--

Note: P^* (Pa) is the value of the charging balance pressure, K can be regarded as a measure of the charge reduction efficiency (CRE) $\Delta V / \Delta \log P$, and V_{stable} (keV) is the value of the surface potential at the stable state. For air on sapphire at 5keV, the surface potential maintains a positive value.

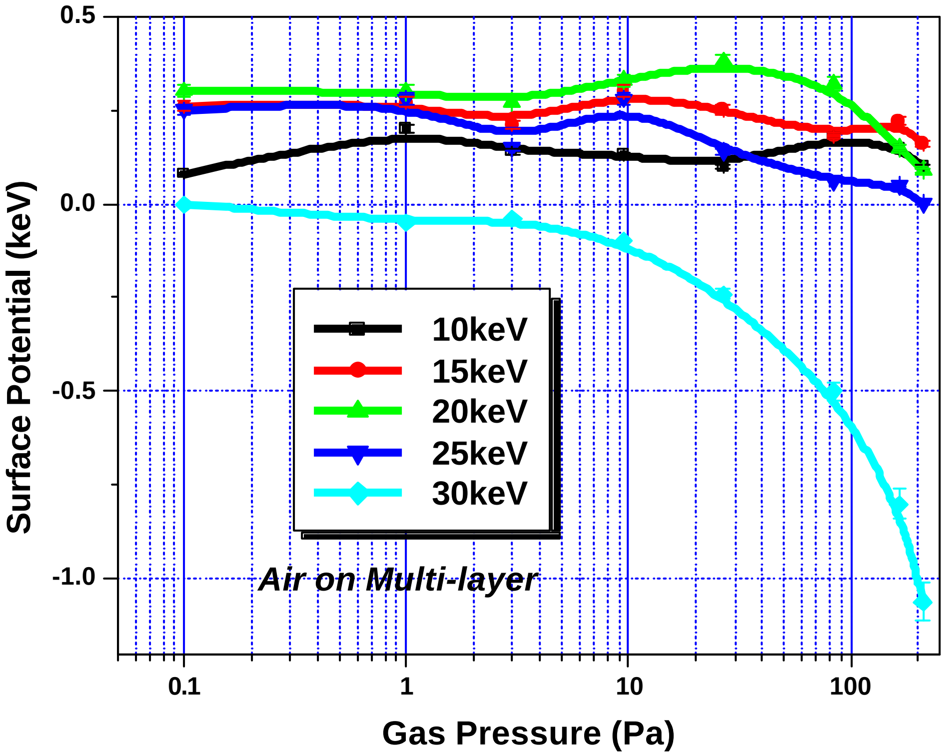

Figure 3.26 Surface potential on a x-ray lithography multi-layer mask containing TaN-Oxide-Mo-Si, as a function of gas pressure and beam energy under the irradiation of 10, 15, 20, 25, and 30keV electron beam within air atmosphere. Sample size is 2× 2× 0.2cm. The acquisition time for the x-ray spectrum was 100 seconds. The plate electrode of the SE detector is in SSE mode. The magnification is 90×. Working distance is 12mm. No objective aperture.

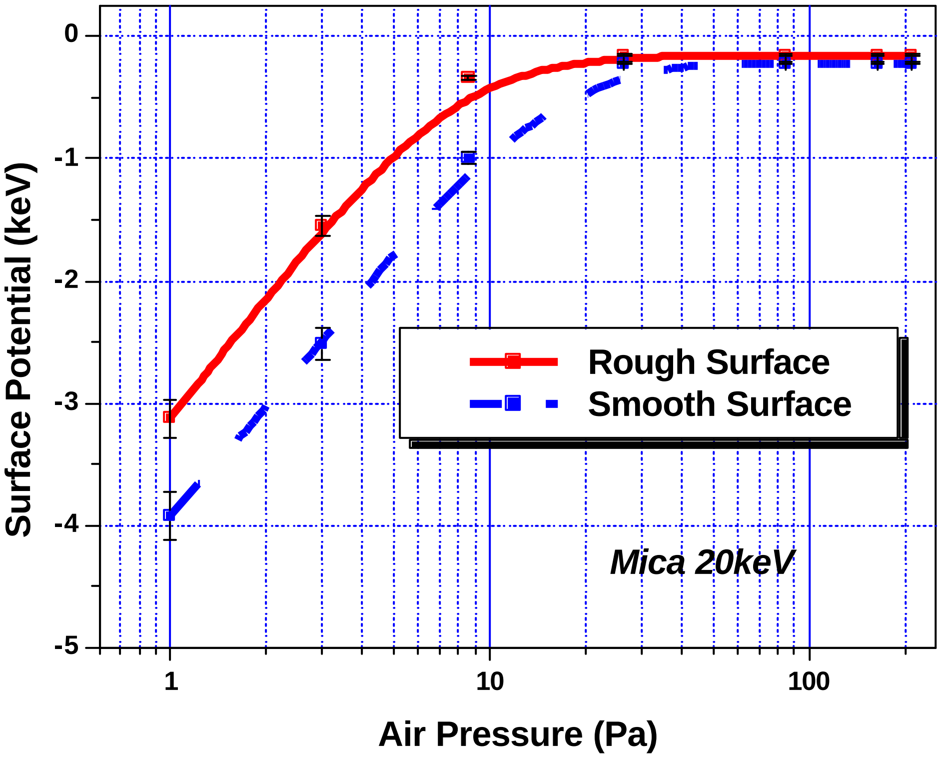

Figure 3.27 Surface potential of mica varies as a function of gas (air) pressure by 10keV beam irradiation with varying surface roughness. The acquisition time for the x-ray spectrum was 100 seconds. The plate electrode of the SE detector is in SSE mode.

related with the SE yield, especially in a gaseous environment because it is the SE which initiates the ionization process.

3.4.5 Effect of Detector Bias Voltage on Charge Reduction

In the Hitachi S3500N VP-SEM used for these experiments there is an electrode, placed just below and to one side of the objective lens, whose function is to enhance the collection efficiency of the secondary electron detector. The potential on this electrode can be varied from 150 to 350 volts. Figure 3.28 shows the results of varying the electrode potential while observing mica under 20keV electron beam in air. Higher electrode bias causes larger surface potential at 1Pa and a larger CRE when gas pressure increases until all three curves merge into stable state at some gas pressure. The bias voltage on electrode can create electric field with charged sample surface to assist the gas ionization process so as to remove surface charging. Since the working distance is fixed (12mm) in this experiment, the intensity of electric field is directly proportional to the voltage which creates the electric field, varying from 130 to 290 volts/cm.

3.4.6 Effect of Sample Tilt on Charge Reduction

As an important factor, the sample tilt affects the secondary electron productive efficiency so as to affect the resulting surface charging condition. The SE yield d_q at some angle q is related to the yield d_0 at normal incidence by [Seiler 1983]

$$d_q = {d_0}\big/{\cos q} \tag{3.6}$$

Some factors will affect d like sample tilt angle, surface roughness, beam energy, and sample composition. As shown in figure 3.29, sample tilting not only changes the surface potential at given gas pressure, but the charging reduction efficiency (CRE). The higher the sample tilts, the

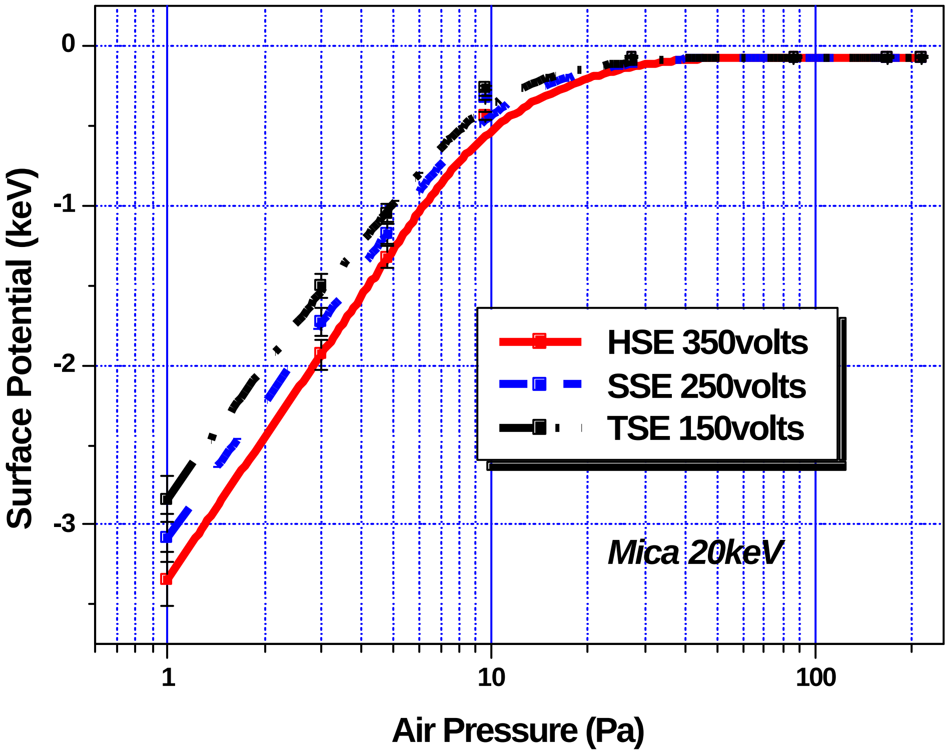

Figure 3.28 Surface potential of mica varies as a function of the gas (air) pressure with the effect of different electrode voltages. HSE: High-resolution SE mode; SSE: standard SE mode; TSE: topography SE mode. Primary beam energy is 20keV. The acquisition time for the x-ray spectrum was 100 seconds.

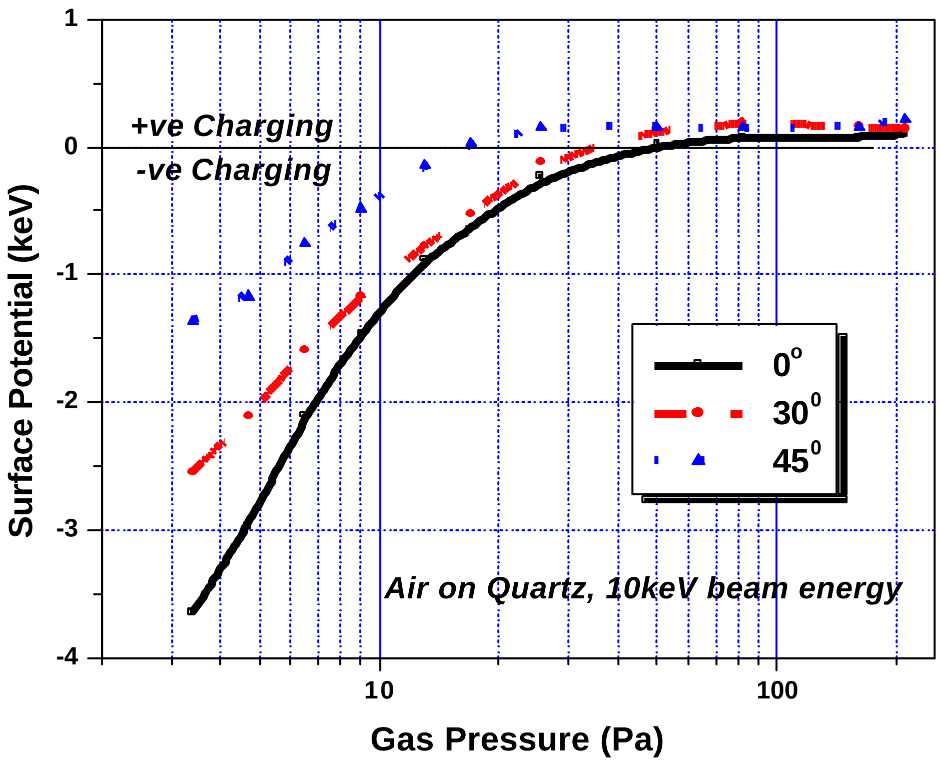

Figure 3.29 Surface potential of quartz varies as a function of the gas (air) pressure with the effect of sample tilt angle. Primary beam energy is 10keV. The acquisition time for the x-ray spectrum was 100 seconds. Magnification is 5000× and the working distance as 12mm. The plate electrode of the SE detector is in SSE mode.

lower the surface potential, and the lower the CRE. It can be shown that

$$E_2(q) = E_2(0) / \cos^2 q \qquad 3.7$$

Since E_2 varies with the angle of incidence the "no charge" condition can never be satisfied everywhere on the surface at the same time and charging will always occur on samples with surface topography [Joy 1987]. Meanwhile, although this drawback can be alleviated by increasing the magnification, as figure 3.30 shows, higher magnification means higher impinging electron density and higher surface potential. Thus the high magnification is used in order to alleviate the effect of working distance which varies due to the sample tilt.

3.4.7 Effect of Magnification on Charge Reduction

Figure 3.31 and 3.32 show how the surface potential varies with magnification. For the case of quartz in air, lower magnification corresponds to smaller CRE and surface potential at low gas pressure while for sapphire in air, CRE is independent on magnification but lower magnification relates to a smaller charging. The irradiation magnification will change the incident electron dose since such dose density is determined by the primary electron density divided by the irradiation area

$$r = I / A \qquad 3.8$$

here r is the dose density, A the scanning area, which is inversely proportional to the square of the magnification. Higher magnification corresponds higher dose density so that the electric field created by surplus surface charge is intensified. As a result, the surface potential increased. Within some range, lower magnification can alleviate surface charging.

The experimental data show that charging depends not only the beam current, but also on the current density. This "dynamic charging effect" is probably due to electron-hole generation in the insulator. It is this effect which makes possible the "scan square" method for finding the E_2

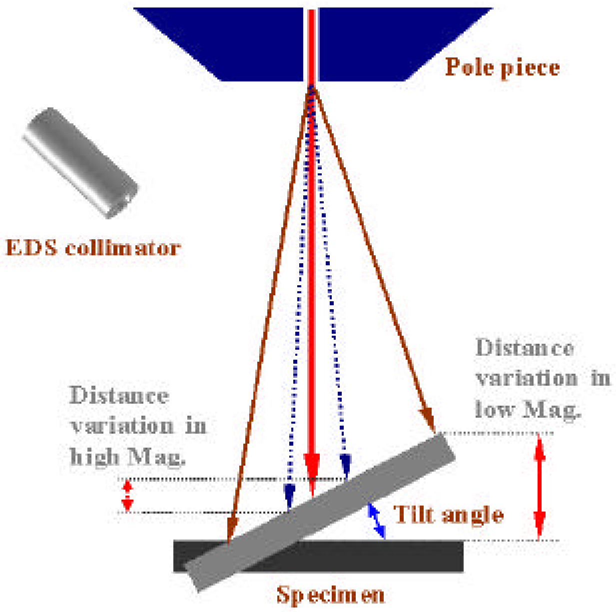

(a)

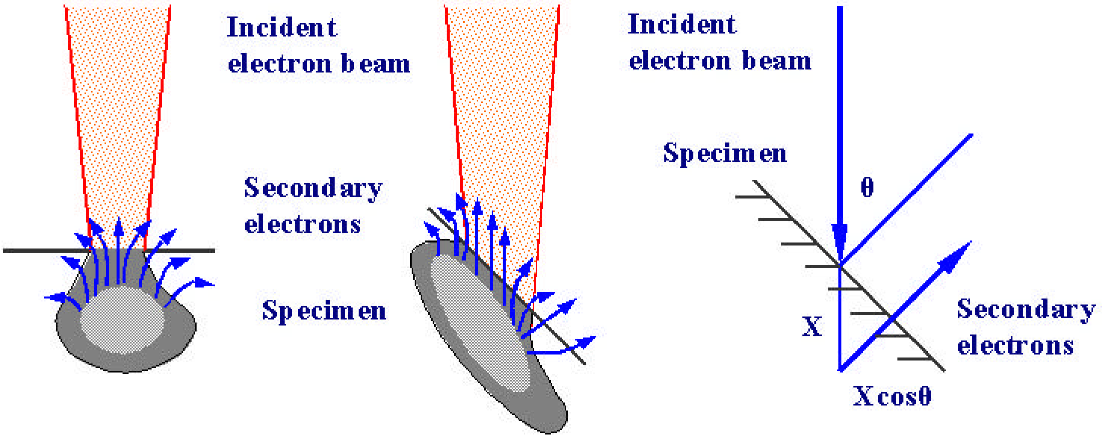

(b)

Figure 3.30 Schematically draw the sample tilt set up (a) The amount of secondary electrons generated depends on the specimen tilt angle (b)

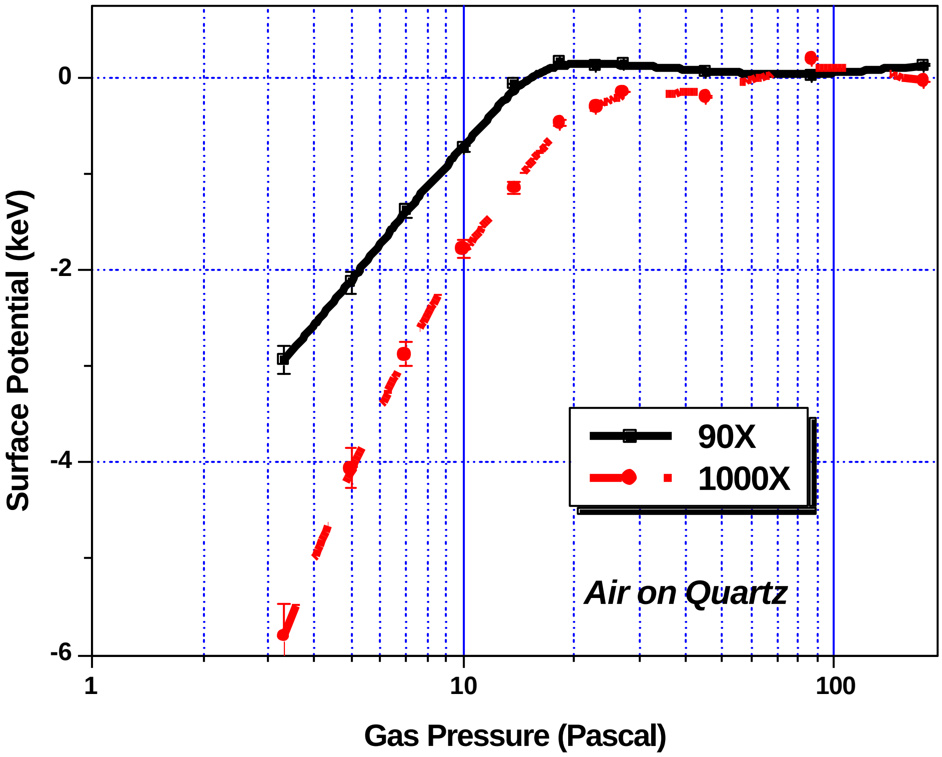

Figure 3.31 Surface potential of quartz varies as a function of the gas (air) pressure with the effect of magnification. Primary beam energy is 15keV. The acquisition time for the x-ray spectrum was 100 seconds. Magnification is 90× and 1000× and the working distance as 12mm. The plate electrode of the SE detector is in SSE mode.

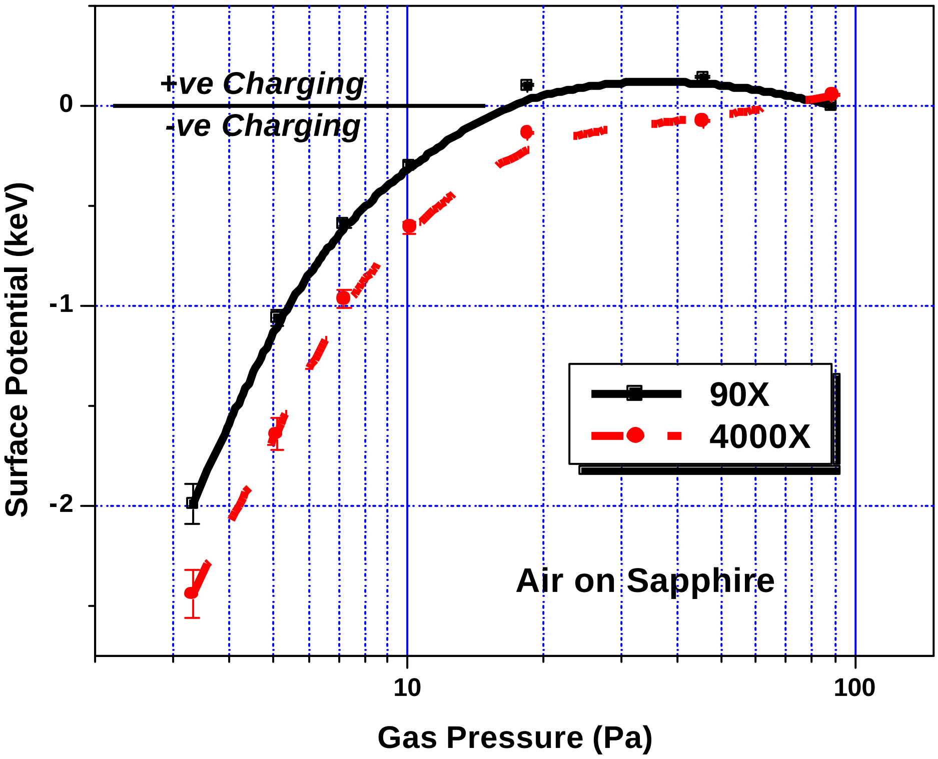

Figure 3.32 Surface potential of sapphire varies as a function of the gas (air) pressure with the effect of magnification. Primary beam energy is 20keV. The acquisition time for the x-ray spectrum was 100 seconds. Magnification is 90× and 4000× and the working distance as 12mm. The plate electrode of the SE detector is in SSE mode.

energy. This method bases on the principle that the sample surface acquires a positive or negative charge as evidenced from the black or white "scan square" that is visible on the image after exposure [Joy 2004].

3.4.8 Effect of Scanning Speed on Charge Reduction

The scanning mode will affect the charge distribution on the irradiation area due to the electron impinge rate at specific area in unit time. Figure 3.33 illustrates the effect of scanning speed on surface charging. The fast scan caused a more negative initial surface potential but higher CRE value thus both curves can reach the same value of surface voltage at stable state.

Charging is time dependent because the system acts like a resistor/capacitor combination with time constant $t = CR$. The charging/scan speed behavior varies with the rate of charge-up and of discharge.

3.4.9 Aperture Effect

In an SEM, the objective aperture is used to limit the final electron current flux striking on the sample surface. Decreasing the diameter of the aperture decreases the incident electron current and hence the deposited dose density as a function of magnification.

Figure 3.34 shows the effect of objective aperture and gas pressure on the surface potential of quartz in air environment under the irradiation of 10keV electron beam. As the aperture diameter decreases, the surface potential moves positively especially for low gas pressure condition. The surface potential tends to independent on the aperture size when the gas pressure increases. In low gas pressure condition, lower the density of the incident electron, fewer trapped electrons inside the sample thus lower charge density which results more positive surface

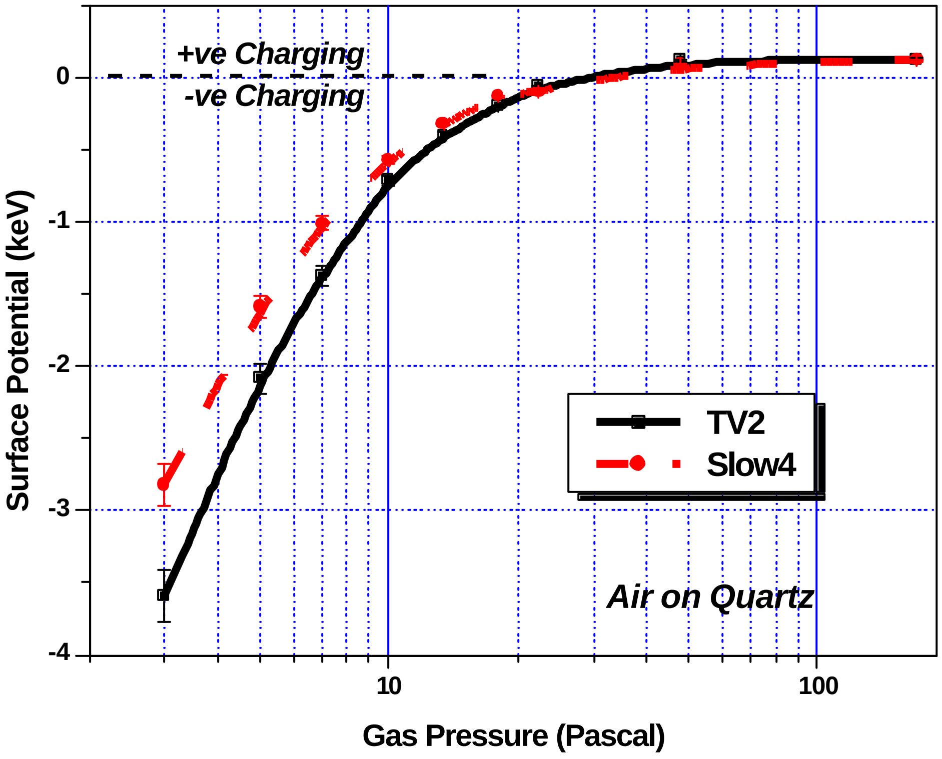

Figure 3.33 Surface potential of quartz varies as a function of the gas (air) pressure with the effect of magnification. Primary beam energy is 20keV. The acquisition time for the x-ray spectrum was 100 seconds. Magnification is 90× and 4000× and the working distance as 12mm. The plate electrode of the SE detector is in SSE mode.

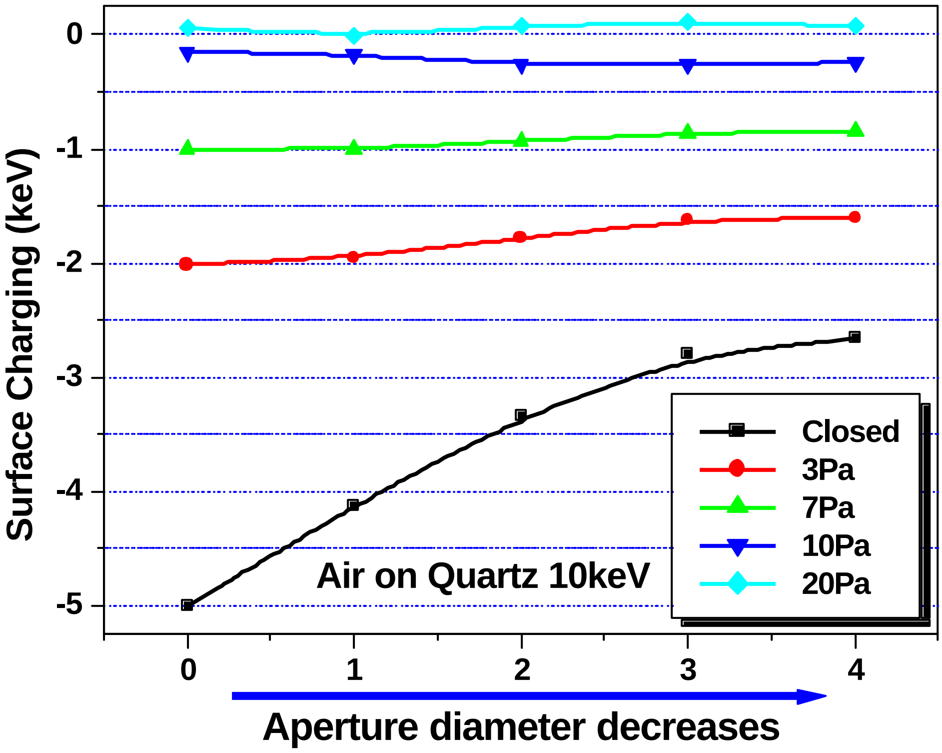

Figure 3.34 Surface potential of quartz varies as the function of gas pressure with the effect of aperture in air atmosphere varying as closed, 3Pa, 7Pa, 10Pa, and 20Pa. Primary beam energy is 10keV. Aperture diameter decreases as the sequence of 0, 1, 2, 3, and 4. The acquisition time for the x-ray spectrum was 100 seconds. Magnification is 90× and the working distance as 12mm. The plate electrode of the SE detector is in SSE mode.

potential. When gas pressure increases, the ionization and beam skirting have larger effect on surface charging neutralization than that of incident electron density.

3.4.10 X-Ray Collection Time Effect

Figure 3.35 shows how the x-ray collecting time affects the surface potential measurement. At low gas pressure part, longer x-ray collecting time means less negative surface potential while the surface potential is not sensitive to the collecting time at high gas pressure region.

In low gas pressure, longer collection time corresponds to lower surface charging and may produce more reliable and reproducible x-ray data because the high-energy cutoff is more distinct. But surface charging is a kind of dynamic process and a quick measurement is more favorable, especially for some bad charging conditions like dielectric breakdown.

3.4.11 Working Distance Effect on Sample Current

Working distance in SEM is defined as the distance between the objective lens and sample surface. Depth of field is strongly dependent on changes of working distance. The effect of working distance on sample current is shown in figure 3.36 on quartz surface in 10Pa air under different beam energy as 10keV and 20keV. Both curves have a peak value of sample current through the changing range of working distance.

Gas path length (or working distance) will not affect the MFP (mean free path) but the gas cascade process at a fixed pressure. When the working distance is short, the emitted SE has less opportunity to ionize gas molecule within the gas cascade process until a threshold value of working distance is reached [Toth 2002]. But if the working distance is too long, the self-damping effect, which comes from the varied electric field by charging neutralization, will limit the sample

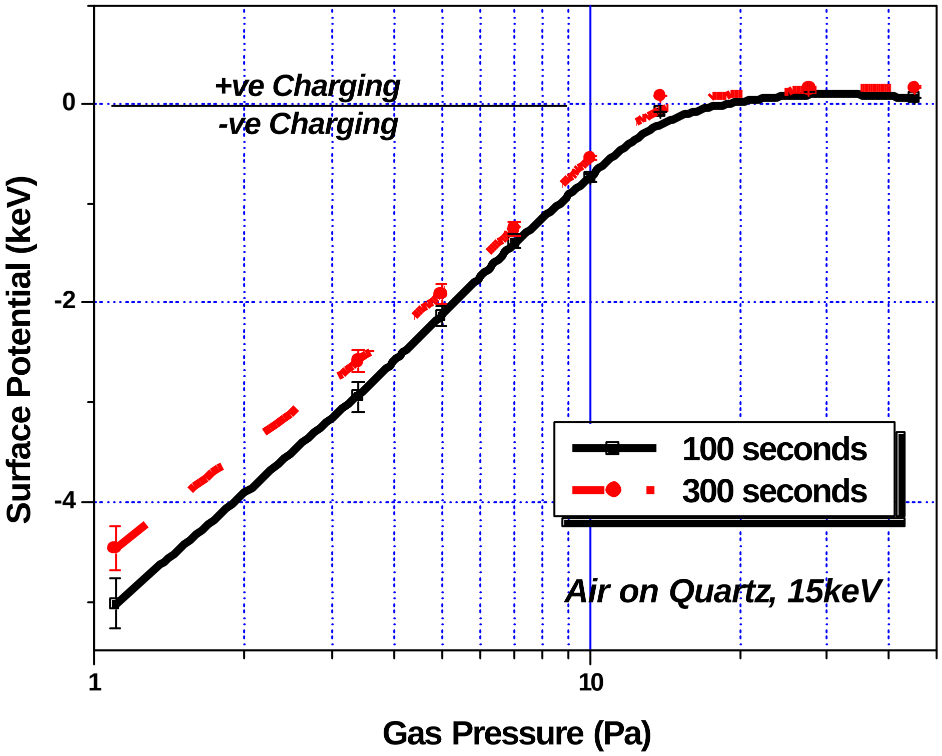

Figure 3.35 Test the effect of the x-ray spectrum collection time (100 and 300 seconds) on the value of the Duane-Hunt limit. All the data are taken from quartz surface at 15keV beam energy in air environment. The plate electrode of the SE detector is on SSE mode. The magnification is 90×. Working distance is 12mm. No objective aperture.

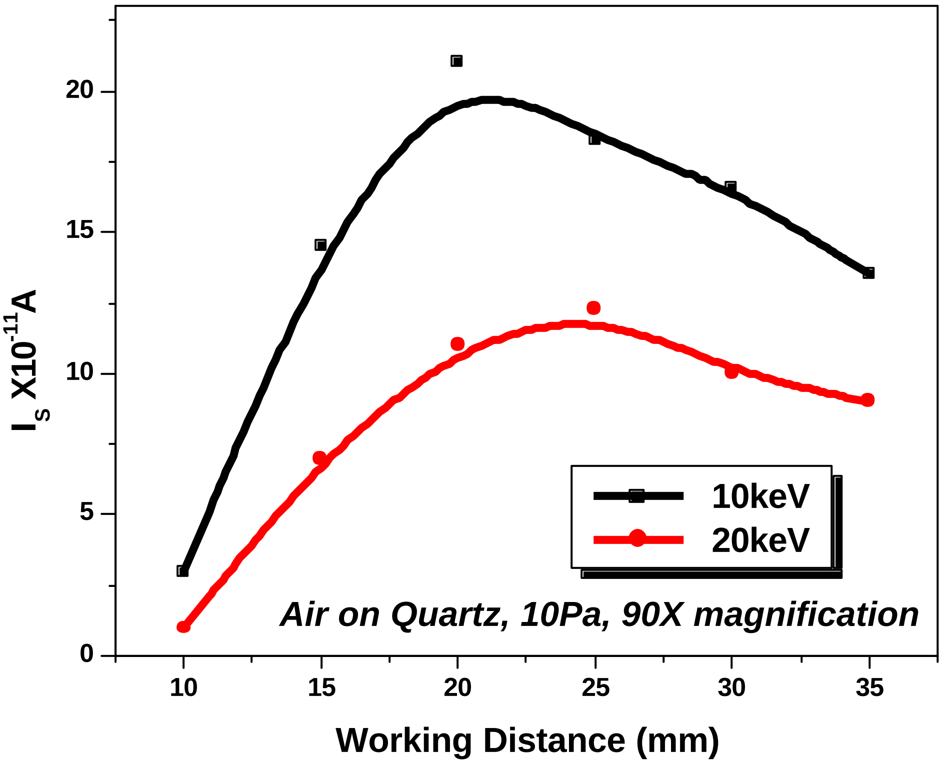

Figure 3.36 Schematically show the relationship of working distance and sample current on quartz in 10Pa air environment by 10 and 20keV beam irradiation. Magnification is 90×. The plate electrode of the SE detector is in SSE mode.

current. Sample current will be discussed in detail later. Nevertheless, changing the working distance is not good to measure the surface potential when employing EDS due to the take off angle of the detector and EDS collection efficiency.

3.4.12 Sample Size Effect

As specimen charging is a kind of process determined by multiple factors, the sample size plays an important role. The sample size effects on the surface potential and specimen current are illustrated in figure 3.37 and 3.38 Different size (Large 20×20×1mm and Small 3×2×1mm) quartzes are irradiated by 15keV electron beam in different gas pressure atmosphere. The surface potential of large sample is more positive than that of small one, and the value becomes less negative when gas pressure increases. The size effect on surface potential varies with the static permittivity and the space charge distribution, which can be explained by charge diffusion and polarization relaxation processes resulting from the space charge formation. The amount of charges trapped is approximately inversely proportional to the size (here is A) of the sample. The charge density of a large specimen decreases much faster than that of a small one. Therefore the charge in a large sample is widely spread while a small sample has the charge concentrated near the vicinity of the electron beam [Oh et al. 1993].

The sample current of large sample is higher than that of small one though it does not follow the variation of gas pressure. The variation of sample current with the change of sample size can be described by formula $I_{sc} = V_{sc} / R$, here I_{sc} is sample current, V_{sc} surface potential, R is the sample bulk resistance along the direction of incident beam and determined by $R = r_T d / A$, z sample thickness, A sample area, r_T resistivity. Although the specimen current read from the ampere meter is the sum of displacement current and leakage current, the analysis of specimen current can be treated on leakage current only since the displacement current is not

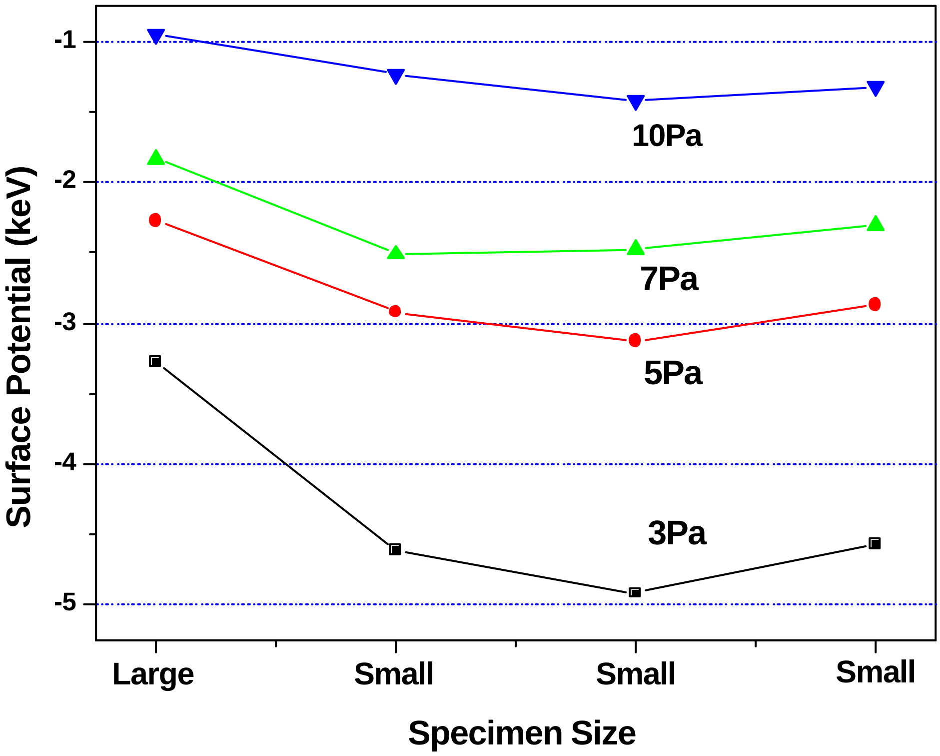

Figure 3.37 The effect of sample size on surface potential in air environment, pressure varies from 3, 5, 7, to 10Pa. Sample sizes are large (20×20×1mm) and small (3×2×1mm). Incident beam energy is 15keV. Magnification is 90×. The plate electrode of the SE detector is in SSE mode

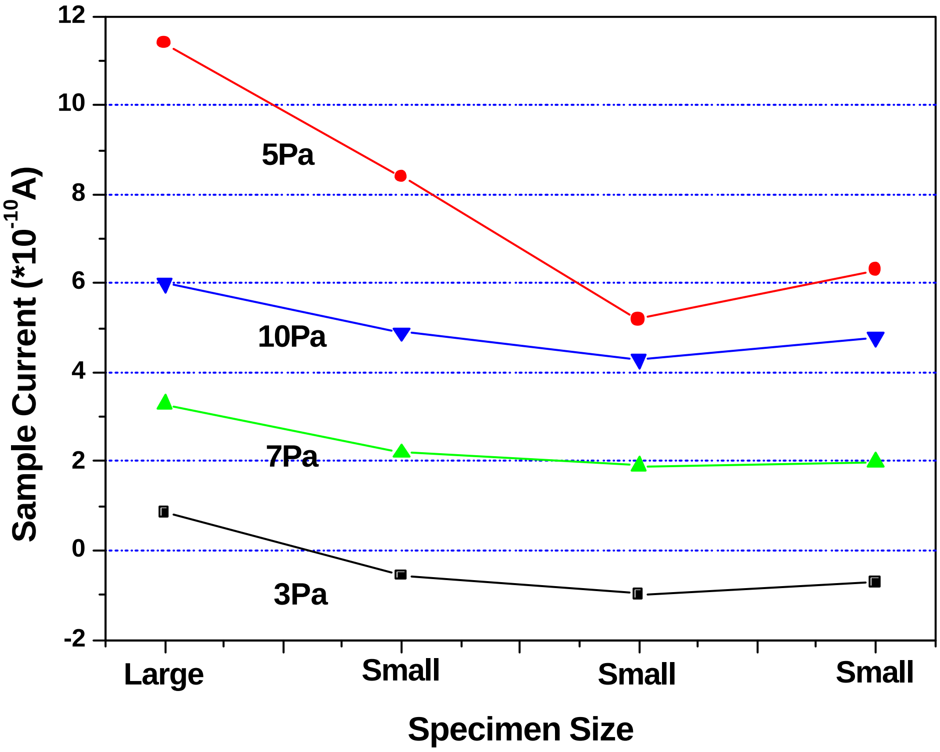

Figure 3.38 The effect of sample size on sample current in air environment, pressure varies from 3, 5, 7, to 10Pa. Sample sizes are large (20×20×1mm) and small (3×2×1mm). Incident beam energy is 15keV. Magnification is 90×. The plate electrode of the SE detector is in SSE mode.

affected by sample size. Thus the specimen current has the relationship with sample size as follows

$$I_{sc} = V_{sc} A / r_T z \qquad 3.9$$

Thus the specimen current is determined by two factors, surface potential and sample area. Experimental data show that the specimen current of large sample is higher than that of small sample though large sample has a less negative surface potential because the sample size effect is higher than that of surface voltage effect.

3.5 Comparison of Duane-Hunt Limit and Peak Ratio Method

Figure 3.39 to 3.41 compare the variation curves of the surface potential with gas pressure obtained from the Duane-Hunt limit experiment and the peak ratio method calculation on quartz surface. The results from different incident beam energies as 5keV, 10keV, and 15keV indicate that both methods have similar trend at intermediate pressure part but differences between these two methods increase at both low and high gas pressure range.

The differences of the surface potential curves between the Duane-Hunt limit method and the peak ratio method are dominant at very low and high gas pressure range, which can be explained as the spectrum distortion by surface charging in low gas pressure region or gas scattering in high gas pressure part. When comparing with the Duane-Hunt limit method, the drawback of the peak ratio method is its inconvenient operation, because each sample with different composition needs different calibration curve. However the peak ratio method is still useful to evaluate the surface potential since the peak ratio of the x-ray spectrum is sensitive to surface potential change and can be a supplemental method to the Duane-Hunt limit in some cases like low beam energy.

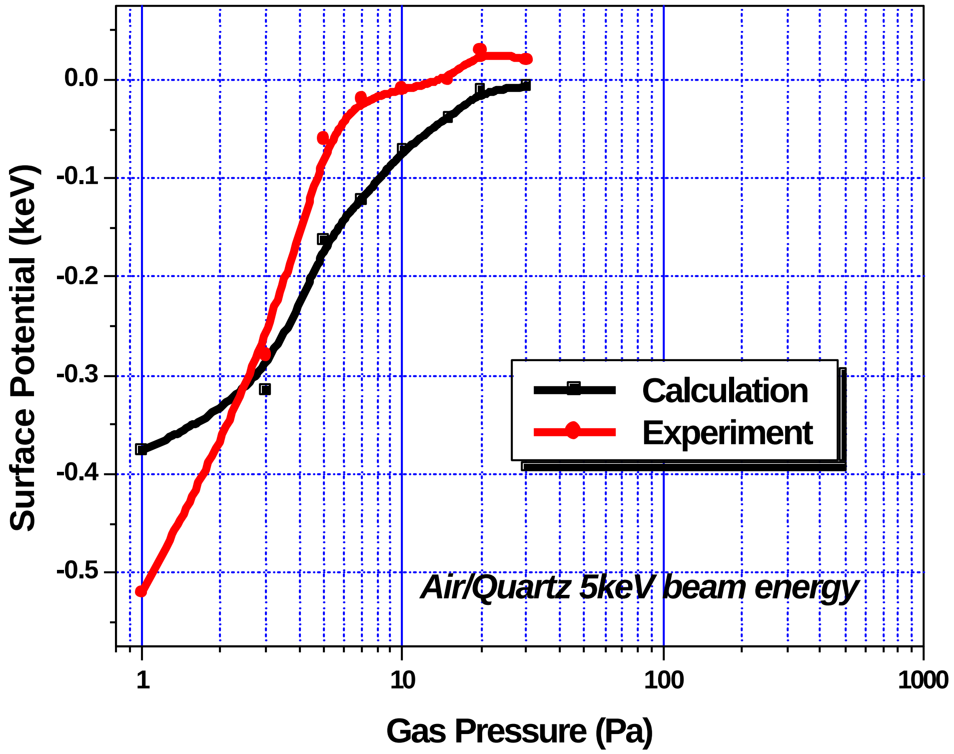

Figure 3.39 Compare the experimental data and the calculation value of the surface potential varying with the air pressure on quartz by 5keV beam irradiation. The acquisition time for the x-ray spectrum was 100 seconds. Magnification is 90× and the working distance as 12mm. The plate electrode of the SE detector is in SSE mode.

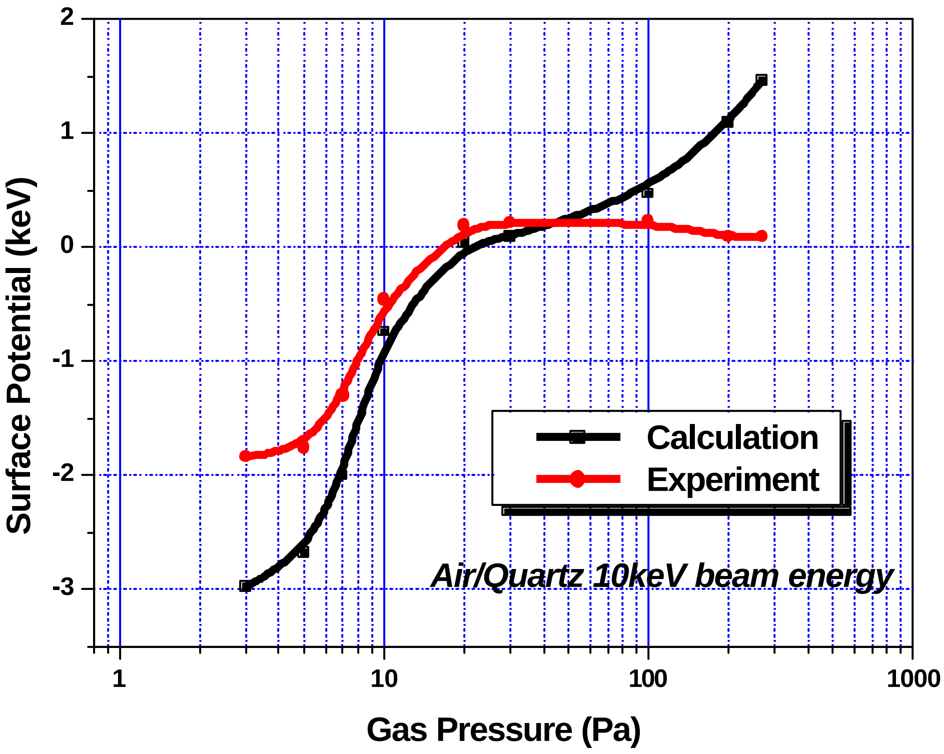

Figure 3.40 Compare the experimental data and the calculation value of the surface potential varying with the air pressure on quartz by 10keV beam irradiation. The acquisition time for the x-ray spectrum was 100 seconds. Magnification is 90× and the working distance as 12mm. The plate electrode of the SE detector is in SSE mode.

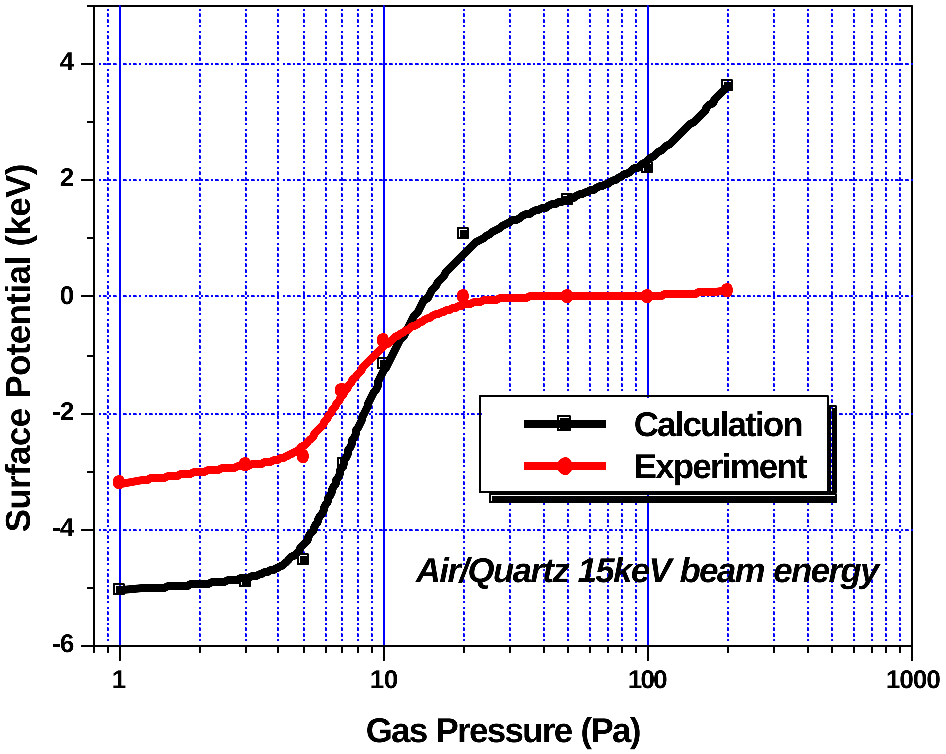

Figure 3.41 Compare the experimental data and the calculation value of the surface potential varying with the air pressure on quartz by 15keV beam irradiation. The acquisition time for the x-ray spectrum was 100 seconds. Magnification is 90× and the working distance as 12mm. The plate electrode of the SE detector is in SSE mode.

3.6 Discussion

Although the general form of the potential variation with pressure is always similar to that shown in figure 3.7, depending on the actual condition chosen, there are significant differences as the initial and stable potential values, charge reduction efficiency, and the charge balance pressure. In order to theoretically explain these phenomena, a model for charge compensation by gas is presented below.

3.6.1 A Model for Charge Compensation by Gas

Incident primary electrons (PE), secondary electrons (SE), and back-scattered electrons (BSE) can interact with gas molecules and produce positive and negative ions. The positive ions will flow to negatively charged regions while the negative ions will go to positively charged areas so as to neutralize surface charge. The electric field off the sample surface due to charging and bias on the electrode accelerates the negative ions, initiating a gas ionization cascade (Figure 2.2). Charge carriers in the gas are PE, BSE, SE, ionized gas molecules, electrons liberated as a consequence of ionizing collisions involving gas molecules (ESE) and electrons liberated by positive ions impact on the sample surface (ESE). The major contribution to the gas cascade comes from the SE emanating from the sample surface, since these have a high interaction cross-section due to their low energy [Toth et al. 2000]. On the other hand, the positive ions have much higher mass than electrons resulting in lower mobility, and ion-gas collisions are easier than electron-gas collisions. All the factors above induce the gas ionization avalanche, producing ion current which takes charge of the charging neutralization. Then the total ion current is given by [Meredith et al. 1996]

$$I_{Amp} = I_{PE}Pk\left(S_{PE} + \frac{da}{P} + hS_{BSE}\frac{\bar{d}}{d} \right) \tag{3.10}$$

here I_{PE} is the primary beam current, P is gas pressure, GPL the sample-to-electrode distance in mm, $\overline{d}$ the BSE path length in mm, S_{PE} and S_{BSE} are the field-independent ionization efficiencies of the primary electrons and BS electrons, d and h the SE and BSE coefficients, and quantity k relates to the effects of positive ion impact at the cathode and is given by

$$k = \frac{\exp(ad)-1}{a\{1-l_T[\exp(ad)-1]\}} \qquad 3.11$$

where a and l_T are the Townsend first and second ionization coefficient respectively [Robinson 1975]. Since the final amplified ion current is consisted by three parts (primary electron, back-scattered electron, and secondary electron), figure 3.42 schematically show their contribution separately.

This figure illustrates that there exists a peak for each curve, and the main contribution to total ion current comes from SE in low gas pressure and from PE in high gas pressure. As the ion current plays an important role in charging neutralization, the experimental and theoretical results about ion current vs. gas pressure are compared in figure 3.43.

The discrepancy between the curves lies in many factors since experimental conditions varied as condenser lens adjustment, which is responsible to keep the dead time of the EDS detector as optimum (around 30%).

In order to eliminate the probe current effect on the specimen current by varying the condenser lens current, a calibration curve shown in figure 3.44 is needed, which is measured by the Faraday's cup in high vacuum condition. After the coarse value correction, following factors are attributed to the differences between these two curves: the charging neutralization efficiency, resulting from the cross-section of charge neutralization and beam skirting; contamination layer on the surface, which can be the surface oxide (for pure material) and contaminant (mainly water) or carbon layer stimulated by electrons. The main influence of the secondary electron yield of insulator is the purity. Thicker the surface water contamination layer, higher the secondary

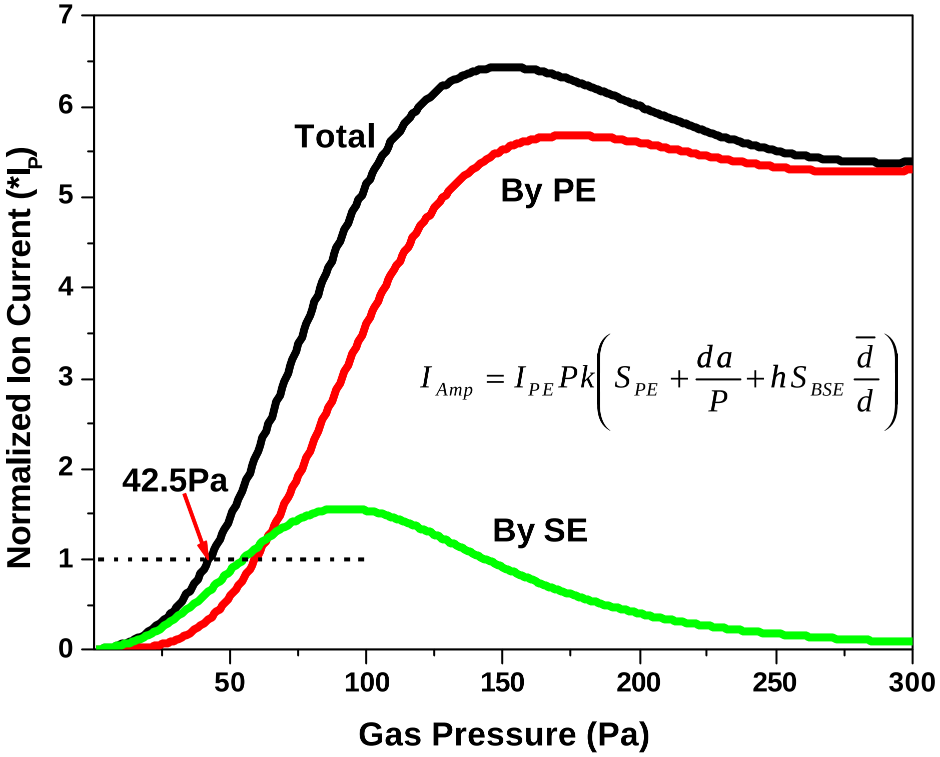

Figure 3.42 Schematic plot of the contribution of ion current from primary electron (PE) and secondary electron (SE) vary as the function of gas pressure. The contribution of back-scattered electron (BSE) is neglected due to its low value.

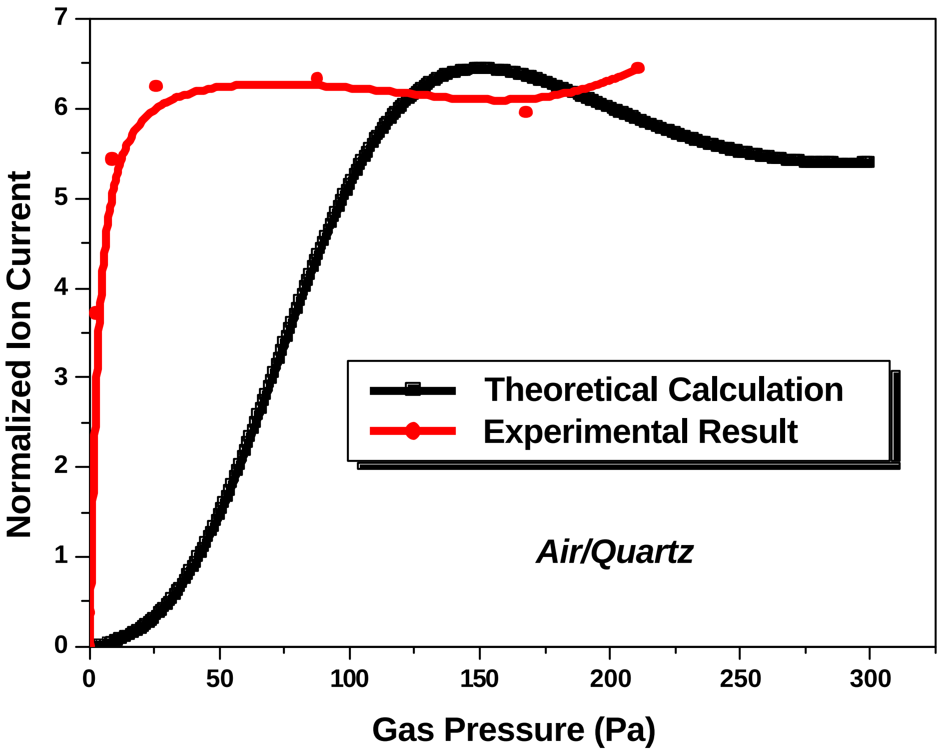

Figure 3.43 The comparison of the experimental measurement and theoretical calculation data on ion current vs. gas pressure. Calculation is based on the experimental condition as 15keV electron beam on the quartz surface in air environment.

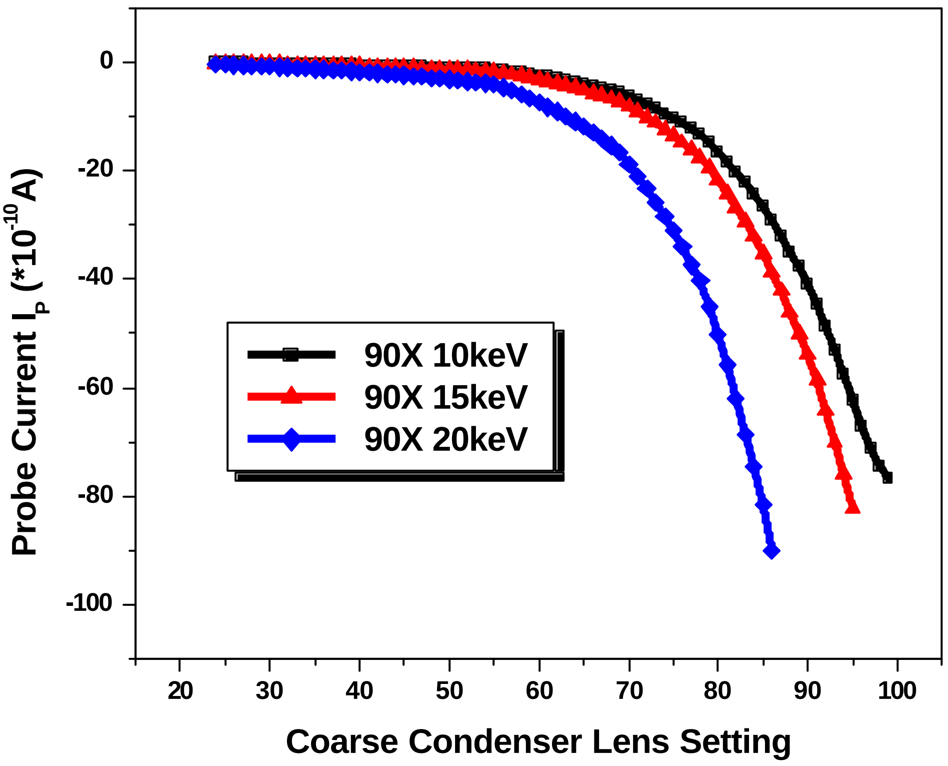

Figure 3.44 Calibration curves of coarse condenser lens setting vs. probe current in high vacuum condition

electron yield; and the recombination effect of gas at the near surface region. Figure 3.45 shows the comparison curve after correcting the coarse adjustment.

Specifically, a contamination layer can form directly after the introduction of the gas. During electron beam irradiation, several organic compounds occur in the gas, which can form a contamination layer even within the short time after the gas input [Pfefferkorn et al. 1972]. Contamination can arise within the microscope column or can exist outside the microscope, but the mostly concern is the cracking of hydrocarbons from the vacuum pumps, grease on o-rings, and lubricants on mechanical parts by the primary electron beam. The contamination can deposit on apertures and pole pieces but also occurs at anywhere which is irradiated by the electron beam. The biggest source of contamination is probably the specimen, which may be obtained from the laboratory environment which contains many forms of natural and man-made pollutants [Echlin et al. 1975].

Both figure 3.46 and 3.47 show the relationship between surface potential, specimen current, and probe current, which are respectively measured by the Duane-Hunt limit, the specimen current, and the Faraday cup, as the function of gas pressure on quartz surface.

Theoretically the Faraday cup is not suitable for probe current measurement in gaseous environment due to the ion current produced by gas ionization. Here the nominal value of probe current experienced the transition from negative to positive and the radius of incident probe calculated by equation

$$r_s = \frac{364\ Z}{E}\left(\frac{p}{T}\right)^{\frac{1}{2}} WD^{\frac{3}{2}} \qquad 3.12$$

When this value is compared with the size of the inlet of the Faraday cup, it is seen that that all the primary electrons can be collected by the Faraday cup at some pressure value and the secondary electron produced inside the Faraday cup cannot escape, resulting no contribution to the gas ionization cascade. Thus the positive ions to neutralize the primary electron must come from the gas ionization by primary beam, which plays an important role in gas ionization cascade too. Figure 3.48 shows such an effect.

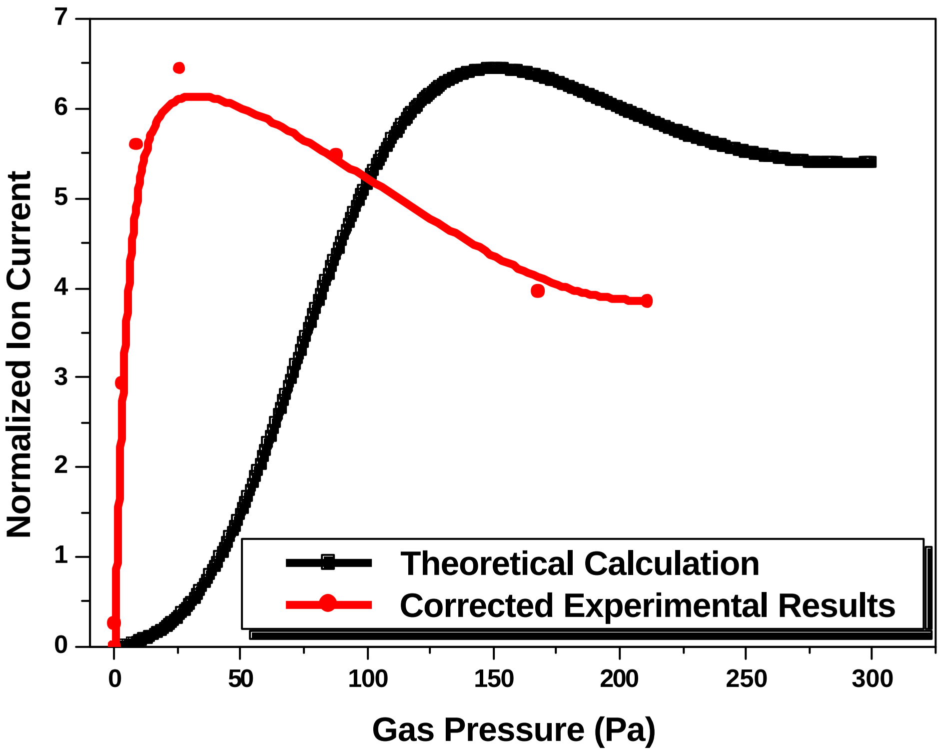

Figure 3.45 Comparison the experimental and theoretical data on ion current vs. gas pressure after the correction of coarse condenser lens setting adjustment. Calculation is based on the data of figure 3.43.

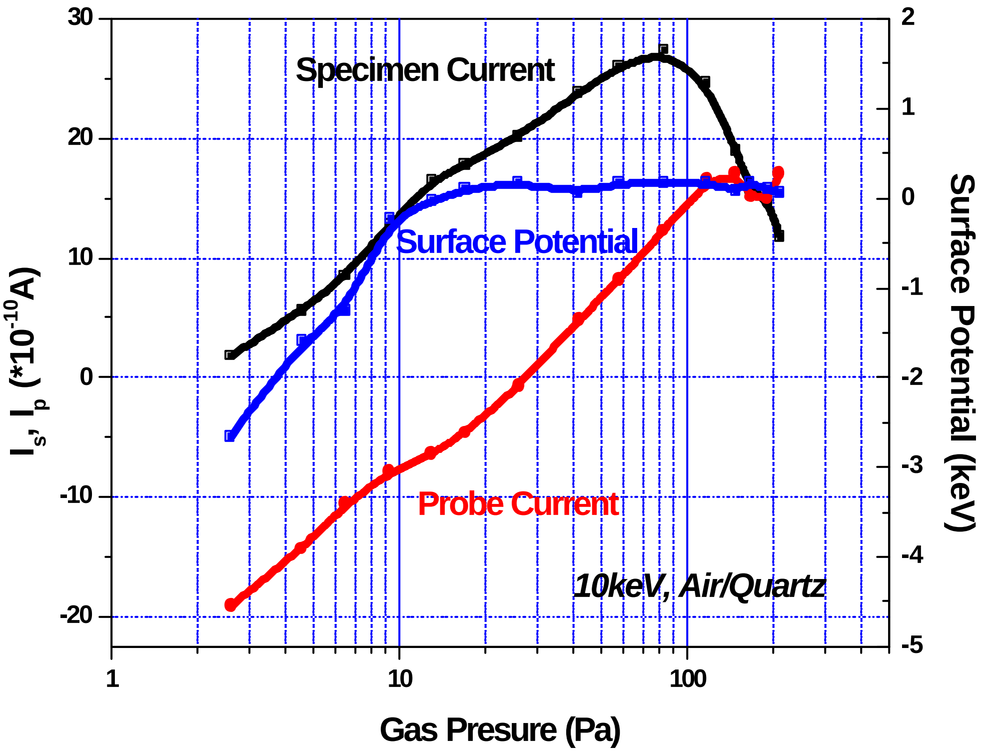

Figure 3.46 The relationship of specimen current, primary current, and surface potential as the function of air pressure on quartz by 10keV beam irradiation. The plate electrode of the SE detector is in SSE mode.

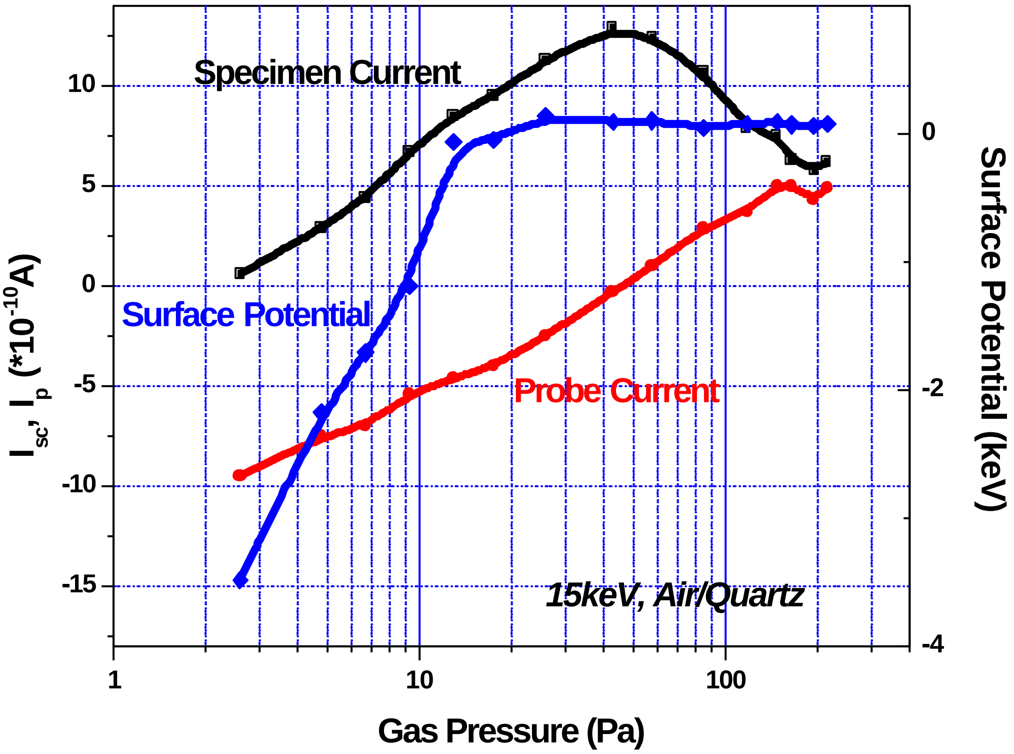

Figure 3.47 The relationship of specimen current, primary current, and surface potential as the function of air pressure on quartz by 15keV beam irradiation. The plate electrode of the SE detector is in SSE mode.

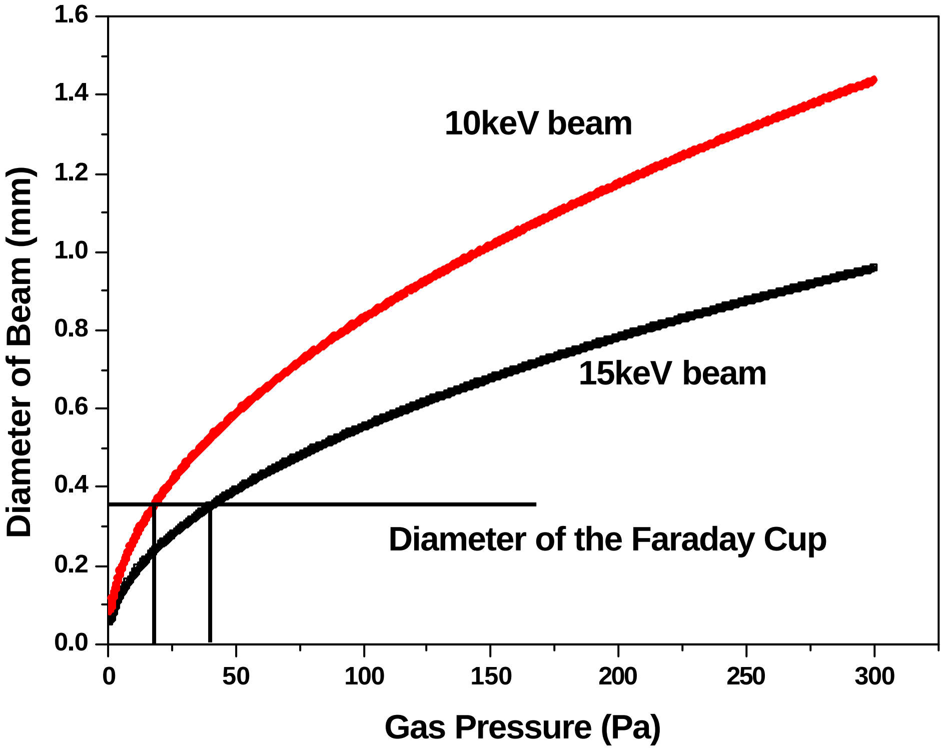

Figure 3.48 Test the effect of primary beam on gas ionization cascade. Curves show the variation of skirted beam diameter on gas pressure. The diameter of the Faraday cup used in experiment is 0.35mm. The critical gas pressures for skirting beam outside the Faraday's cup are 18Pa for 10keV beam, 41Pa for 15keV beam, respectively.

The results in table 3.2, 3.3, and 3.4 show that the charge reduction efficiency is always increased when beam energy increases. Also higher beam energy result in a more negative surface potential. These behaviors can be explained by the gas compensation model above: In the high vacuum condition the surface will be charged negatively. The incident high-energy electron beam results in a low probability of SE emission [Thiel et al. 1997]. Thus more electrons will accumulate on the surface causing a larger electric field. After gas is introduced into the chamber, primary, secondary, and backscattered electron will ionize the gas molecules, although the SE are the most important factor contributors. Meanwhile positive ions play an important role in compensating the surplus negative charge on the surface, resulting a surface potential fall. The electric field will help the gas avalanche process thus causing faster charge neutralization, and larger charge reduction efficiency. When the gas pressure is increased, the effect of positive ion-electron recombination becomes stronger, which offsets the gas ionization avalanche and weakens the charge neutralization process. At the same time, this recombination coefficient increases logarithmically with pressure [Danilatos 1988]. These two effects combine to produce a so-called dynamic equilibrium state or stabilization when gas pressure reaches some value.

The CRE decreases from helium to air, argon, and then to methane, and is determined by these factors: gas ionization energy; ionization cross-section; ion mobility, which is inversely proportional to the ion weight. Table 3.5 listed some parameters of gases used.

The gas ionization energy determines the ability to be ionized by electron and related with the ion-electron pair produced, which is critical to charging neutralization. Another important factor is the mean free path of gas molecule, which is directly related to gas pressure and may explain the logarithmic relationship of gas pressure and surface potential. Although the ionization energy of gas is critical in producing the ions, the ion mobility plays an important role in surface charge neutralization. As a result, the CRE value is inversely proportional to both the gas ionization energy and the ion weight. Thus the final CRE value depends on the tradeoff of these two factors. For example, despite the highest ionization energy of all three gases, helium has the highest charge reduction efficiency due to its lowest atomic mass.

Table 3.5 The ionization energy of different gases [von Engel 1955]

Gas Type	Water	Helium	Nitrogen	Oxygen	Argon	Methane
Weight (g/mol)	18	4	14	16	40	16
Ionization Potential (eV)	12.35	24.5	14.54	13.61	15.7	12.98

The CRE on sapphire is larger than that on mica for a given gas. Such difference can be attributed by the leakage resistance of the specimens, which can affect the Ohmic voltage drop produced by the incident beam current, and the secondary electron (SE) emission coefficient of mica is, as measured from the image in the SEM, higher than that of sapphire. SE emission efficiency will greatly affect the gas ionization process and change the surface charge state. Rough surfaces have a larger SE emission compared with smooth surfaces and thus are more efficient in ionizing the gas and neutralizing surface charging. Dielectric susceptibility is another factor, which is defined as the probability of storing a high density of charge in materials. Having a high susceptibility is the reason of the smallest of the Coulomb repulsion between pairs of charge.

In summary the experimental data generally supports the proposed mechanism (Figure 2.9). When a sample is irradiated by the electron beam then ions are generated by the emitted secondary electrons, the efficiency of this process depending on the secondary yield which is a function of the material and the incident beam energy. At very low gas pressures, the surface is at some negative potential relative to ground, therefore there is an electric field with the bias voltage directed away from the surface which accelerates the ions that are produced. This can lead to additional ionization production in a cascade process if the ions drift a large enough distance to acquire sufficient energy. The probability of an ion cascade forming therefore depends on the gas pressure, the field, and the distance that an ion can travel- which will typically be that between the sample surface and the lens, the gas path length (GPL). The positive ions drift back to the surface and partially compensate the surface charge. However, as the pressure raises a larger flux of ions reaches the sample surface providing sufficient ions to remove almost all surface charge. In this condition the field above the surface also disappears and so the ion cascade decays, as is seen by the abrupt change which occurs in the slope of the surface potential versus pressure plots when the potential is at, or close to, zero. The surface is then maintained at zero potential, or is made slightly positive by the incoming ion flux. At high beam energies the lower SE yield means that there are fewer initial ionization events and consequently a lower ion flux available for compensation. The surface can thus not be made either neutral or positive in potential. The exact conditions under which these situations occur will depend on the value of the GPL, here fixed at 12mm. For a shorter GPL higher pressures will be required. To a first approximation the pressure required to reach the 'knee' in the potential curve varies as 1/GPL. Since the scattering of the incident electron beam varies as $P^{1/2}GPL^{3/2}$ this indicates that the highest spatial resolution will be obtained by keeping the GPL as small as possible and then increasing the pressure just enough to achieve the desired minimum surface potential. Work is now in progress to extend these measurements to energies below 10keV, and to investigate how these results are different in a localized gas jet as compared with the enveloping gas atmosphere.

3.7 Conclusion

This experiment investigated the charging behavior of insulating materials irradiated by electron beam under the gas atmosphere. Some factors affecting the surface potential are also studied, including the gas type, gas pressure, sample material, beam energy, sample surface roughness, and bias voltage. The relationship curve of surface potential and gas pressure can be divided as two parts: charge neutralization and stable region. Some quantitative results as the charge reduction efficiency (CRE) are also presented. Increasing beam energy and bias voltage will raise the CRE. Surface roughness will evenly shift the surface potential to positive direction but do not change the CRE very much. All the results above can be explained by charge compensation mechanism. The process can be attributed as the competition process between: emitted secondary electron and incident primary electrons, gas ionization and electron-positive ion recombination.

CHAPTER IV GAS FLOW SIMULATION

4.1 *Introduction*

As discussed in the previous chapters, an effective method to alleviate charging phenomena on insulating and semiconducting materials is to surround the sample with a gaseous environment. The most usual way of doing this is to distribute gas uniformly throughout the specimen chamber, bleeding as through a leak valve and differential valve (or pressure limiting) aperture. The pressure-limiting aperture (PLA) is used to separate the high-pressure region from the high vacuum electron optical column, so the chamber can reach as high as 270 Pa (in a Hitachi S-3500) or 20 Torr (in an ESEM) while maintaining the gun at a pressure less than 10^{-6} Torr. Since the chamber is full of the gas, including the electron beam path, the incident beam will be skirted especially for low energy beam, high gas pressure, and long working distance. The skirt effect broadens the diameter of the beam spot, degrading the image resolution and reducing the image contrast. An alternative approach, which avoids these problems, is to use a localized gas jet directed to the point where the beam meets the sample surface. At this time the gas layer above the sample surface also can be ionized by e-beam irradiation so as to neutralize the charging with less beam broadening. Studies of both deposition and etching show that the size and shape of the plume from the gas nozzle has an effect on the process, as shown in figure 4.1. It can be expected that the size and shape of the gas plume will have an effect on the charge reduction just as it does on the etching and deposition that occur in a precursor gas jet.

To understand and optimize this effect, it is necessary to know where the gas goes, its pressure and temperature distribution after it leaves the nozzle [Neilde et al. 2002]. In this pressure range (~10^{-2} Torr) classical gas flow models are invalid because the gas is too dilute. Therefore a molecular dynamics simulation has been developed, based on the work of G. A. Bird [Bird 1976] in the 1970s, to be able to simulate the gas flow close to the surface. Some work has

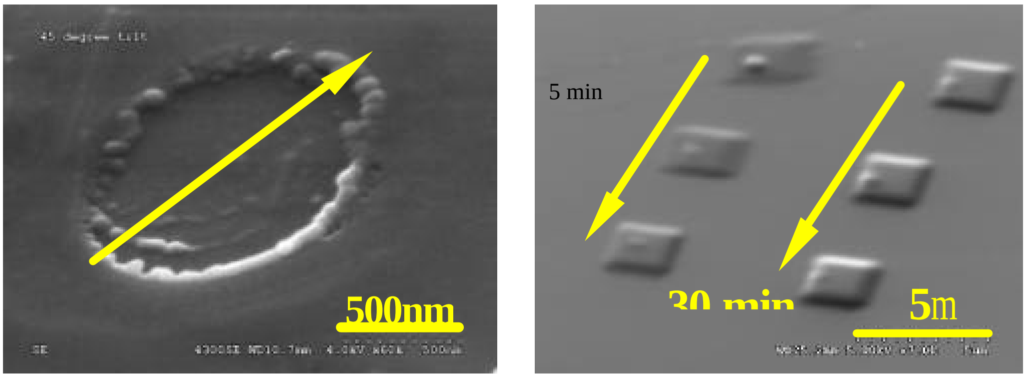

Figure 4.1 E-beam induced etching and deposition from a localized gas jet of precursor gas. The arrows show the gas flow direction.

also been done to investigate the properties of the gas by the direct-simulated Monte Carlo (DSMC) method of Bird from a commercial package [Danilatos 1991][Bird 1994].

Figure 4.2 schematically shows the cross-section of the gas jet and the incident electron beam [Wurster 1986]. Combining the simulated gas distribution with a model of the electron beam scattering gives a comprehensive model of the gas interaction and ionization by electron beam, and hence ultimately predicts the form of subsequent deposition or etching steps.

4.2 Procedure

"Monte Carlo" simulation first evolved as a mathematical process in the 18th century and it has many applications in statistics and physics related area, such as radioactive decay and transmission of cosmic rays through barriers [Joy 1995]. The first Monte Carlo simulation of gas flow was introduced by William Anderson [Kelvin 1901]. Since then other works in this field had been done by different groups and consequently the framework of Monte Carlo simulations

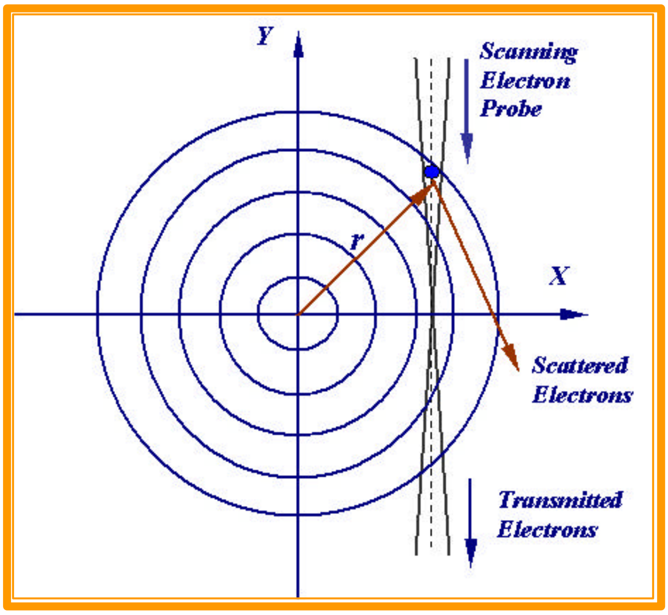

Figure 4.2 Coordinate schemes for gas modeling as the cross-section of the gas jet

had been established. The use of random number to choose several various probabilities of action is the distinguishing feature of a Monte Carlo procedure, and the essentially probabilistic nature of a gas flow at the molecular regime makes it a good fit for a simulation approach. The technique was used by Danilatos to study the gas flow etc around the PLA [Danilatos 1991].

The molecular model of the gas flow is different from the macroscopic or continuum model based on the Knudsen number K_n, which is a distinct dimensionless parameter defined as

$$K_n = l / l \tag{4.1}$$

here l is the mean free path (MFP) of the molecules and l is the characteristic flow dimension which is typically chosen as the length of the pipe. If K>>1 then the flow is defined as being molecular. The MFP of air at a pressure of 1Pa is about 6mm, which is larger than that of pipe diameter (0.5mm), thus the gas flow is defined as molecular regime without interactions between molecules. At any Knudsen number a rarefied gas flow can be calculated on the basis of the distribution function $f(t,r,v)$, which provides access to many macroscopic characteristics such as [Cercignani 1988] the particle number density distribution

$$n(t,r) = \int f(t,r,v)dv \tag{4.2}$$

the pressure distribution

$$P(t,r) = \frac{m}{3}\int V^2 f(t,r,v)dv \tag{4.3}$$

the temperature distribution

$$T(t,r) = \frac{m}{3nk_B}\int V^2 f(t,r,v)dv \tag{4.4}$$

where t is the time, **v** is the molecular velocity, m is the mass of the particle, r is the position vector, k_B is the Boltzmann constant, and V is the peculiar velocity.

The distribution function $f(t,r,v)$ can be obtained from the Boltzmann equation

$$\frac{\partial f}{\partial t} + v\frac{\partial f}{\partial r} = \int w(v, v_*; v', v'_*)(f' f'_* - ff_*)dv' dv_* dv'_* \tag{4.5}$$

here, the suffixes to *f* correspond to those of their arguments **v**: $f' = f(t,r,v')$, $f_* = f(t,r,v_*)$. The quantity $w(v, v_*; v', v'_*)$ is the probability density that two molecules having the velocities **v'** and **v'**$_*$ will have the velocities **v** and **v**$_*$, respectively, after a binary collision between them.

This model is based on the principle of treating all gas molecules as hard spheres. The boundary conditions are as follows: no inter-molecular collisions; only consider the collision between molecule and tube wall; no surface reaction and adsorption; collisions obey the ideal reflection law and momentum conservation; the passage of gas molecules through the tube is a discrete process; and the gas has a stationary initial state. The distribution of gas molecules is computed by a Visual Basic program, given in Appendix A of this thesis. The dilute gas flow is a kind of probabilistic process, which requires the generation of representative values of variables that are distributed in a prescribed manner to model it. In this simulation, random numbers are used to determine the initial position of molecule, and the directional cosine of next movement. A random number is defined as one which is uniformly distributed between 0 and 1. Random number can be supplied as a standard function on a computer or obtained from standard table. The arrangement and cross-section of the tube are shown in figure 4.3.

Assume the coordinate of the initial position at the X-Y plane is (X_0 Y_0), the distance from the origin O to this point is R, and the radius of the circle is 1. RND is the random number. The probability of a molecule situating inside a smaller circle with radius RM determined by calling a random number which functions as the probability since both the random number and the probability range from 0 to 1 and are uniformly distributed. Thus

$$\begin{aligned} RND &= \frac{\pi RM^2}{\pi 1^2} = RM^2 \\ RM &= \sqrt{RND} \end{aligned} \qquad 4.6$$

After the initial coordinates of molecule on cross-section 1 are determined, the molecules will be followed in sequential steps along its trajectory. Since the motion can be in any sense, the direction cosine of the first step is determined by a random number. This step is then extended until it strikes the tube wall, at which point the molecule rebounds. Figure 4.4 shows the projection of the rebounded point (can be A or B, here we consider A only) on the cross-section 1. Clearly point A is the intersection of line AB and circle O. Assume the initial point C and the intersection point A have the coordinates (X_0, Y_0) and (X, Y) respectively, the angle of circle is used to represent the coordinates.

The coordinates of the starting point are

$$X_0 = RM \times \cos\theta \qquad 4.7$$

$$Y_0 = RM \times \sin\theta \qquad 4.8$$

$X = \cos\phi$

$Y = \sin\phi$

The equation of line AB is

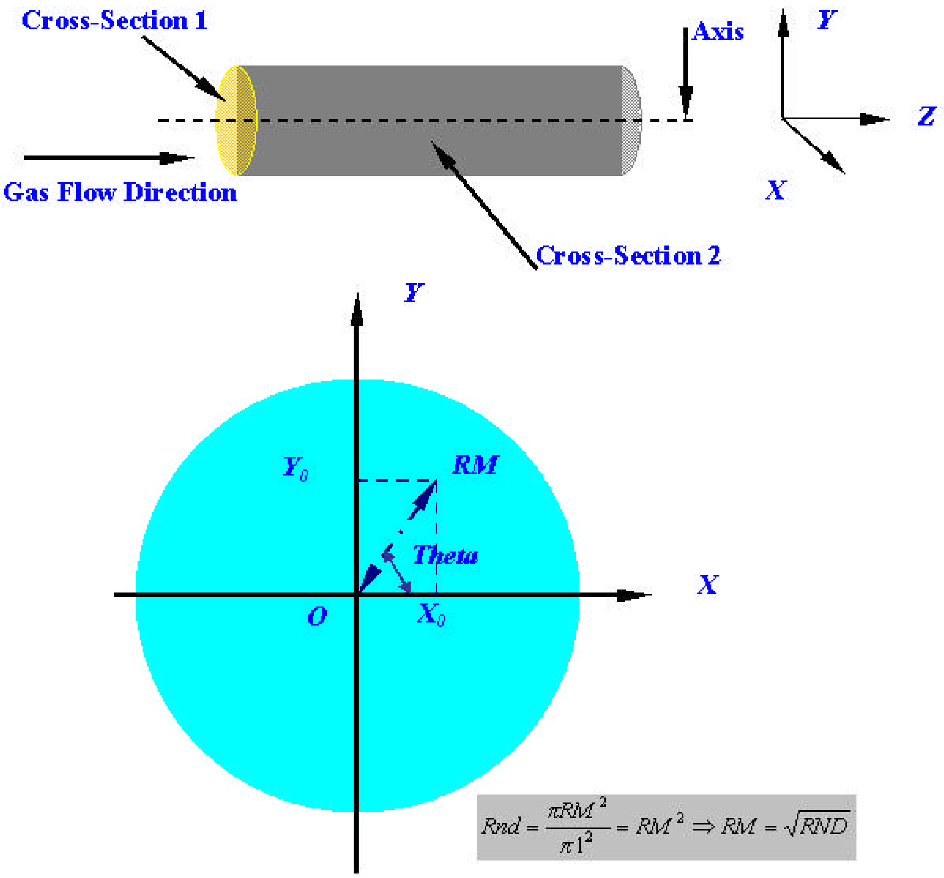

Figure 4.3 Schematically show the arrangement and the cross-section of the pipe

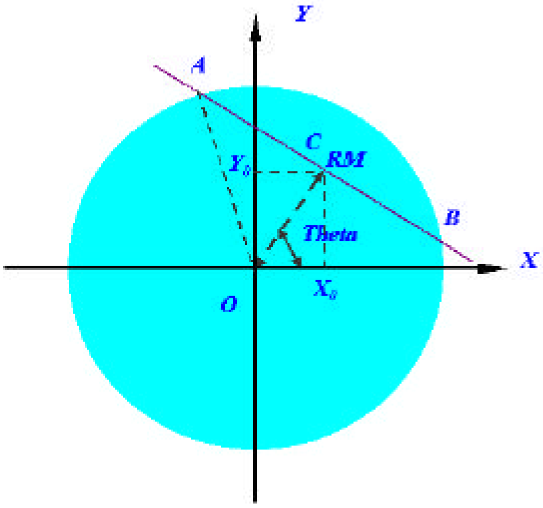

Figure 4.4 The projection of the rebound point on the cross-section 1

$$Y - Y_0 = k(X - X_0)$$

here k is the slope of the line AB and equals to tan(∠ACY$_0$). Assume the directional cosines at three directions are cosine (x), cosine (y), and cosine (z).

$$\tan \angle ACY_0 = \frac{\cos z}{\cos x}$$

The equation of line AB thus transforms into

$$Y - Y_0 = \tan \angle ACY_0 \times (X - X_0)\,.$$

The equation of the circle is

$$X^2 + Y^2 = 1$$

Combining these two equations, the coordinate of the next rebounded point on the tube wall can be determined.

In the gas flow direction (Z axis), the direction cosines can also be represented by the random number, and the rebounding point on the pipe wall also be calculated. Figure 4.5 shows the pipe structure in three dimensions and the direction cosines are

$$\cos q_1 = \sqrt{1 - RND} * \cos(2p * RND) \qquad 4.9$$

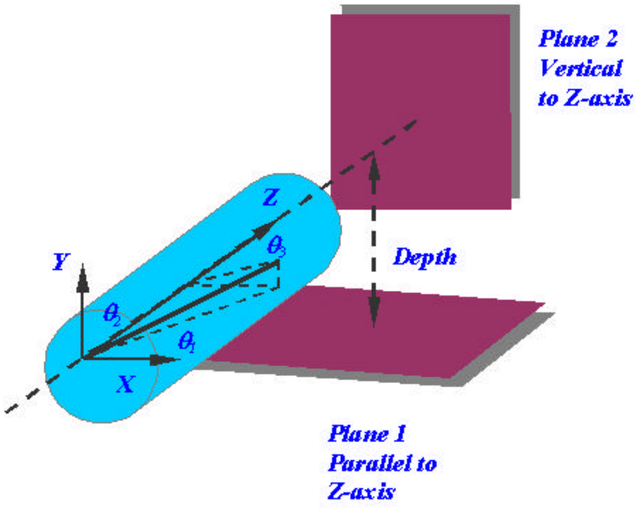

Figure 4.5 Schematically show the direction cosines and the 3D arrangement

$$\cos\theta_2 = \sqrt{1 - RND} * \sin\left(2\pi * RND\right) \tag{4.10}$$

$$\cos\theta_3 = \sqrt{RND} \tag{4.11}$$

4.3 Results and Discussion

After the procedures are translated into the Visual Basic code, the distribution of the gas flow out of the pipe is obtained. The properties of the distribution are affected by many parameters such as the distance, the angle of pipe, and the number of the particles simulated. The plume aspect ratio is defined as the ratio of the plume length to the half width of the plume in the radius direction. By adjusting these parameters, the desired gas flow distribution can be achieved.

4.3.1 Distribution on Plane 1

Figure 4.6 shows the effect of the distance from the pipe axis to the plane 1, which is parallel to Z-axis, on the distribution of the particle density on plane 1. The plume out from the gas nozzle changes shape, which is more diffuse and less particle density variation with the increased distance. Such plume expansion mainly occurs at the radius direction and keeps constant at the Z-axis, or the plume aspect ratio is decreased. Meanwhile the distribution of the molecules outside the pipe is cylindrical symmetry, so the distribution in whole space can be reconstructed. Pressure P is defined as the normal momentum of gas molecule transferred within collision on a unit area per unit time t, or the product of the molecular density and the mean value of the square of the thermal velocity [Bird 1994].

$$P = \frac{1}{3} r \overline{c'^2} \qquad 4.12$$

$$P = \frac{mv}{tA} \qquad 4.13$$

where r_m is molecular density, $\overline{c'^2}$ is the mean value of the square of the thermal velocity components in any direction, m is the mass of molecule, **v** is velocity vector perpendicular to the interested plane.

On the other hand, pressure can also be deduced by the ideal gas equation

$$P = rRT = nkT \qquad 4.14$$

here k_B is the Boltzmann constant which is related to the universal gas constant R by

$$k = \frac{R}{N_A} \qquad 4.15$$

and N_A is the Avogadro’s number.

An important result from the above comparison shows that the ideal gas equation can be applied to a dilute gas even in a non-equilibrium condition, which connects temperature and

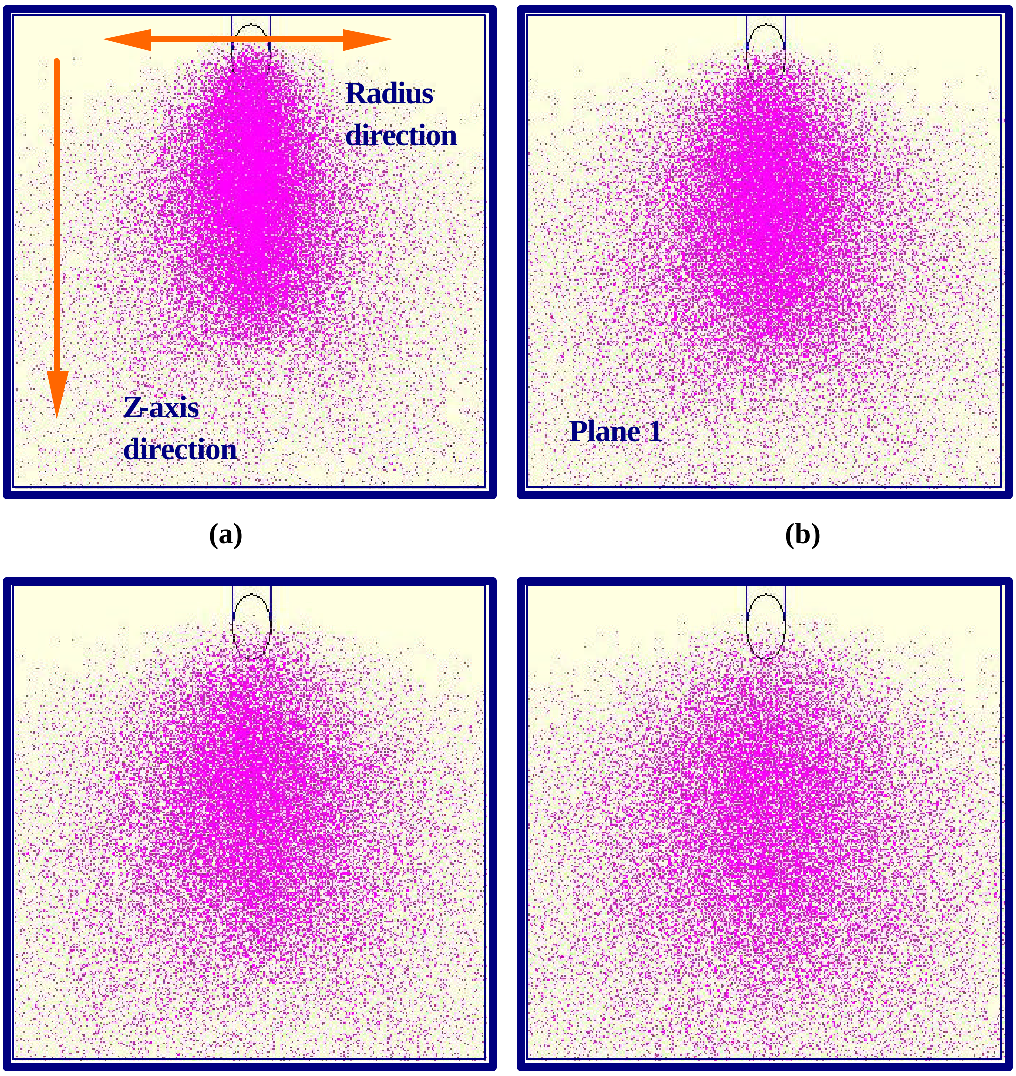

(a) **(b)**

(c) **(d)**

Figure 4.6 The molecules distribution on plane 1 varies with the depth. The distance between the pipe axis and plane 1 increases from 1, 2, 3, to 4 times of the pipe radius as the sequence of (a)(b)(c)(d). Simulated molecule number is 100000. The end cross-section plane has 30^{o} degree to the Z-direction. The ratio of length to radius is 10.

pressure. The overall temperature distribution is defined as the weighted mean of the translational and internal temperature

$$T_{ov} = (3T_{tr} + zT_{\text{int}})/(3+z) \tag{4.16}$$

The translational kinetic temperature T_{tr} is defined by

$$\frac{3}{2}kT_{tr} = \frac{1}{2}m\overline{c'^2} = \frac{1}{2}m(\overline{u'^2} + \overline{v'^2} + \overline{w'^2}) \tag{4.17}$$

The internal temperature T_{int} is defined as

$$\frac{1}{2}zRT_{\text{int}} = e_{\text{int}} \tag{4.18}$$

Here, x is the number of internal degrees of freedom and e_{int} is the specific energy associated with the internal modes. Thus the temperature distribution can be obtained from the known pressure distribution.

4.3.2 Effect of the Computational Approximations

An important notion used in this simulation procedure is the computational approximation, which defined as the ratio of the number of simulated molecules to the number of real molecules in order to avoid the lengthy simulation time and make the result tidy. The number of molecules is about 10^{17} for 0.1Pa gas inside the 5 liters SEM chamber at room temperature by the ideal gas law. It is unrealistic to simulate such a huge number of molecules. For a given gas pressure, the variation of the computational approximation number helps to refine the macroscopic distribution of particle density and pressure. The pressure distribution is derived from the particle density distribution divided by the chosen area. Figure 4.7 shows the molecules distribution on the plane 2 (vertical to the pipe axis) and figure 4.8 describes variation of the pressure distribution on the plane 2 from the center of the axis to the edge. The number of the particles used in simulation affects the deviation of the final results. Figure 4.7 clearly indicates that decreasing the computational approximation number (the real particle from 5000, 50000,

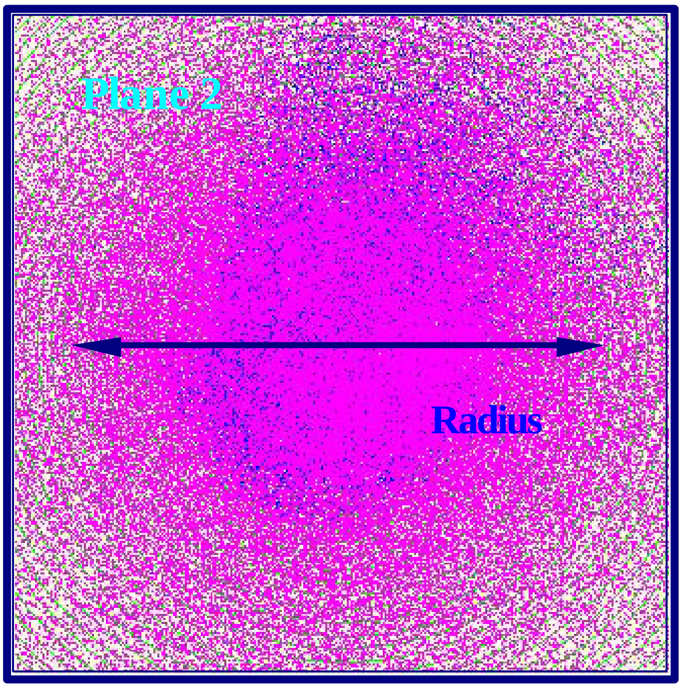

Figure 4.7 The molecules distribution on the plane 2 from the center of the axis to the edge. The angle between the end cross-section plane and the Z-direction is 30^o degree. The distance from the end of the pipe to plane 2 is 10 times of the pipe radius. The ratio of length to radius is 10. The number of molecules simulated was 500000.

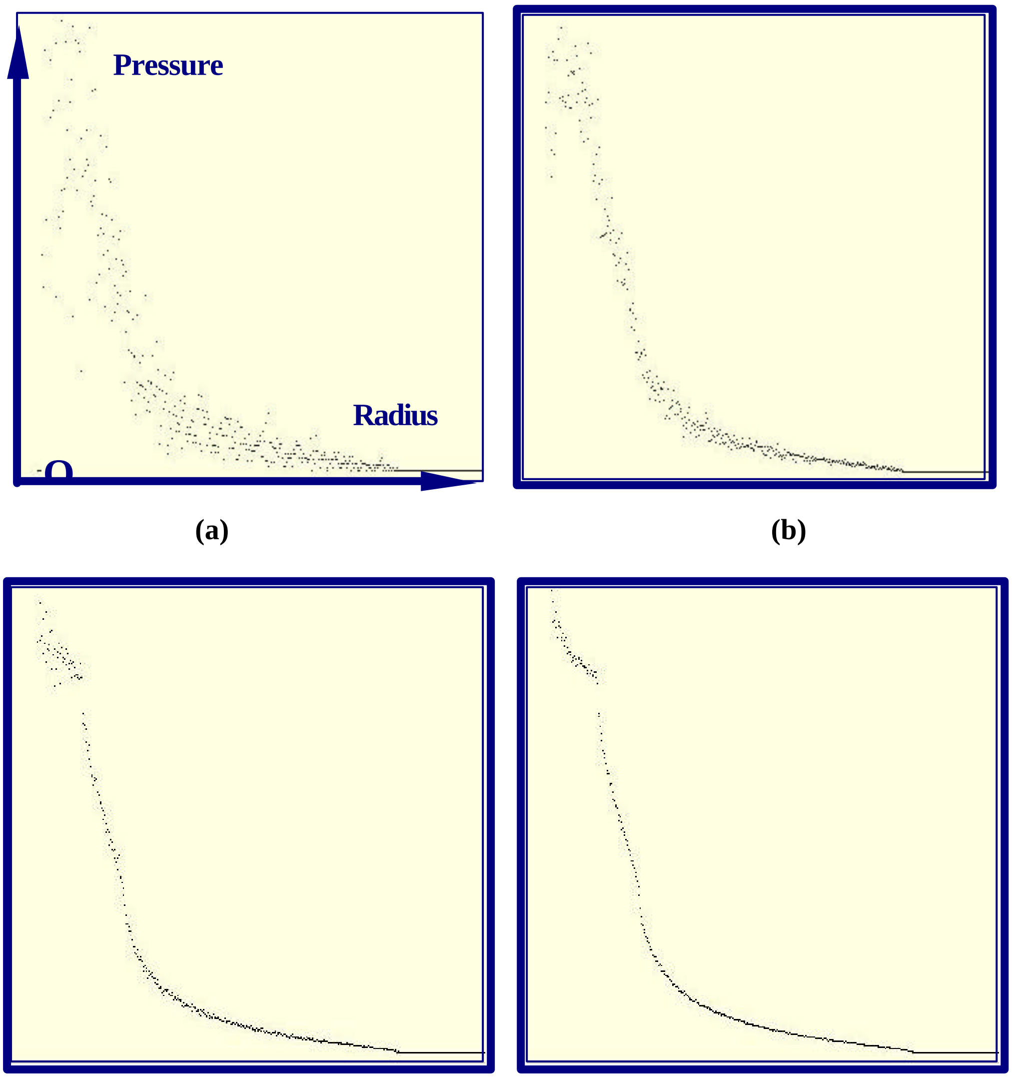

(a) (b)

(c) (d)

Figure 4.8 The pressure distribution on plane 2 from the center of the axis to the edge. The real particle numbers increase from 5000, 50000, 500000, to 5000000. The end cross-section plane has 30^o degree to the Z-direction. The ratio of length to radius is 10. The distance from the end of the pipe to plane 2 is 10 times of the pipe radius.

500000, then 5000000) helps to refine the distribution curve of the pressure on plane 2. In order to achieve a statistically useful result many tens of thousands of molecules must be tracked.

4.3.3 Effect of the Pipe Shape

The gas flow properties are also greatly affected by the shape of the pipe, which includes the pipe aspect ratio (length to radius) and the angle between the cross-section plane and the pipe length direction. Drawing in figure 4.9 plots the variation of pressure distribution by changing the pipe aspect ratio and figure 4.10 shows how the angle of the cross-section plane affects the final molecule distribution.

Keeping other parameters constant, the shape of the gas plume on the plane 1 varies by changing the pipe aspect ratio, which can be achieved by altering the pipe length or the radius of the pipe, respectively. The gas plume is more concentrated near the region of the pipe outlet when the aspect ratio decreased. For a higher pipe aspect ratio, the gas plume is fuzzy and elongates along the direction of gas flow, corresponding to a larger plume aspect ratio. It's suggestive to select the pipe with a small aspect ratio in order to gain a more localized gas distribution, but a large aspect ratio of pipe is more favorable if a wide spread gas environment is required.

Another important parameter to affect the molecule distribution is the angle between the end cross-section plane and the Z-axis of the pipe. The gas plume shrinks at both the Z-axis and the radius directions when the angle increases from 30° to 90°.

4.3.4 Verification

The data obtained by this procedure give results that are both intuitively reasonable and physically sensible. Direct experimental verification is more difficult because specialized

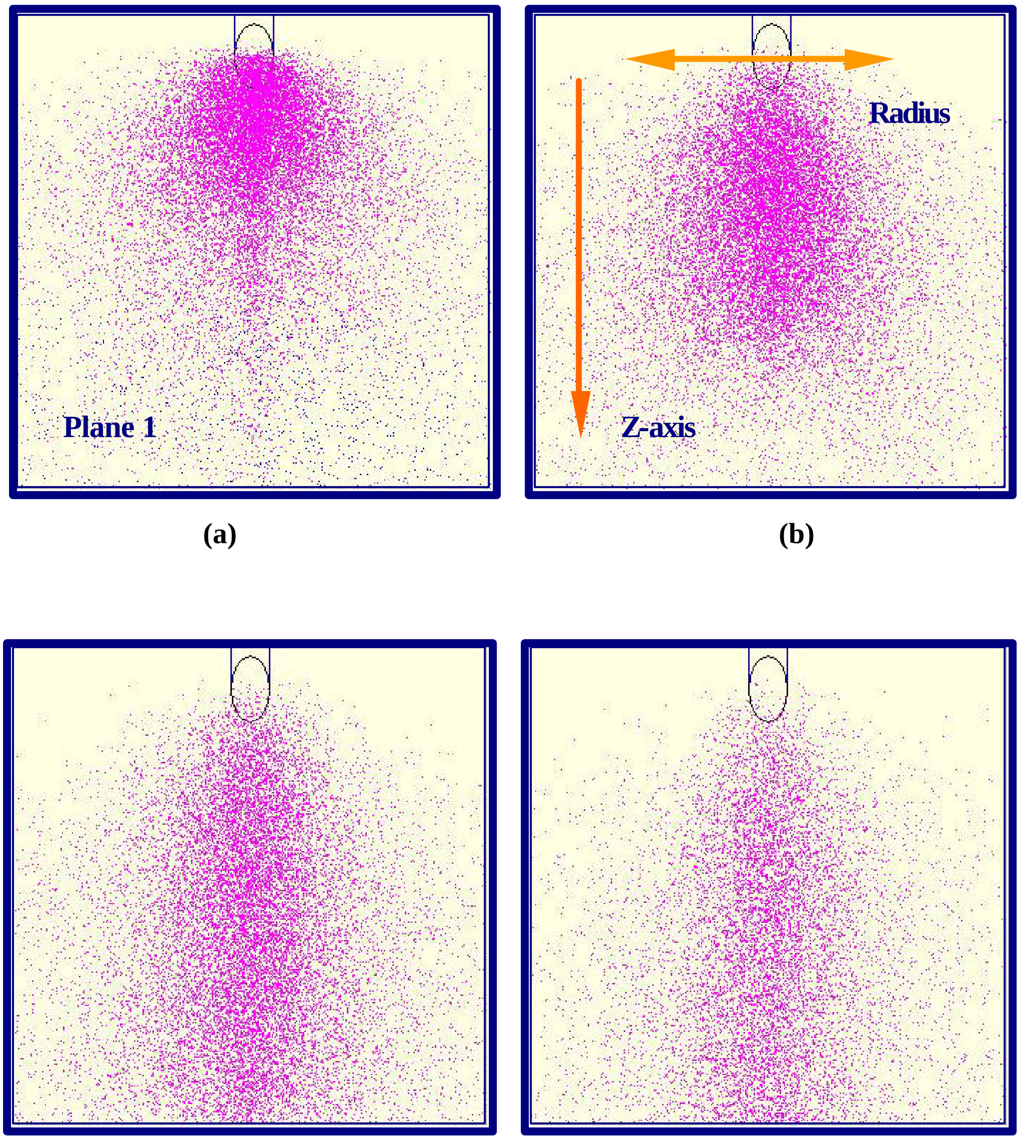

(a) (b)

(c) (d)

Figure 4.9 The molecules distribution on plane 1 varies with the pipe aspect ratio. The distance between the pipe axis and plane 1 is two times of the pipe radius. The number of molecules simulated was 50000. The end cross-section plane has 30^o degree to the Z-direction. The ratio of length to radius in (a), (b), (c), and (d) varies as the sequence of 4, 10, 20, and 40 times of the pipe radius.

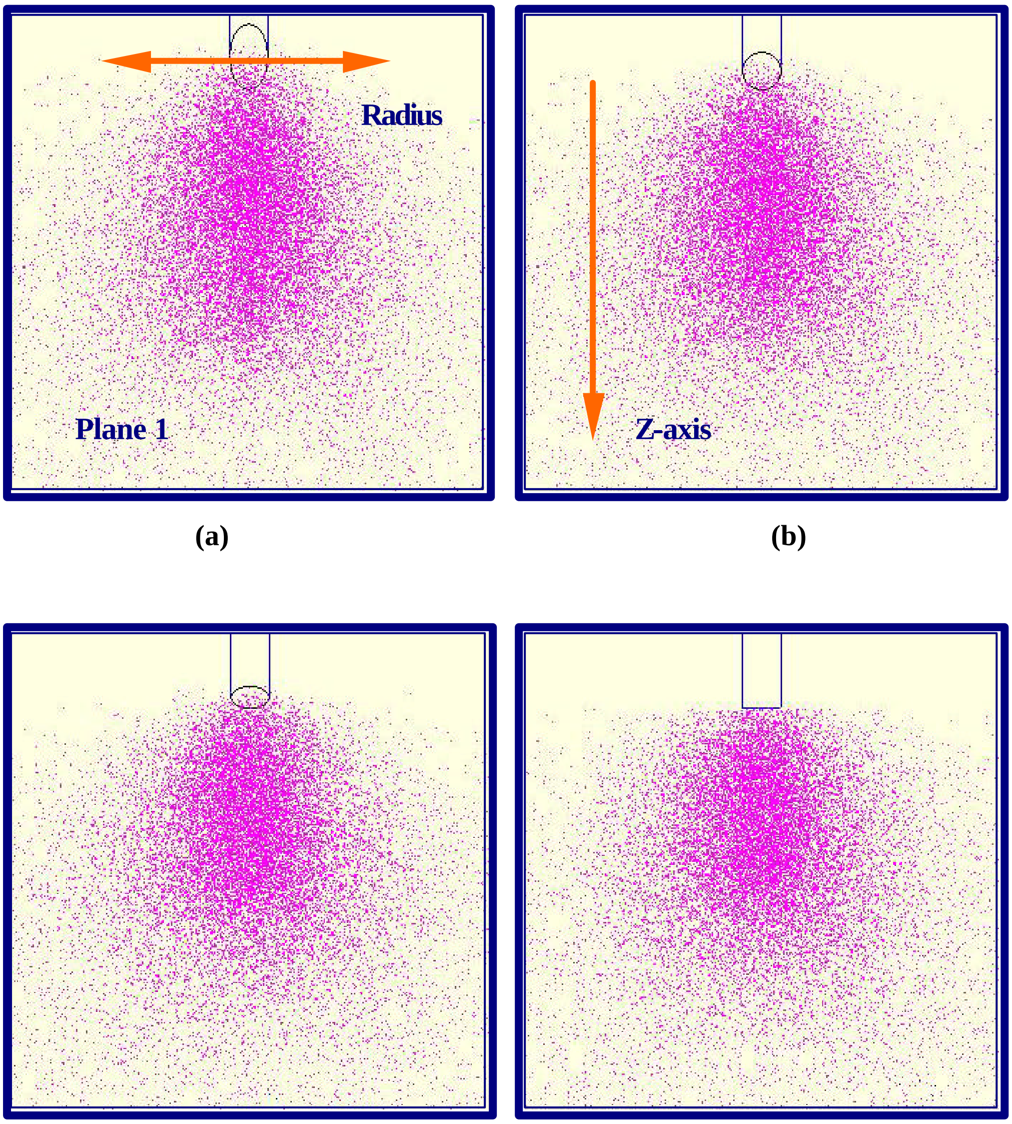

(a) (b)

(c) (d)

Figure 4.10 The molecules distribution on plane 1 varies with the ending-angle of pipe. The distance between the pipe axis and plane 1 is twice of the pipe radius. The number of molecules simulated was 50000. The ratio of length to radius is 10 times of the pipe radius. The angle between the end cross-section plane and the Z-direction increased from 30^{o}, 45^{o}, 60^{o}, and 90^{o} as the sequence of (a), (b), (c), and (d).

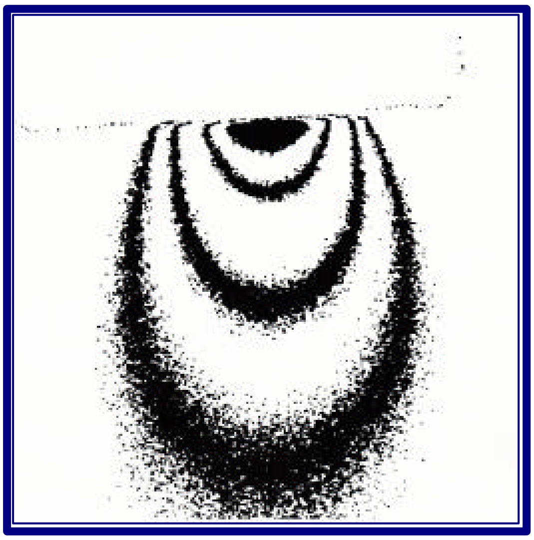

Figure 4.11 Iso-density curves obtained by discrimination the gas jet image of TEM at distinct grey level values intervals by an image processing system [Wurster 1986].

“sniffers” to sense localized pressures are required. However the form of these solutions can be compared with the experimental data obtained by optical or thermal methods from gas jets, wind tunnels and other systems [Wurster 1986]. For example, figure 4.11 shows the iso-density curves obtained from a brightfield gas jet image recorded in a TEM at distinct grey level values intervals by an image processing system.

Because the experimental contours represent a projection through the entire depth of the plume outside the gas jet, rather than the individual slices of the simulation model, corrections have to be made to allow for a valid comparison. The quality of agreement has been found to be good within the range of conditions that are of interest.

The logical method to simulate the complex gas low that involves multiple surface reactions is the test particle method. The main disadvantage of this method is the initial estimate requirement for the distribution function over the whole flowfield. The alternative to the test particle method is to introduce a time variable and to follow the trajectories of a very large number of simulated molecules simultaneously, called the direct simulation Monte Carlo (DSMC) method. The essential assumption of DSMC is to separate the molecular motion and the intermolecular collisions within a small time interval. The principle limitation of this method is that it only can be applied to dilute gas flows but the computational efficiency of the DSMC method is far higher than that of the molecular dynamics (MD) method. Here the commercial Visual DSMC program for two-dimensional and axially symmetric flows by Bird is also being evaluated, which is shown in figure 4.12. The velocity components and position coordinates of all of the molecules are stored in the computer and are modified with time as the molecules are concurrently followed through representative collisions and boundary interactions in simulated physical space. This model allows chemical reactions at the walls to be included but computation times are long and the user interface is difficult.

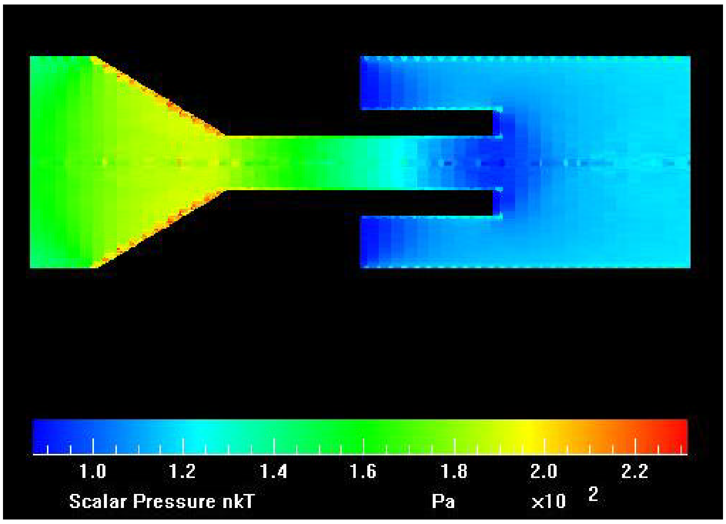

Figure 4.12 Gas flow distribution from Direct Simulation Monte Carlo (DSMC) method

CHAPTER V CHARGE VISUALIZATION

5.1 Introduction

In the previous chapters it has been demonstrated how charging can be quantified by a variety of analytical techniques. But other questions about the nature of charging such as its spatial extent require some methods for visualizing the effect. We therefore describe here a simple technique which provides a rapid way of visualizing charging phenomena and so examining its spatial characteristics.

Soon after Ben Franklin first demonstrated the electrical nature of lightning, Lichtenberg in Germany noted that lightning strikes on the ground produced characteristic patterns in the dust, an example of which shown in figure 5.1 [Lichtenberg 1777][Merrill 1939]. His drawings of these events helped to provide the basic understanding of lightning formation and his methods were used until the 1930's to study high-energy electrical discharges [Lee et al. 1927]. The basic principles involved in the formation of these electrostatic figures were later developed into modern xerography.

The Lichtenberg experiment can now be carried out on a much smaller scale by using ultra-fine particles – such as toner powder. The object to be studied (quartz or sapphire) is coated with a 'monolayer' of commercial toner powder of the type used in office copiers. The toner powder is usually applied prior to irradiation, but can also be applied to a specimen recently removed from the microscope. The toner particles are small (micron size), highly electrostatic and lightweight. They readily interact with a field but do not interact with each other and originally have a static positive charge [http://www.howstuffworks.com]. Under the e-beam irradiation, they thus will sense the presence of the electric field associated with bulk and surface charging and move in the field before coming to rest on the surface at point where the field is a

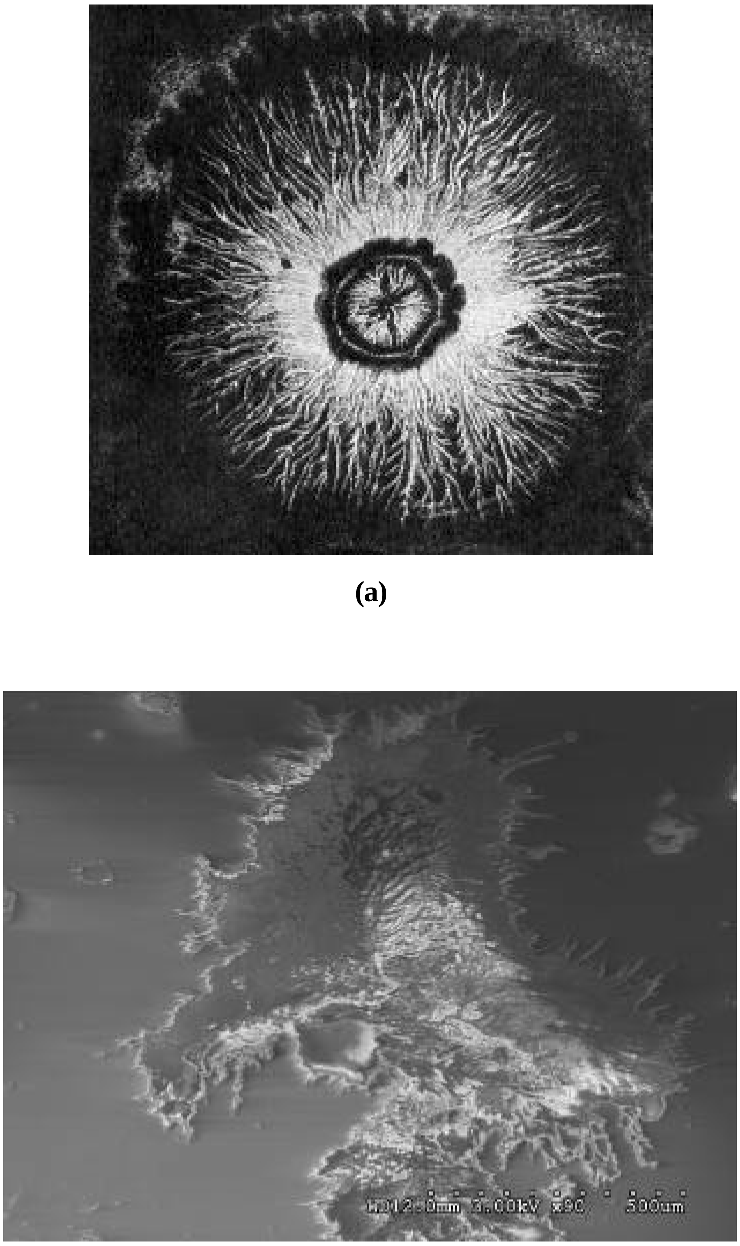

(a)

(b)

Figure 5.1 Lichtenberg's drawing made in sulphur dust by means of a charged electrode in 1777 (a) Contamination image on quartz surface by 3keV beam irradiation. The magnification is 90× and at high vacuum condition (b) minimum. Once the toner powder has settled it remains firmly attracted to the surface and can be imaged in the SEM, or by placing it in a flat bed optical scanner connected to a computer.

The regular secondary electron image is based on the collection of the SE signals which means the brightness of the SE image is proportional to the SE yield. If the insulator surface is charged up, its SE image is bright in a negatively charged region due to the higher SE yield, while it is in a dark at positively charged area since the SE emission is depressed. The charged SE image somehow qualitatively illustrates the surface potential distribution. Figure 5.2 shows the comparison of charged surface with and without toner powder, respectively.

The contrast of the bright and dark regions in figure 5.2 (b) and (d) show the surface electric field distribution, which corresponds the formation of toner powder pattern in figure 5.2 (a) and (c). Thus the relationship between the surface potential distribution and the toner powder pattern is created. Figure 5.2 (b) and (d) are taken at magnification of 150× and correspond to the area of rectangle with the black edge in figure 5.2 (a) and (c), which are at magnification of 40×. In addition the inner white circles of figure 5.2 (b) and (d) are demonstrated as the toner powder clusters inside the black rectangles because the negative charge keeps toner powder in position. The bright area outside the black rectangle is the result of the attractive force on the positively charged toner by negative electric field. Another feature in figure 5.2 between 3Pa and 5Pa images is the relative shape of both SE images and the toner powder pattern because the previous chapters indicate that lower gas pressure with other parameters constant has higher surface potential and stronger field intensity. As charging is a dynamic process and charges will diffuse with time elapsing, thus figures were taken after surface reaches the stable state. The change in the apparent rectangle size will be discussed in detail later.

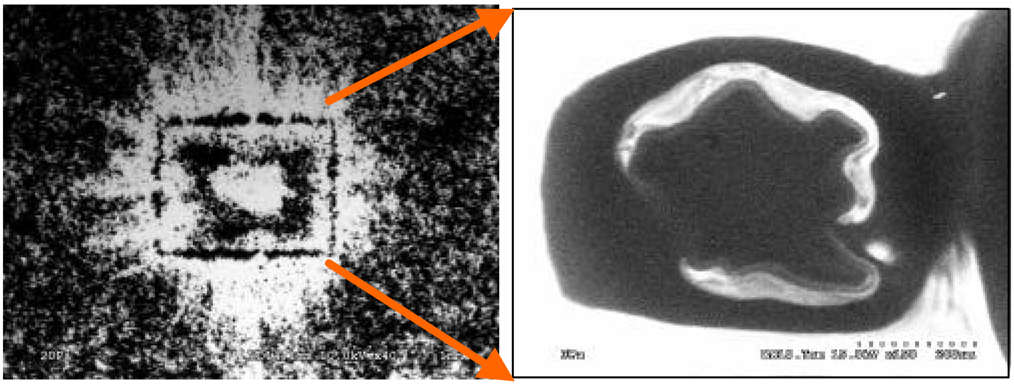

(a) (b)

3Pa

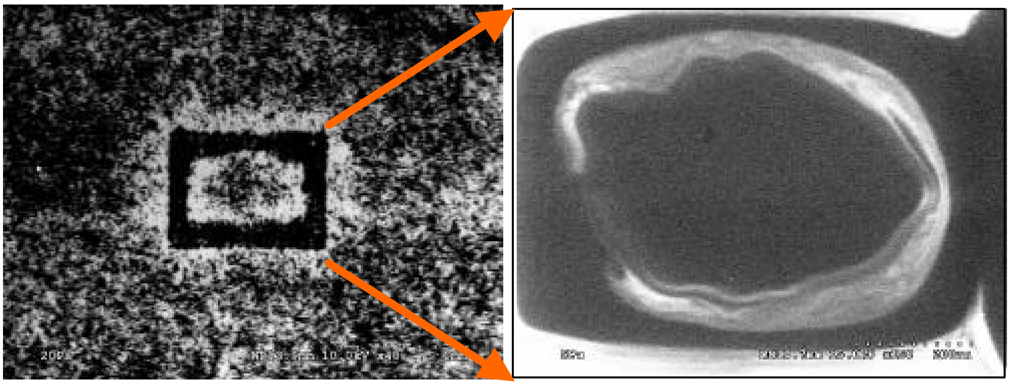

(c) (d)

5Pa

Figure 5.2 Comparison of the surface charge pattern with and without toner powder on quartz surface in 3Pa and 5Pa air environment, respectively. Right figure (b) (d) (150×) are the amplified part of left figure (a) (c) (40×). Toner powder clusters and dark areas are positively charged; powder-free areas and bright area are negatively charged.

5.2 Experimental Procedure

The samples were carefully cleaned by acetone in an American Brand ultra-sonic cleaner. Then a California Stainless MFG oven was used to bake the samples so as to evaporate the residual acetone from off the surface. There are two ways to deposit the toner powder on the insulator surface either before, or after, electron beam irradiation of the sample. Here the pre-irradiation approach was used for the operational convenience. The toner particles are uniformly applied on the surface of quartz blocks with a size L60mm×W20mm×H2mm, then both of them were irradiated by the electron beam on a Hitachi S-3500 SEM under variable pressure mode, with a setting of 150× magnification, 30 seconds duration exposure time, a working distance of 12mm, and a rapid (TV1) scanning rate. After that, the patterns are observed with a magnification of 40×, 15Pa gas pressure, and 10keV beam energy, under which condition the surface is free of charging. Meanwhile, the relationships of surface charging with different experimental parameters were recorded by measuring the Duane-Hunt (D-H) cut-off of the x-ray spectrum [Tang et al. 2003][Duane et al. 1915].

5.2.1 Magnification Effect – Varying the Dose Density

Figure 5.3 shows the Lichtenberg images, which demonstrate the effect of the magnification on the distribution of toner powder, or surface electric field, and the relationship curve of magnification with surface potential. The magnification varies as 150×, 300×, 500×, and 1000×. Magnification will affect the impinging rate of the electron dose density, which equals to the electron beam density divided by the irradiation area. The irradiation area is directly proportional to the magnification. Thus higher magnification corresponds higher dose density so that the electric field created by surplus surface charge is intensified.

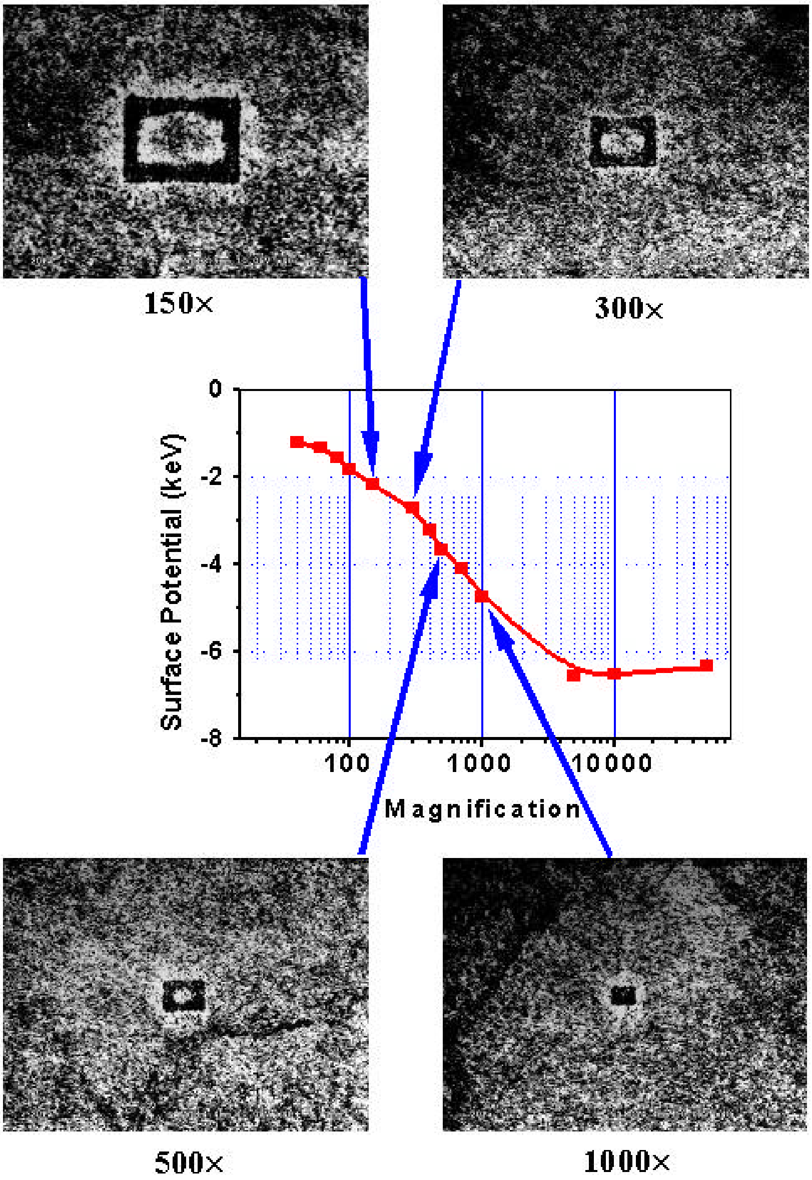

Figure 5.3 Variation of the toner powder patterns with magnification. Quartz substrate was irradiated by 15keV electron beam in 5Pa air. Magnification varies as 150×, 300×, 500×, and 1000×, scanning rate TV1 16ms/frame, duration time 30seconds. The resulting patterns were observed by a 10keV electron beam, magnification 40×, and 15Pa air. Center is the relationship of surface potential, magnification (dose density) in 5Pa air environment on quartz surface. Incident beam energy is 15keV, working distance 12mm.

The black rectangle in the Lichtenberg image is defined by how far the electric field can expand, which results from the surface charging by e-beam irradiation. As the electric field increases, the charge will not stop diffusing until the equilibrium of the whole system is reached. The stronger the electric field, the farther the charge diffusion. The brighter area surrounding the black rectangle is due to the attraction effect of the electric field on toner. The distance of this area is an important parameter to describe the intensity of the electric field. The size of the black rectangle and the distance of the brighter region surrounding the rectangle in figure 5.3 are obtained in line profile by Scion Image [http://www.scioncorp.com]. These dimensions are described in figure 5.4. The image size with magnification 40× is 1280×960 pixels thus the image size of magnification M× can be deduced as

$$\begin{aligned} Width &= 1280 \times 40 / M \\ Height &= 960 \times 40 / M \end{aligned} \qquad 5.1$$

The theoretical and measured values of the rectangle size are listed in table 5.1 and the measured distance of the brighter surrounding area and the relative ratio to the rectangle size are listed in table 5.2. Data show that the relative size of the black rectangle to the irradiation area and the distance ratio of the bright surrounding area to the rectangle size, which are both used to describe the intensity of the electric field, increase with the higher magnification. That means increasing magnification, which equals to increase the electron dose density, makes a lightly charging sample begin to charge more severely. These results are well matched with the curve of the surface potential as a function of magnification, which is obtained from the Duane-Hunt limit of the x-ray spectrum under the same experimental condition as that of toner powder pattern. In addition, the value of measured rectangle size is always larger than that of calculated no matter what magnification used. This is because the negative surface potential helps to attract toner powder to form the black edge of the rectangle. The higher the negative surface potential is, the wider the edge and thus the higher the ratios of the width and height to the calculated value.

Another important result from the measurement is that the rectangular feature of the brighter surrounding area at the lower magnification tends to diminish and changes to the circular

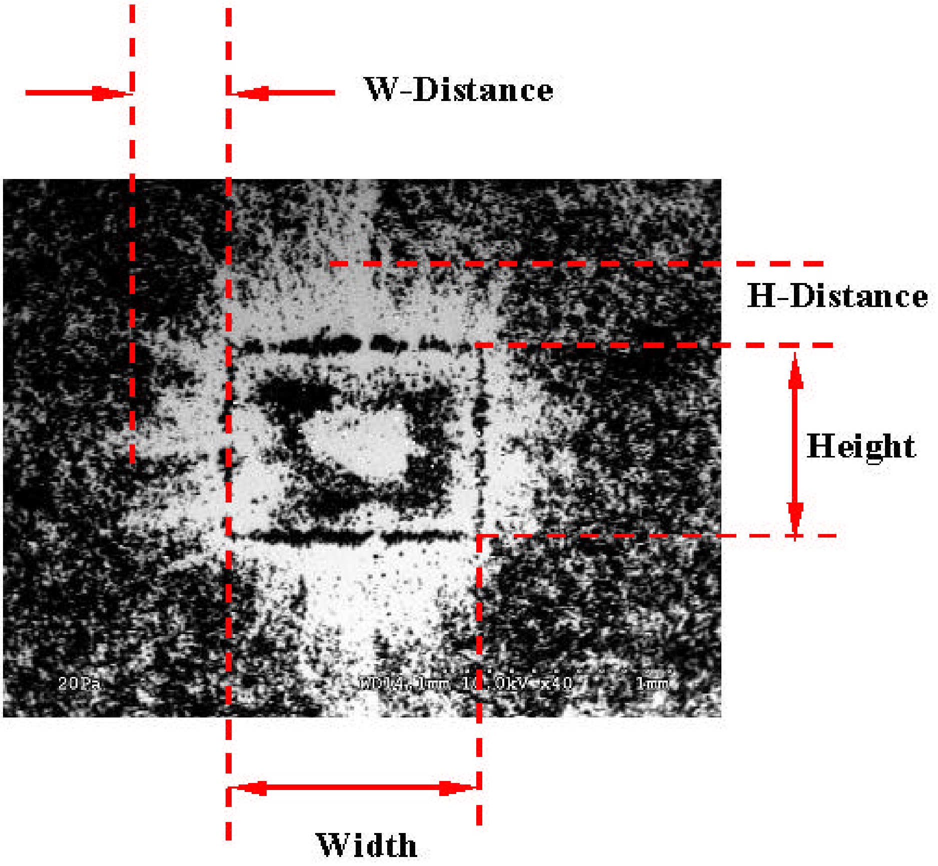

Figure 5.4 Dimensional description of the width and height of the black rectangle, and the distance of the brighter surrounding area. The H-Distance is defined in the height direction and W-Distance in the width direction

Table 5.1 Measurement of the black rectangle size for varying magnification

Magnification	Measured (pixel)		Calculated (pixel)		Measured/Calculated	
	Width	Height	Width	Height	Width Ratio	Height Ratio
150	401	290	341	256	1.17	1.13
300	230	168	171	128	1.35	1.31
500	142	108	102	77	1.39	1.4
1000	84	62	51	38	1.64	1.61

*Resolution is 1280×960 pixels

Table 5.2 Measurement of the W-Distance & H-Distance for varying magnification

Magnification	W-Distance (pixel)	H-Distance (pixel)	W-Distance/Width	H-Distance/Height
150	87	62	0.22	0.21
300	60	50	0.26	0.3
500	45	62	0.32	0.57
1000	41	53	0.5	0.85

*Resolution is 1280×960 pixels

shape when the magnification increases. The ultimate situation is the point scan mode, which has a symmetry distribution of the surface electric field.

5.2.2 Scanning Speed Effect – Varying the Dose Rate

In SEM, the image is formed by divided the object as small units (pixels) and the pixels are scanned in turn, which is in a regular raster and made up of scanned lines. At the resolution normally used in scanning, 640×480 pixels, the electron beam has different scanning speed such as:

TV 2 – 33 ms per frame of 480 lines
Slow 2 – 2 seconds per frame of 480 lines
Slow 4 – 25 seconds pre frame of 480 lines

Assume T is the time per frame, the pixel time t on each pixel can be calculated as

$$t = \frac{T}{640 \times 480} \tag{5.2}$$

The pixel times for these three scanning speeds are thus 0.1µs per pixel for TV 2, 6.5µs per pixel for Slow 2, and 81µs per pixel for Slow 4, respectively. The dose density is proportional to the dwell time of each pixel, thus the relative dose rate of these three scanning speed is the reason of the charging behavior difference and toner powder pattern variation. Quartz was irradiated with various scanning speeds and figure 5.5 shows the resulting toner powder patterns and the relationship curve between surface potential and scanning rate. Although the range of the bright region shrinks with slower scanning speed, the toner powder inside the irradiation area is more uniformly distributed. Changing the scan speed for a given magnification and beam current therefore results in a very wide variation in the dose rate (C/second) into each pixel of the image. This effect is widely exploited in the SEM observation of charging samples. Charging is rate dependent because the charge/discharge process requires a finite time constant t

$$t = CR \tag{5.3}$$

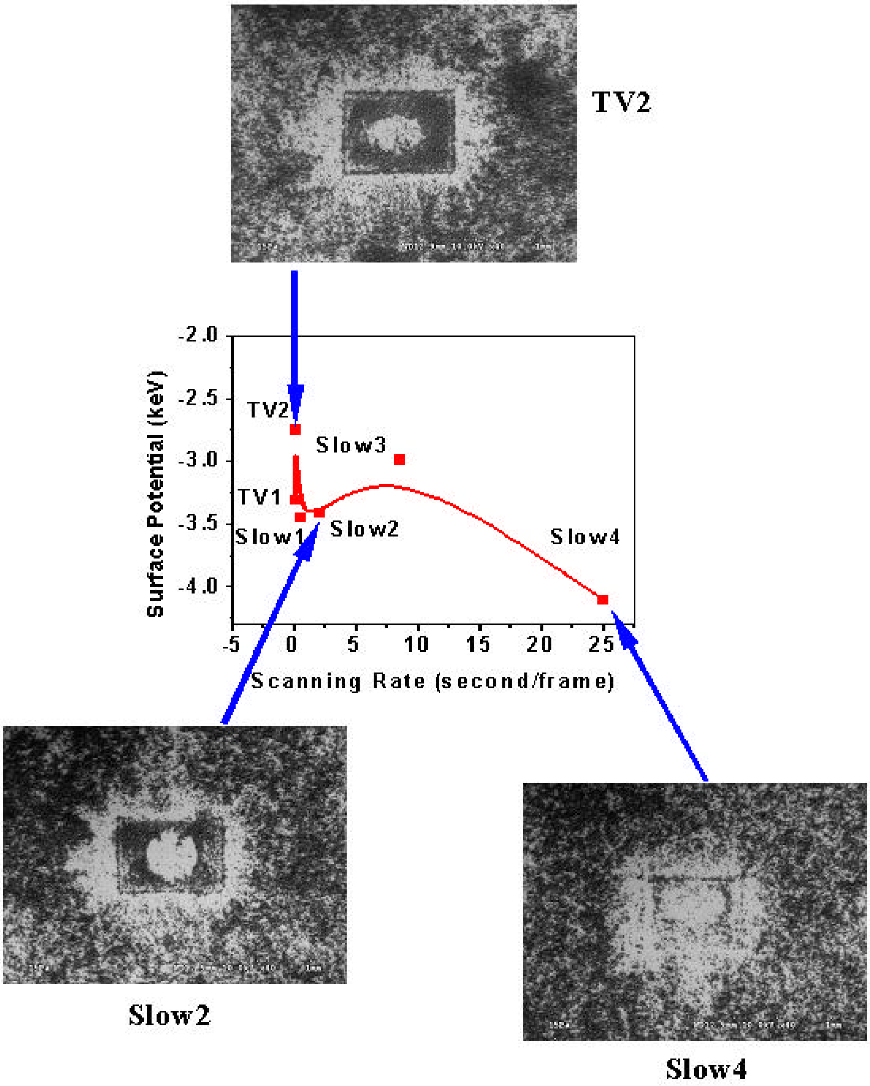

Figure 5.5 Variation of the toner powder patterns with scanning speed. Quartz substrate was irradiated by 20keV electron beam in 5Pa gas with magnification 150×.The scanning rates are TV2-33ms/frame, Slow2-2s/frame, and Slow4-25s/frame at 60Hz. Scanning time 30seconds. The resulting patterns were observed by a 10keV electron beam, magnification 40×, and 15Pa air. Center is the relationship of surface potential and scanning speed in 5Pa air environment on quartz surface. Incident beam energy is 20keV, working distance 13mm.

here C and R are capacitance and resistivity of a RC circuit formed by the dielectric sample.

5.2.3 Gas Pressure Effect – Charge Compensation

The quartz surface with pre-applied toner powder was exposed under 15keV electron beam and variable gas pressure, and the patterns were shown in figure 5.6. The depleted region both inside and outside the rectangular frame will decrease while the particle cluster will form inside the frame with the increasing gas pressure. The picture of 1Pa in figure 5.6 shows a pattern which is suggestive of a flashover caused by dielectric breakdown. Similar images have also been observed at higher electron beam energy. These series of patterns confirm that there is a transition from negative to positive charging beyond 10Pa gas pressure, which agrees with the charging data determined by measuring the Duane-Hunt (D-H) cut-off of the x-ray spectrum from quartz, which is shown at the center of figure 5.6.

The variation of the toner powder patterns indicates how the gas pressure changes the surface potential so as the distribution of the electric field. For both patterns of 0.2Pa and 1Pa, they have high degree of charging, large extent of the electric field, and inhomogeneous surface potentials. As the gas pressure increases, the surface potential decreases and tends to become homogeneous, toner powder cluster begin to accumulate inside the rectangle, while the brighter surrounding area outside the black rectangle reduces steadily because the attractive effect of the electric field to the toner powder is decreased. When the gas pressure reaches about 10Pa, surface potential is homogeneous and low, with less ability to attract toner powder from both inside and outside the rectangle.

The theoretical and measured values of the rectangle size are listed in table 5.3 and the measured distance of the brighter surrounding area and the relative ratio to the rectangle size are listed in table 5.4. The data in table 5.3 illustrate that the black rectangle size continues shrink with increased gas pressure and close to the calculated value, which is the charge-free condition.

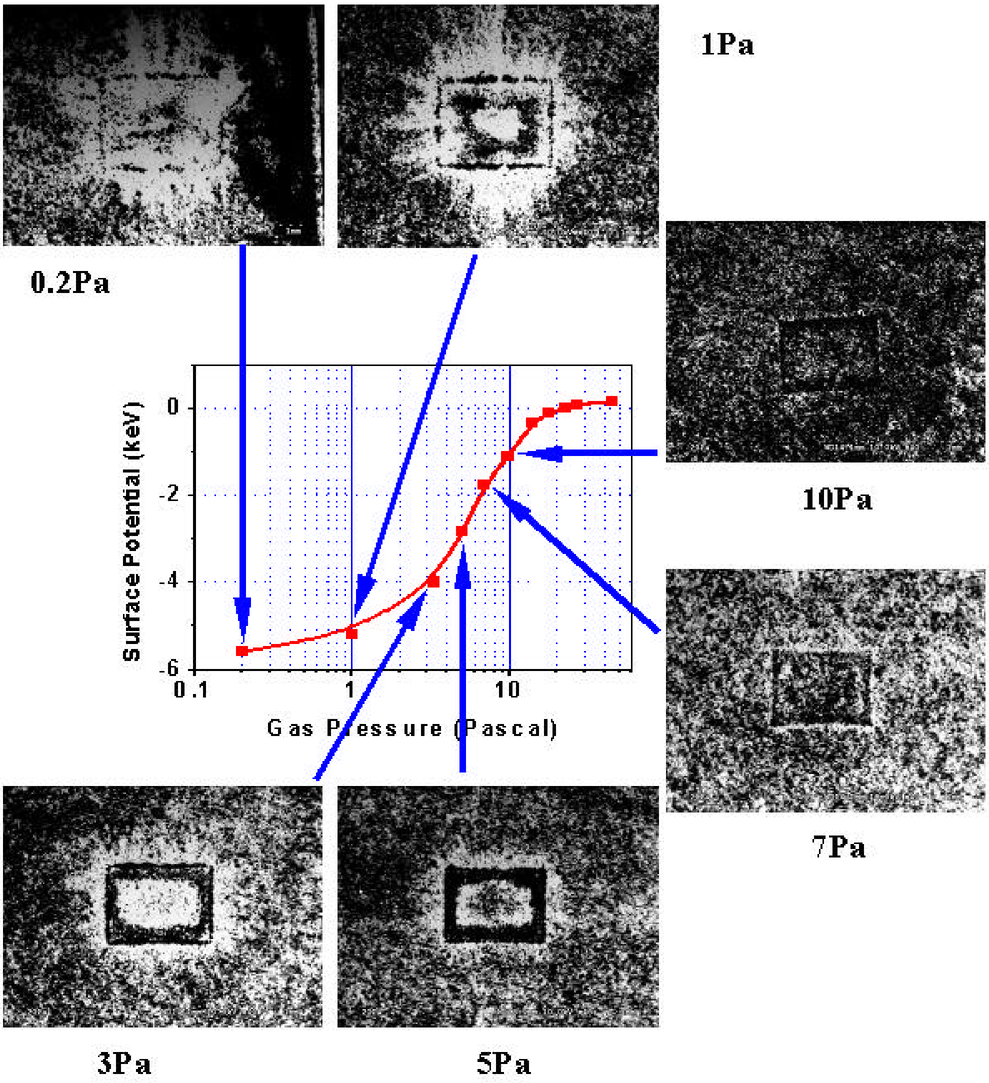

Figure 5.6 Variation of the toner powder patterns with gas pressure. Quartz substrate was irradiated by 20keV electron beam, magnification is 150×, the scanning speed is TV1 16ms/frame at 60Hz, and duration time 30seconds. The resulting patterns were observed by a 10keV electron beam at magnification 40×. Center is the relationship of surface potential and gas pressure on quartz surface. Incident beam energy is 15keV, working distance 13mm, and magnification 150×.

Table 5.3 Measurement of the black rectangle size for varying gas pressure

Pressure (Pa)	Measured (pixel)		Calculated (pixel)		Measured/Calculated	
	Width	Height	Width	Height	Width Ratio	Height Ratio
0.2	486	382	341	256	1.42	1.49
1	464	354	341	256	1.36	1.38
3	430	310	341	256	1.26	1.21
5	402	288	341	256	1.18	1.13
7	390	281	341	256	1.14	1.1
10	391	278	341	256	1.15	1.09

*Resolution is 1280×960 pixels

Table 5.4 Measurement of the W-Distance & H-Distance for varying gas pressure

Pressure (Pa)	W-Distance (pixel)	H-Distance (pixel)	W-Distance/Width	H-Distance/Height
0.2	161	204	0.33	0.53
1	139	194	0.3	0.55
3	129	116	0.3	0.37
5	86	63	0.21	0.22
7	36	27.5	0.09	0.1
10	16	23	0.04	0.08

*Resolution is 1280×960 pixels

In addition the data in table 5.4 confirm the above analysis related with the variation of the toner powder patterns, which show that the distance outside of the black rectangle decreased quickly both in width and height directions when the gas pressure rises from 0.2 to 10Pa.

5.2.4 Beam Energy Effect – Charge Balance

As demonstrated elsewhere in this thesis, beam energy will also affect the surface charging state greatly because of the change in charge yields and such effect is reflected by the toner powder distribution. Such correlation is verified by comparing the toner particle patterns, which is shown in figure 5.7, with the relationship curve of beam energy and surface potential, which is obtained from measuring the Duane-Hunt cutoff.

At low beam energy (6keV or below) the pattern, which is different from that usually observed, has toner powder cluster inside the irradiation area without the black edge rectangle. That is because the surface is locally positive-charged and the electric field generated will repel the toner powder, which has positive charge initially. As the beam energy increases, the surface potential becomes negative and the electric field is intensified due to the decreased SE yield. The rectangle pattern appears at 7keV beam energy and the features of this kind of pattern are intensified for the higher beam energy range. The toner powder inside the rectangle disappears at around 15keV beam energy while the black edge of the rectangle is wider, with the expanding of the brighter surrounding area outside the rectangle. Such phenomena proved the assumption that the toner powder in the edge comes from both inside and outside the rectangle due to the electric attractive effect. The inversion of the depleted region from the frame to both inside and outside the frame starts between 6 and 7keV. Thus the toner powder pattern can be the monitor for the surface charging state.

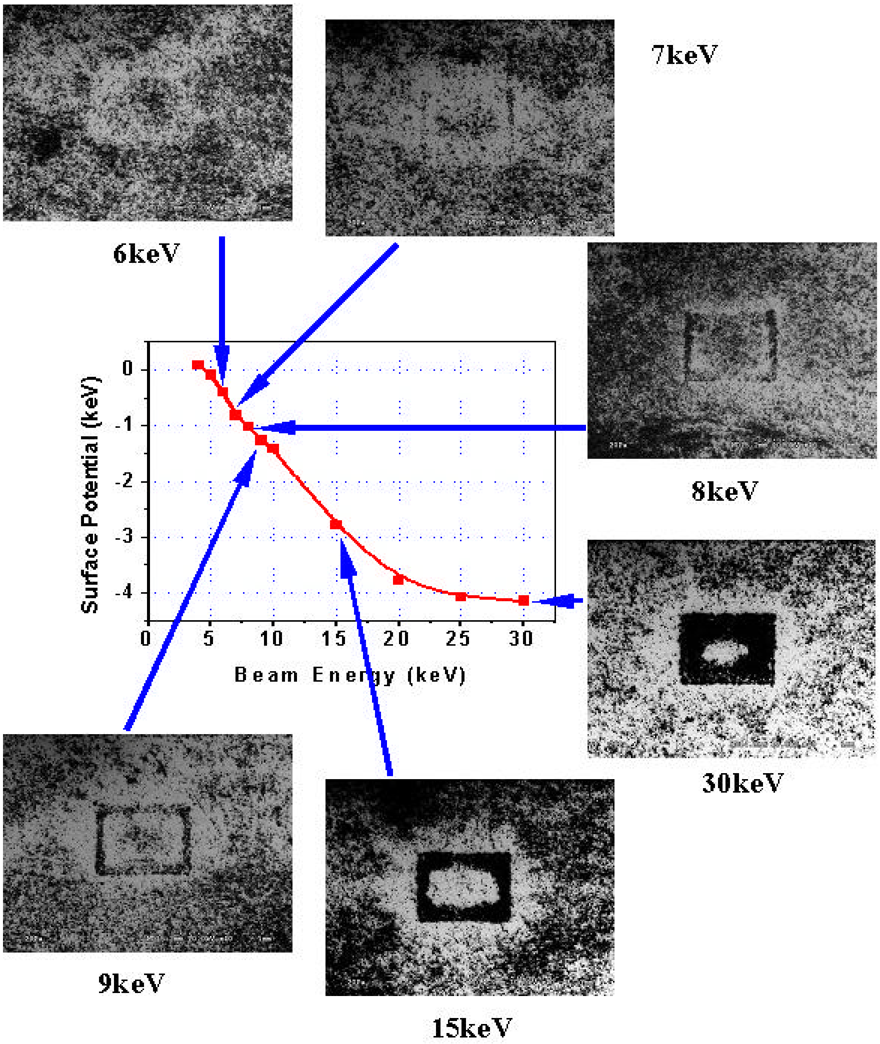

Figure 5.7 Variation of the toner powder patterns with incident beam energy. Quartz substrate was irradiated by 6, 7, 8, 9, 15, 30keV electron beam in 5Pa air environment, magnification is 150×, the scanning speed is TV1 16ms/frame at 60Hz, and duration time 30seconds. The resulting patterns were observed by a 10keV electron beam at magnification 40×. It also shows the relationship of surface potential and incident beam energy on quartz surface in 5Pa air environment. Incident beam energy varies from 5 to 30keV, working distance 14mm, magnification 150×.

5.3 Discussion

The figures above show toner powder patterns which are observed at low magnification after exposure to the e-beam. These experiments clearly demonstrate how the experimental parameters affect the surface electric field, and how these Lichtenberg patterns help to elucidate the changes in charging behavior with beam condition. In order to understand the better we need to develop a basic theory of pattern formation. We can assure that the toner is positively charged initially and the density of the deposited electron dose is proportional to electric field intensity. Since particles will move in an applied field, the pattern can indicate how the surface electric fields are distributed and what their intensities are. A heavier particle density means a stronger positive charge while a depleted region corresponds to negative charge. These series of patterns thus agree with the corresponding charging data determined by measuring the Duane-Hunt (D-H) cut-off of the x-ray spectrum from quartz. These figures also show that charge field can extent for hundreds of microns away from the charged region.

The pattern phenomena can be interpreted by the classical double-layer model[Hoffmann 1992]. When the electron beam hits the insulator, a thin surface layer will be positively charged due to the secondary electron emission. The thickness of this layer is about 50nm for insulator. The incident electrons will penetrate deeper inside until they finally come to rest, excluding the back-scattered electrons. The incoming electrons thus form an embedded negative charge zone, which has micrometer range R, is determined by the beam's energy and the density d_m of the sample [Seiler 1983]

$$\frac{R}{nm} = \frac{1.15\times10^{5}}{d_m/(kg/m^{3})}\left(\frac{E_{PE}}{keV}\right)^{1.35} \tag{5.4}$$

When the incident electron beam bombard the insulator surface, the charge density r_+ and r_- vary with time as

$$r_+(t) = \frac{I_0 d}{d_s} t$$
$$r_-(t) = \frac{I_0 (h - 1)}{d_p} t \qquad 5.5$$

here I_0 is the incident current, d_s and d_p are the thickness of positive charge layer and negative charge layer respectively, d the SE yield coefficient, h the BSE yield coefficient. When an incident electron beam with high enough energy irradiates the surface of good insulator, the charge density and surface potential linearly increase with time until the breakdown potential is reach. On the other hand, if the sample is a poor insulator, the electric charge distribution quickly reaches a stable state because of the large leakage current that can flow and the surface potential is then held at a constant value, which depends on the incident beam current, energy and the leakage rate. The processes for surface breakdown or surface potential stabilization always quickly occur.

We can treat the sample studied as being an infinite medium since the irradiated area is much smaller than the whole specimen. The field distribution created by the trapped charge has a sign either centrifugal or centripetal, which depends on the sign of trapped charge. There also exists an inversion point at which the field changes direction, or field is zero. At the lower scanning magnification used (20×), the penetration range of incident electron is small (around 5 micron) compared with the scanning area (1mm). Thus the double layer model can be simplified as the net charge model, which means all the negative charges are uniformly distributed inside a thin disk on sample surface. Figure 5.8 shows the equal-potential distribution of the electric field through the cross section of sample by the Quick Field simulation [http://www.tera-analysis.com], which is based on solving the two dimensional Poisson equation.

$$\nabla^2 V(x, y) = -\frac{r(x, y)}{c} \qquad 5.6$$

here we assume a uniform dielectric permittivity c, $r(x, y)$ is the charge density uniformly distributed right below the sample surface, $V(x, y)$ is the unknown electrical potential to be

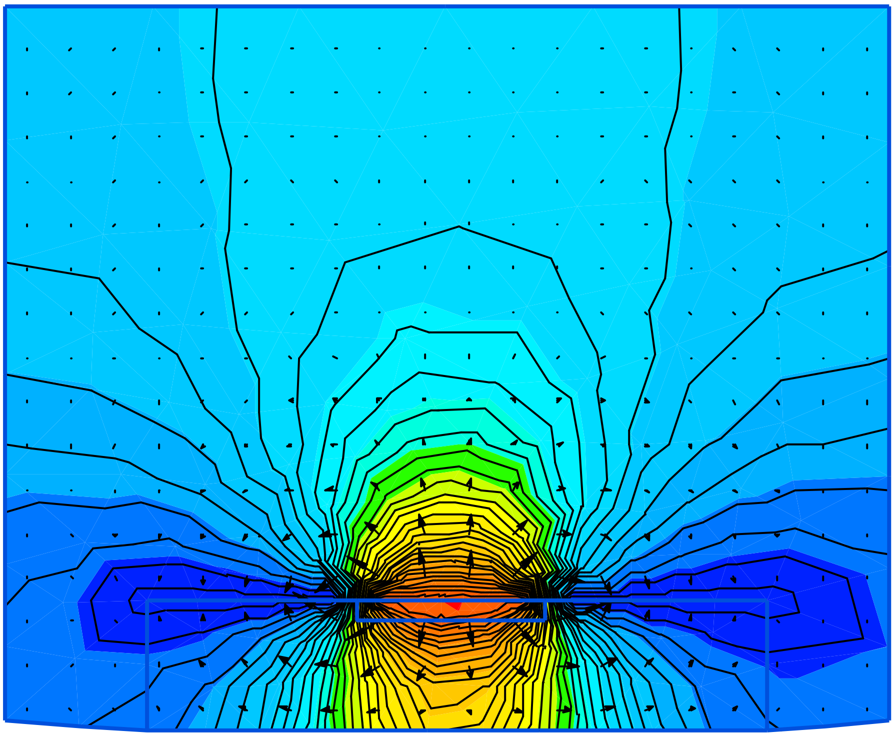

Figure 5.8 The simulation of the equal-potential distribution of the surface electric field through the cross section of quartz based on QuickField©. Assume uniform charge density; uniform dielectric permittivity. The boundary conditions include the surface potential is 3000 volts equally distributed within the charge-stored area while zero volt on the remaining sample area and the chamber wall. Grid units are millimeters.

solved. In addition, boundary conditions are given as: the surface voltage of charged area V (0,0) is 3000 volts; the other sample area and the chamber wall are to be considered as good grounded, with the voltage of zero [Tang et al. 2003b].

The voltage distribution and electric force distribution of the electric field are calculated and shown in figure 5.9 [Cazaux 1986]. It is clear that the edges of the charging disc in figure 5.8 have the maximum electric field intensity, corresponding to the peak value in figure 5.9.

Along the radial direction (r) on the disc surface (z = 0), the electric field F_r has the general expression as

$$F_r(r,0) = \frac{rd}{2e} f_r^i(r,0) \text{ for d<<a} \qquad 5.7$$

here $f_r^i(r,0) = \frac{2a}{pr}[J_1(\frac{r}{a}) - J_2(\frac{r}{a})]$ for r<a,

and $f_r^0(r,0) = \frac{2}{p}[J_1(\frac{a}{r}) - J_2(\frac{a}{r})]$ for r>a.

J_1 (k) and J_2 (k) are the elliptic integrals (k=a/r or k=r/a):

$$J_1(k) = \int_0^{p/2} \frac{dy}{(1-k^2 \sin^2 y)^{1/2}},$$

$$J_1(k) = \int_0^{p/2} (1-k^2 \sin^2 y)^{1/2} dy \ .$$

y is an auxiliary variable related to j, which is the angular variable in cylindrical coordinates and $j = p - 2y$.

The expression of surface potential V (r, 0) can be deduced by integrating F_r (r, 0) as:

$$F_r(r,0) = -\partial V(r,0)/\partial r \qquad 5.8$$

The migration of small particles to form a Lichtenberg image is driven by an electric force due to the gradient of the surface electric field. Such particles are attracted by the electric field gradient until they reach the equilibrium position where $\partial F/\partial r = 0$, producing patterns which reveal the field structure. As the beam turns off, the net electric charge density r (sum of the negative and positive charge) inside the sample decays with time as the following equation

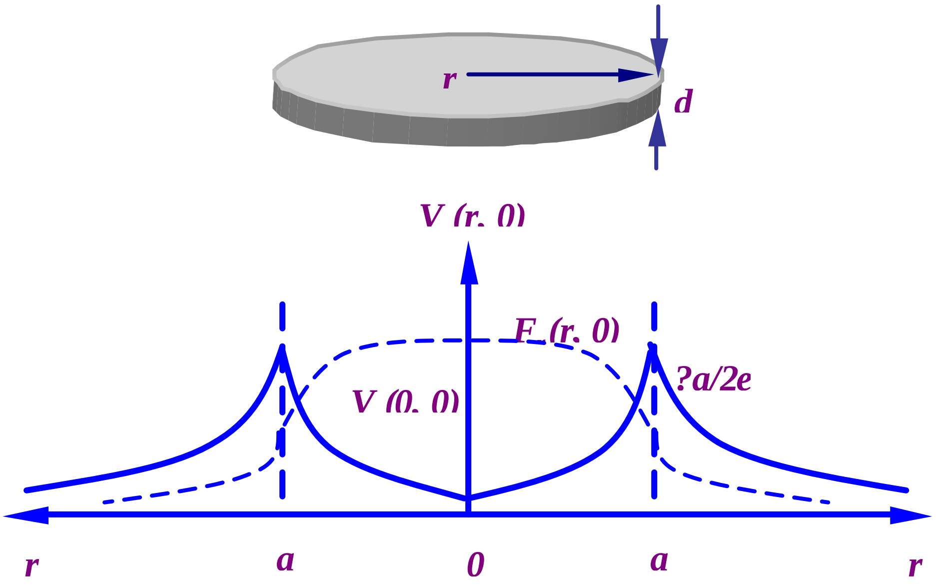

Figure 5.9 The electric field (solid line) and potential (dash line), which created by a uniformly distributed charge inside a disc, plotted as a function of radius r.

$$r(t) = r(0)e^{-t/t} \tag{5.9}$$

where $t = e/k$, k is electrical conductivity, e is dielectric constant. For the sample used in experiment, quartz has a large time constant t of about 10 days resulting a slow decay, which is the reason why toner powder can attach on the surface for a long time without changing the initial pattern [Lee 1927]. The charge decay is the result of the recombination of surface positive charge with negative charge in the bulk. Such discharge phenomena can be described by the discharge of a RC circuit with time constant t .

Since the toner powder pattern is affected by the variation of surface electric field, which can be controlled by adjusting the operation parameters, this could be the basis of a nano-Xerox process with a suitable 'powder' and a means of generating patterns.

5.4 Conclusion

The migration of small particles to form a Lichtenberg image is driven by the surface potentials, which are a direct function of the distribution of high-energy electrons at the surface. The combination of the PPM, nanoparticles, and the Lichtenberg technique might permit high-resolution direct metal imprinting.

References

Baer, D. R., M. H. Engelhard, D. J. Gaspar, A. S. Lea and C. F. Windisch Jr. (2002). *Surf. Interface Anal.* **33** p781-790.

Baglin, V., Y. Bozhko, O. Gröbner, B. Henrist, N. Hilleret, C. Scheuerlein, M. Taborelli, *http://clic-structures-working-group.web.cern.ch/clic-structures-working-group/min/2000/18-9-2000/noel.pdf.*

Bai, M., R. F. Pease, C. Tanasa, M. A. McCord, D. S. Pickard, and D. Meisburger (1999). *J. Vac. Sci. Technol.* B **17**, (6), p2893-2896.

Belhaj, M., O. Jbara, M. N. Filippov, E. I. Rau, and M. V. Andrianov (2001). *Appl. Surf. Sci.*, **177** p58-65.

Bigelow W. C. (1994). *Vacuum Methods in Electron Microscopy in Practical Methods in Electron Microscopy*, **15**, (Portland Press, London).

Bird, G. A. (1976). *Molecular Gas Dynamics*. (Oxford Univ. Press, London).

Bird, G. A. (1994). *Molecular Gas Dynamics and the Direct Simulation of Gas Flows*. (Clarendon Press, Oxford).

Bolon, R. B., C. D. Robertson, and R. Lifshin (1989). *Microbeam Analysis*, p449.

Cazaux, J. (1986). *J. Appl. Phys*., **59**, 5 p1418-1430.

Cazaux, J. (1999a). *J. Appl. Phys.,* **85**, p1137-1147.

Cazaux, J. (1999b). *J. Electron Spectrosc. Relat. Phenom.* **105**, 155-185.

Cazaux, J. (2001). *J. Appl. Phys.* **89**, p8265.

Cazaux, J. (2004). *J. Appl. Phys*. **95**, p731-742.

Cazaux, J., P. Lehuede (1992). *J. Electron Spectrosc. Relat. Phenom.* **59**, 49-71.

Cercignani, C. (1988). *The Boltzmann equation and its application*. (Springer Press, New York).

Crawford, C. K. (1979). *Scanning Electron Microscope,* p31-46.

Cros, A. (1992). *J. Electron Spectrosc. Relat. Phenom*. **59**, p1-14.

Danilatos, G. D. (1988). *Adv. Electronics Electron Phys*. **71**, 109-249.

Danilatos, G. D. (1991). *Microbeam Analysis*, p201-203.

Duane W., Hunt F. L. (1915). *Proc. the American Physical Society* **VI** No.2, 166-171.

Echlin, P., A. Saubermann, and P. Taylor (1975). *Scanning Electron Microscope*, **I**, p680.

Farley, A. N., and J. S. Shah (1990). *J. Microscopy*, **158**, Pt 3, p389-401.

Fletcher, A. L., B. L. Thiel, and A. M. Donald (1997). *J. Phys. D: Appl. Phys*., **30**, p2249-2257.

Fuchs, W., J. D. Brombach, and W. Trösch II (1978). *Scanning Electron Microscope*, p63-74.

Goldstein J. I., D. E. Newbury, P. Echlin, D. C. Joy, A. D. Romig, Jr., C. E. Lyman, and C. Fiori (1992). *Scanning Electron Microscopy and X-Ray Microanalysis*, (Plenum Press, New York).

Gong, H., C. Le Gressus, K. H. Oh, X. Z. Ding, C. K. Ong, and B. T. Tan (1993). *J. Appl. Phys*., Vol. 74 p1944-1948.

Griffin, B. J., A. A. Suvorova (2003). *Microscopy and Microanalysis*, **9**, Issue 2, p155-165.

Gross, B., G. M. Sessler, and J. E. West (1974). *J. Appl. Phys*., **45**, p2841.

Guo, H., W. Maus-Friedrichs and V. Kempter (1997). *Surf. Interface Anal*. **25** p390-396.

Hofmann, S. (1992). *J. Electron Spectrosc. Relat. Phenom*. **59**, p15-32.

http://electronics.howstuffworks.com/photocopier5.htm

http://www.scioncorp.com

http://www.tera-analysis.com

Ichinokawa, T., M. Iiyama, A. Onoguchi, and T. Kobayashi (1974). *Japanese J. Appl. Phys*., **13**, p1272-1277.

Jbara, O., B. Portron, D. Mouze, and J. Cazaux (1997). *X-Ray Spectrometry*, **26**, 291-302.

Joy, D. C. (1987). *Microbeam Analysis*, San Francisco, p105-109.

Joy, D. C. (1995). *Monte Carlo Modeling for Electron Microscopy and Microanalysis*, (Oxford Univ. Press, New York).

Joy, D. C. (2004). *International SEMATECH Inc*.

Joy D. C., and C. S. Joy (1996). *Micron*, **27**, p247-263.

Kelvin, Lord (1901). *Philos. Mag*., **2**, p1-40.

Lee, E. S., and C. M. Foust, (1927). *General Electric Review*, **30**, 3 p135-145.

Le Gressus, C., F. Valin, M. Gautier, J. P. Duraud, J. Cazaux, and H. Okuzumi (1990). *Scanning*, **12**, p203-210.

Larrabee, R. D. and M. T. Postek (1993). *Solid State Electron*. **36**, No. 5, 673.

Le Gressus, G. and G. Blaise (1991). *J. Appl. Phys*. **69**, 6325.

Le Gressus, G. and G. Blaise (1992). *J. Electron Spectrosc. Relat. Phenom*. **59**, p73-96.

Lichtenberg, G. C. (1777). *Novi. Comment. Gö tt*., **8**, 168.

MacDonald, E. and T. Iwayanagi (1989). *Materials and Processes, ACS Symposium Series* (American Chemical Society, Washington, DC).

MacDonald, N. C., P. W. Palmberg, G. E. Riach, and R. E. Weber (1976). *Handbook of Auger Electron Spectroscopy*, edited by Lawrence E. Davies.

Mathieu, C. (1999). *Scanning Microscopy*, **13**, no.1, p23-41.

Melchinger, A., and S. Hofmann (1995). *J. Appl. Phys*. **78**, (10) p6224-6232.

Meredith, P., A. M. Donald, and B. L. Thiel (1996). *Scanning*, **18**, p467-473.

Merrill, F. H., and A. Von Hippel (1939). *J. Appl. Phys*., **10**, p837.

Moncrieff, D. A., P. R. Barker, and V. N. E. Robinson (1979). *J. Phys. D: Appl. Phys*., **12**, p481-488.

Moncrieff, D. A., V. N. E. Robinson, and L. B. Harris (1978). *J. Phys. D: Appl. Phys*., **11**, p2315-2325.

Myklebust, R. L., C. E. Fiori, and D. E. Newbury (1990). *Microbeam Analysis*, p147-149.

Fiori C. E., C. R. Swyt, and R. L. Myklebust (1992). *DTSA – Desk Top Spectrum Analyzer* (US Patent 529913).

Neilde, A., and N. I. Morimoto (2002). *Comput. Nanoscience Nanotechnology*, p340-343.

Newbury, D. E. (1976). *Scanning Electron Microsc.* **1**, p112-119.

Newbury, D. E. (2000). *Scanning*, **22**, p345-351.

Newbury, D. E. (2002). *J. Res. Natl. Inst. Stand. Technol*., **107**, p567-603.

Oh, K. H., C. K. Ong, B. T. G. Tan, and G. Le Gressus (1993). *J. Appl. Phys*. **74**, p6859-6865.

Pantano, C. G. and T. E. Madey (1981). *Appl. Surf. Sci*., **7**, p115.

Pawley, J. B. (1972). *Scanning Electron Microscope*, p153-160.

Pfefferkorn, G. E., H. Gruter, and M. Pfautsch (1972). *Scanning Electron Microscope*, p147-152.

Pireaux, J. J., M. Vermeersch, and R. Caudano (1992). *J. Electron Spectrosc. Relat. Phenom.* **59**, p33-48.

Postek, M. T. and D. C. Joy (1987). *J. Res. Nat. Bur. Standards* **92**, No. 3, 205.

Postek, M. T., and A. E. Vladár (2004). *Microscopy Today*, **12**, No.1.

Reimer, L. (1985). *Scanning Electron Microscope, Springer Series in Optical Science* (Springer, Berlin).

Robinson V. N. E. (1975a). *J. Phys. E: Sci. Instrum.* **8**, p638-640.

Scarce, R. I. (1994). *Solid State Tech.* **37**, 43.

Seiler, H. (1983). *J. Appl. Phys.*, **54**, pR1-R18.

Shackelford, J. F., and W. Alexander (2000). *CRC Materials Science and Engineering Handbook, 3rd edition.* (CRC Press).

Shaffner, T. J. and J. W. S. Hearle (1976). *Scanning Electron Microscope*, p61-82.

Sharipov, F. (2001). *J. Braz. Soc. Mech. Sci.* **23**, p.441-452.

Soane, D. S. and Z. Martynenko (1989). *Polymers in Microelectronics* (Elsevier, Amsterdam).

Solosky, L. F. and D. R. Beaman (1972). *The Review of Scientific Instruments*, **43**, p1100-1102.

Song, Z. G., C. K. Ong, and H. Gong (1996). *J. Appl. Phys.* **79**, (9), p7123-7128.

Stratton, J. A. (1941). *Electromagnetic theory*, (McGraw-Hill Press, New York).

Tang, X. and D. C. Joy (2002). Microscopy and Microanalysis, 1540CD.

Tang, X. and D. C. Joy (2003a). *Scanning*, **25**, p194-200.

Tang, X. and D. C. Joy (2003b). Microscopy and Microanalysis, 980CD.

Taylor, D. M. (1976). *Scanning Electron Microscope*, p2269-2279.

Toth, M., and M. R. Philips (2000). *Scanning*, **22**, p370-379.

Toth, M., B. L. Thiel, and A. M. Donald (2002). *J. Microscopy*, **205**, p86-95.

Townsend, J. S. E. (1915). *Electricity in Gases.* (Clarendon Press, Oxford).

Vigouroux, J. P., J. P. Duraud, A. Le Moel, C. Le Gressus, and D. L. Griscom (1985). *J. Appl. Phys.* **57**, 5139.

Von Engel, A. (1955). *Ionized Gases*, (Clarendon Press, Oxford).

Witty, D. B. and C. J. Wu (1975). *Scanning Electron Microscope*, p441-446.

Wurster, R. (1986). *Scanning*, **8**, p69-73.

Yu, X., and H. Hantsche (1990). *J. Electron Spectrosc. Relat. Phenom*. **50**, p19-29.

Appendix

GASFLOW code wrote in Visual Basic

```
'Molecule passing through the tube and plot the pressure distribution
'Based on the model from Bird. (C) Copyright Xiaohu Tang, Sep, 09, 2002
'Revised by March, 03, 2004

Option Explicit
Dim RM, two_pi As Double                  'RM is the distance from the tube axes to start point
Dim Theta As Double                 'Theta is the angle of hitting point projected on cross section circle
Dim CenX, CenY, Bottom, Radius, Length, LeftEdge, RightEdge As Double       'these variables are used to describe the projection figure
Dim TL As Double                          'TL is the ratio of length to radius of cross section
Dim NT, ND, N, NTT As Double              'NT for number of molecules bounce through, ND for number of molecules direct through, NTT for number of molecules total through
Dim R As Double                           'R is the radius of cross section for projection figure
Dim cx, cy, cz As Double                  'Direction cosine for initial bounce
Dim X0, Y0, Z0, X1, Y1, Z1, X, y, Z, X2, Y2, Z2, X3, Y3, Z3 As Double              'X1, Y1, Z1 as the coordination of starting point, X, Y, Z for next point, X2, Y2, Z2, X3, Y3, Z3 as selective
Dim A, B, C, D, E As Double               'All used for solving the bounce angle
Dim CenCircleX, CenCircleY As Double                'Center of the circle in cross-section figure
Dim Alpha, Alpha1, Alpha2 As Double          'To represent the point after bouncing in projection figure
Dim Phi, Phi1, Phi2 As Double                  'Calculate the bouncing angle
Dim CoX, CoY, Radius2 As Double                'Draw the co-center circle
Dim Step1, Step2, Step3 As Double               'Describe the spatial steps of molecules
Dim I                                        'the number of co-circle rings
Dim pi, Max, Min As Double                     'Constant
Dim AA, BB                                    'Used in directional cosine calculation
Dim Slope, Slope1, Slope2, Slope3 As Double       'Used in bounce point calculation
Dim Check                                     'Check the symbol
Dim Xp, Yp As Double                            'Point position in cross-section
Dim Dp, OX, OY As Double                         'the ratio of out distance to radius
Dim TP, BM, center_x, center_y, Cc1, Cc2, DD, S0, S1, k1, k2
Dim LE, RE, Xaxis, Ratio
Dim number (1 To 2000) As Double                'array of molecule in different rings
Dim pressure (1 To 2000) As Double               'pressure of different rings
Dim AA1, BB1
Dim Tubeangle, LineLength As Double              'this is the slope angle of the tip of the tube
Dim TDA, TDB                                'For the purpose of definition of two-dimensional array
Dim XUnit, YUnit                'Define the unit value of frame so as to paint the desired particle density
```

```
Dim Rate As Single                          'the ratio of no. Directly pass to no. Bounce


Private Sub Contour_Click ()
  Imgdemonstration.Cls                        'clear the pictures each time

  Dim Xellipse, Yellipse
  Call Prameter (pi, two_pi, center_x, center_y, TP, BM, R, LE, RE, Cc1, Cc2, TL, Dp, DD, NTT, Xaxis, Ratio, OX, OY, AA1, BB1, LineLength)
  Tubeangle = (AngleofTube.Text) * pi / 180

  Xellipse = Xaxis
  Yellipse = LineLength - Ratio / Tan (Tubeangle)

  XUnit = Imgdemonstration.ScaleWidth / 100
  YUnit = Imgdemonstration.ScaleHeight / 100

  Imgdemonstration.Line (AA1, 0)-(AA1, Yellipse), RGB (0, 0, 255)
  Imgdemonstration.Line (BB1, 0)-(BB1, Yellipse), RGB (0, 0, 255)
  If AngleofTube.Text = 90 Then
    Imgdemonstration.Line (AA1, LineLength)-(BB1, LineLength), RGB (0, 0, 255)
  ElseIf Tan (Tubeangle) >= 1 Then
    FillStyle = 1
    Imgdemonstration.Circle (Xellipse, Yellipse), Ratio, , , , 1 / Tan(Tubeangle)     'Draw a hollow ellipse
  Else: FillStyle = 1
    Imgdemonstration.Circle (Xellipse, Yellipse), Ratio / Tan (Tubeangle), , , , 1 / Tan (Tubeangle)  'draw a hollow ellipse
  End If

  y = DD + 1                                          'Give the initial value
  NT = 0
  ND = 0

  Dim I, J
  Static dblMatrix (1 To 100, 1 To 100) As Double
  For I = 1 To 100
    For J = 1 To 100
      dblMatrix(I, J) = 0
    Next J
  Next I
```

```
For N = 1 To NTT
    RM = Sqr (Rnd)
    Theta = two_pi * Rnd
    X0 = RM * Cos (Theta)
    Y0 = RM * Sin (Theta)
    Z0 = 0                                                  'staring point position

  Call DCEM (cx, cy, cz)
  A = cx / cy
  B = A * Y0 - X0
  D = -(B / (1 + A * A))
  E = A * Sqr(Abs((B * B) - (1 + A * A))) / (1 + A * A)
  Phi1 = Atn (-(D + E) / Sqr (-(D + E) * (D + E) + 1)) + 2 * Atn (1)
  Phi2 = Atn (-(D - E) / Sqr (-(D - E) * (D - E) + 1)) + 2 * Atn (1)        'calculate renounce angle
    If Abs (Phi1 - Theta) < pi Then Phi = Phi1                             'Determine the renounce angle
    If Abs (Phi1 - Theta) >= pi Then Phi = Phi2
  X1 = Cos (Phi)
  Y1 = Sin (Phi)
  Z1 = ((Y1 - Y0) / cy) * cz
  S0 = Sqr ((Y1 - Y0) ^ 2 + (X1 - X0) ^ 2)
  If Z1 <= 0 Then
  ElseIf Z1 >= (TL - (1 - Sin (Phi) / Tan (Tubeangle))) Then                    'GoTo its_gone
    ND = ND + 1
    NT = NT + 1
    X2 = X1 + (y + Y1) * cx / cy
    Z2 = (y + Y1) * cz / cy- TL + Z1
    If Z2 <= 0 And AngleofTube.Text = 90 Then                                   'GoTo Repeat
    Else
    Imgdemonstration.PSet (Xaxis + X2 * Ratio, Z2 * Ratio + LineLength), RGB (0, 0, 255)
      If (Xaxis + X2 * Ratio) >= Int (Xaxis + X2 * Ratio) Then
        I = CLng (Int ((Xaxis + X2 * Ratio) / XUnit)) + 1
      Else: I = CLng (Int ((Xaxis + X2 * Ratio) / XUnit))
      End If
      If (Z2 * Ratio + LineLength) >= Int (Z2 * Ratio + LineLength) Then
        J = CLng (Int ((Z2 * Ratio + LineLength) / YUnit)) + 1
      Else: J = CLng (Int ((Z2 * Ratio + LineLength) / YUnit))
      End If
      TDA = I
      TDB = J
```

```
    For I = 1 To 100
      For J = 1 To 100
        If I = TDA And J = TDB Then
        dblMatrix (I, J) = dblMatrix (I, J) + 1#
        Else: dblMatrix (I, J) = dblMatrix (I, J)
        End If
      Next J
    Next I
  End If
Else
  k1 = (Y1 - Y0) / (X1 - X0)
  k2 = Tan (Phi)
  Alpha = Abs (Atn (Abs ((k2 - k1) / (1 + k1 * k2))))

  Z1 = ((Y1 - Y0) / cy) * cz
  While (Z1 >= 0 And Z1 < (TL - (1 - Sin (Phi) / Tan (Tubeangle))))
    X0 = X1
    Y0 = Y1
    Z0 = Z1
      If k2 >= k1 Then Phi = Phi - pi + 2 * Alpha                 'next renounce
      If k2 < k1 Then Phi = Phi + pi - 2 * Alpha
    X1 = Cos (Phi)
    Y1 = Sin (Phi)
    S1 = Sqr ((Y1 - Y0) ^ 2 + (X1 - X0) ^ 2)
    Z1 = Z0 + Z0 * S1 / S0
    S0 = S1
  Wend
  If Z1 >= (TL - (1 - Sin (Phi) / Tan (Tubeangle))) Then             'GoTo its_thru
     NT = NT + 1
     X2 = X1 + (y + Y1) * cx / cy
     Z2 = (y + Y1) * cz /cy - TL + Z1
     If Z2 <= 0 And AngleofTube.Text = 90 Then                        'GoTo Repeat
     Else
      Imgdemonstration.PSet (Xaxis + X2 * Ratio, Z2 * Ratio + LineLength), RGB (255, 0, 255)
      If (Xaxis + X2 * Ratio) >= Int (Xaxis + X2 * Ratio) Then
        I = CLng (Int ((Xaxis + X2 * Ratio) / XUnit)) + 1
      Else: I = CLng (Int ((Xaxis + X2 * Ratio) / XUnit))
      End If
      If (Z2 * Ratio + LineLength) >= Int (Z2 * Ratio + LineLength) Then
        J = CLng (Int ((Z2 * Ratio + LineLength) / YUnit)) + 1
```

```
          Else: J = CLng (Int ((Z2 * Ratio + LineLength) / YUnit))
          End If
          TDA = I
          TDB = J
          For I = 1 To 100
            For J = 1 To 100
              If I = TDA And J = TDB Then
              dblMatrix (I, J) = dblMatrix (I, J) + 1#
              Else: dblMatrix (I, J) = dblMatrix (I, J)
              End If
            Next J
          Next I
        End If
      End If
    End If
  Next N

  For I = 1 To 100
    For J = 1 To 100
      Select Case dblMatrix (I, J)
        Case Is > Nummolecule.Text * 12 / 50000
          Imgdemonstration.Line (XUnit * I, YUnit * J)-(XUnit * (I + 1), YUnit * (J + 1)), QBColor (14), BF
        Case Nummolecule.Text * 8 / 50000 To Nummolecule.Text * 12 / 50000
          Imgdemonstration.Line (XUnit * I, YUnit * J)-(XUnit * (I + 1), YUnit * (J + 1)), QBColor (2), BF
        Case Nummolecule.Text * 4 / 50000 To Nummolecule.Text * 7 / 50000
          Imgdemonstration.Line (XUnit * I, YUnit * J)-(XUnit * (I + 1), YUnit * (J + 1)), QBColor (4), BF
        Case Nummolecule.Text * 2 / 50000 To Nummolecule.Text * 3 / 50000
          Imgdemonstration.Line (XUnit * I, YUnit * J)-(XUnit * (I + 1), YUnit * (J + 1)), QBColor (8), BF
        Case Else
      End Select
    Next J
  Next I

  Rate = ND / (NT - ND)

    Modistribution.Text = "No. pass directly= " & ND & "total No.= " & NT & _
```

```
    "direct/indirect= " & Rate

End Sub

Private Sub Crosssection_Click ()
Imgdemonstration.Cls                                    'clear the pictures each time
Call Prameter (pi, two_pi, center_x, center_y, TP, BM, R, LE, RE, Cc1, Cc2, TL, Dp, DD, NTT, Xaxis,
Ratio, OX, OY, AA1, BB1, LineLength)

Tubeangle = (AngleofTube.Text) * pi / 180


  Step2 = R / 10
  For Radius = 0 To 20 * R
    Imgdemonstration.Circle (OX, OY), Radius, RGB (0, 255, 0)
    Radius = Radius + Step2
  Next Radius                            ' draw the co-center circle on the vertical projection plane

  NT = 0
  ND = 0



  For N = 1 To NTT
    RM = Sqr (Rnd)
    Theta = two_pi * Rnd
    X0 = RM * Cos (Theta)
    Y0 = RM * Sin (Theta)
    Z0 = 0                                              'staring point position
  Call DCEM (cx, cy, cz)
  A = cx / cy
  B = A * Y0 - X0
  D = -(B / (1 + A * A))
  E = A * Sqr (Abs ((B * B) - (1 + A * A))) / (1 + A * A)
  Phi1 = Atn (-(D + E) / Sqr (-(D + E) * (D + E) + 1)) + 2 * Atn (1)
  Phi2 = Atn (-(D - E) / Sqr (-(D - E) * (D - E) + 1)) + 2 * Atn (1)       'calculate renounce angle
  If Abs (Phi1 - Theta) < pi Then Phi = Phi1
  If Abs (Phi1 - Theta) > pi Then Phi = Phi2
  X1 = Cos (Phi)
  Y1 = Sin (Phi)
  Z1 = ((Y1 - Y0) / cy) * cz
  S0 = Sqr ((Y1 - Y0) ^ 2 + (X1 - X0) ^ 2)
```

```
If Z1 <= 0 Then
  ElseIf Z1 >= (TL - (1 - Sin (Phi) / Tan (Tubeangle))) Then                    'GoTo its_gone
    ND = ND + 1
    NT = NT + 1
    Xp = X0 + (Dp + TL - Z1) * (X1 - X0) / (Z1 - Z0)
    Yp = Y0 + (Dp + TL - Z1) * (Y1 - Y0) / (Z1 - Z0)
    Imgdemonstration.PSet (OX + R * Xp, OY + R * Yp), RGB (0, 0, 255)
  Else
    k1 = (Y1 - Y0) / (X1 - X0)
    k2 = Tan (Phi)
    Alpha = Abs (Atn (Abs ((k2 - k1) / (1 + k1 * k2))))

    Z1 = ((Y1 - Y0) / cy) * cz
    While (Z1 >= 0 And Z1 < (TL - (1 - Sin (Phi) / Tan (Tubeangle))))
      X0 = X1
      Y0 = Y1
      Z0 = Z1
        If k2 >= k1 Then Phi = Phi - pi + 2 * Alpha                             'next renounce
        If k2 < k1 Then Phi = Phi + pi - 2 * Alpha
      X1 = Cos (Phi)
      Y1 = Sin (Phi)
      S1 = Sqr ((Y1 - Y0) ^ 2 + (X1 - X0) ^ 2)
      Z1 = Z0 + Z0 * S1 / S0
      S0 = S1
    Wend
    If Z1 >= (TL - (1 - Sin (Phi) / Tan (Tubeangle))) Then                      'GoTo its_thru
       NT = NT + 1
       Xp = X0 + (Dp + TL - Z1) * (X1 - X0) / (Z1 - Z0)
       Yp = Y0 + (Dp + TL - Z1) * (Y1 - Y0) / (Z1 - Z0)
       Imgdemonstration.PSet (OX + R * Xp, OY + R * Yp), RGB (255, 0, 255)
       End If
    End If
Next N

Rate = ND / (NT - ND)

  Modistribution.Text = "No. pass directly= " & ND & "total No.= " & NT & _
  "direct/indirect= " & Rate

End Sub
```

```
Private Sub Form_Load ()
'Initialize the text windows

'Color the form to look nice
FadeForm Me, True, False, True

LentoRad.Text = 10#                                   'default length to radius
Nummolecule.Text = 50000                              'default trajectory value
OutDistance.Text = 10#                    'default distance between outer tube and interested plane
Modistribution.Text = "MD simulation of gas flow in a cylinder"
ProjectionDistance.Text = 2#                   'default the distance from tube axis to projection plane
AngleofTube.Text = 30#                           'default the angle of the slope of the tube

End Sub

Private Sub Numdistribution_Click ()
Imgdemonstration.Cls                                      'clear the pictures each time
Call Prameter (pi, two_pi, center_x, center_y, TP, BM, R, LE, RE, Cc1, Cc2, TL, Dp, DD, NTT, Xaxis,
Ratio, OX, OY, AA1, BB1, LineLength)

Tubeangle = (AngleofTube.Text) * pi / 180

NT = 0                        '
ND = 0

  Step3 = R / 100
  For I = 1 To 2000
  number (I) = 0
  Next                                               'pre-set the step of co-center circle

  For N = 1 To NTT
    RM = Sqr (Rnd)
    Theta = two_pi * Rnd
    X0 = RM * Cos (Theta)
    Y0 = RM * Sin (Theta)
    Z0 = 0                                            'staring point position
  Call DCEM (cx, cy, cz)
  A = cx / cy
  B = A * Y0 - X0
  D = -(B / (1 + A * A))
```

```
E = A * Sqr (Abs ((B * B) - (1 + A * A))) / (1 + A * A)
Phi1 = Atn (-(D + E) / Sqr (-(D + E) * (D + E) + 1)) + 2 * Atn (1)
Phi2 = Atn (-(D - E) / Sqr (-(D - E) * (D - E) + 1)) + 2 * Atn (1)            'calculate renounce angle
If Abs (Phi1 - Theta) < pi Then Phi = Phi1
If Abs (Phi1 - Theta) > pi Then Phi = Phi2
X1 = Cos (Phi)
Y1 = Sin (Phi)
Z1 = ((Y1 - Y0) / cy) * cz
S0 = Sqr ((Y1 - Y0) ^ 2 + (X1 - X0) ^ 2)
If Z1 <= 0 Then
  ElseIf Z1 >= (TL - (1 - Sin (Phi) / Tan (Tubeangle))) Then 'GoTo its_gone
    ND = ND + 1
    NT = NT + 1
    Xp = X0 + (Dp + TL - Z1) * (X1 - X0) / (Z1 - Z0)
    Yp = Y0 + (Dp + TL - Z1) * (Y1 - Y0) / (Z1 - Z0)
    I = Int (Sqr (Xp * Xp + Yp * Yp) * R / Step3)
    If I < 1 Then I = 1
    number (I) = number (I) + 1#
  Else
    k1 = (Y1 - Y0) / (X1 - X0)
    k2 = Tan(Phi)
    Alpha = Abs (Atn (Abs ((k2 - k1) / (1 + k1 * k2))))

    Z1 = ((Y1 - Y0) / cy) * cz
    While (Z1 >= 0 And Z1 < (TL - (1 - Sin (Phi) / Tan (Tubeangle))))
      X0 = X1
      Y0 = Y1
      Z0 = Z1
        If k2 >= k1 Then Phi = Phi - pi + 2 * Alpha                          'next renounce
        If k2 < k1 Then Phi = Phi + pi - 2 * Alpha
      X1 = Cos (Phi)
      Y1 = Sin (Phi)
      S1 = Sqr ((Y1 - Y0) ^ 2 + (X1 - X0) ^ 2)
      Z1 = Z0 + Z0 * S1 / S0
      S0 = S1
    Wend
    If Z1 >= (TL - (1 - Sin (Phi) / Tan (Tubeangle))) Then                    'GoTo its_thru
      NT = NT + 1
      Xp = X0 + (Dp + TL - Z1) * (X1 - X0) / (Z1 - Z0)
      Yp = Y0 + (Dp + TL - Z1) * (Y1 - Y0) / (Z1 - Z0)
```

```
            I = Int (Sqr (Xp * Xp + Yp * Yp) * R / Step3)
            If I < 1 Then I = 1
            number (I) = number (I) + 1#
        End If
      End If
   Next N

   Rate = ND / (NT - ND)

      Modistribution.Text = "No. pass directly= " & ND & "total No.= " & NT & _
      "direct/indirect= " & Rate

   For I = 1 To 2000
      Imgdemonstration.PSet (I * 10 + 200, Imgdemonstration.ScaleHeight - number(I) * 100 * 7500 / NTT
- 100)
   Next

End Sub

Private Sub ParticleDistribution_Click ()
Imgdemonstration.Cls                                                   'clear the pictures each time

   Dim Xellipse, Yellipse
   Call Prameter (pi, two_pi, center_x, center_y, TP, BM, R, LE, RE, Cc1, Cc2, TL, Dp, DD, NTT, Xaxis,
Ratio, OX, OY, AA1, BB1, LineLength)
   Tubeangle = (AngleofTube.Text) * pi / 180

   Xellipse = Xaxis
   Yellipse = LineLength - Ratio / Tan (Tubeangle)

   Imgdemonstration.Line (AA1, 0)-(AA1, Yellipse), RGB (0, 0, 255)
   Imgdemonstration.Line (BB1, 0)-(BB1, Yellipse), RGB (0, 0, 255)
   If AngleofTube.Text = 90 Then
      Imgdemonstration.Line (AA1, LineLength)-(BB1, LineLength), RGB (0, 0, 255)
   ElseIf Tan (Tubeangle) >= 1 Then
      FillStyle = 1
      Imgdemonstration.Circle (Xellipse, Yellipse), Ratio, , , , 1 / Tan(Tubeangle)     'Draw a hollow ellipse
   Else: FillStyle = 1
      Imgdemonstration.Circle (Xellipse, Yellipse), Ratio / Tan (Tubeangle), , , , 1 / Tan(Tubeangle)   'Draw
a hollow ellipse
```

```
End If

y = DD + 1                                                     'Give the initial value
NT = 0
ND = 0

For N = 1 To NTT
      RM = Sqr (Rnd)
      Theta = two_pi * Rnd
      X0 = RM * Cos (Theta)
      Y0 = RM * Sin (Theta)
      Z0 = 0                                                   'staring point position

   Call DCEM(cx, cy, cz)
   A = cx / cy
   B = A * Y0 - X0
   D = -(B / (1 + A * A))
   E = A * Sqr (Abs ((B * B) - (1 + A * A))) / (1 + A * A)
   Phi1 = Atn (-(D + E) / Sqr (-(D + E) * (D + E) + 1)) + 2 * Atn (1)
   Phi2 = Atn (-(D - E) / Sqr (-(D - E) * (D - E) + 1)) + 2 * Atn (1)       'calculate renounce angle
      If Abs (Phi1 - Theta) < pi Then Phi = Phi1                 'Determine the renounce angle
      If Abs (Phi1 - Theta) >= pi Then Phi = Phi2
   X1 = Cos (Phi)
   Y1 = Sin (Phi)
   Z1 = ((Y1 - Y0) / cy) * cz
   S0 = Sqr ((Y1 - Y0) ^ 2 + (X1 - X0) ^ 2)
   If Z1 <= 0 Then
   ElseIf Z1 >= (TL - (1 - Sin (Phi) / Tan (Tubeangle))) Then            'GoTo its_gone
      ND = ND + 1
      NT = NT + 1
      X2 = X1 + (y + Y1) * cx / cy
      Z2 = (y + Y1) * cz / cy- TL + Z1
      If Z2 <= 0 And AngleofTube.Text = 90 Then                  'GoTo Repeat
      Else
      Imgdemonstration.PSet (Xaxis + X2 * Ratio, Z2 * Ratio + LineLength), RGB (0, 0, 255)
      End If
   Else
      k1 = (Y1 - Y0) / (X1 - X0)
      k2 = Tan (Phi)
      Alpha = Abs (Atn (Abs ((k2 - k1) / (1 + k1 * k2))))
```

```
         Z1 = ((Y1 - Y0) / cy) * cz
        While (Z1 >= 0 And Z1 < (TL  - (1 – Sin (Phi) / Tan(Tubeangle))))
           X0 = X1
           Y0 = Y1
           Z0 = Z1
              If k2 >= k1 Then Phi = Phi - pi + 2 * Alpha                    'next renounce
              If k2 < k1 Then Phi = Phi + pi - 2 * Alpha
           X1 = Cos (Phi)
           Y1 = Sin (Phi)
           S1 = Sqr((Y1 - Y0) ^ 2 + (X1 - X0) ^ 2)
           Z1 = Z0 + Z0 * S1 / S0
           S0 = S1
         Wend
         If Z1 >= (TL - (1 – Sin (Phi) / Tan (Tubeangle))) Then                 'GoTo its_thru
             NT = NT + 1
             X2 = X1 + (y + Y1) * cx / cy
            Z2 = (y + Y1) * cz / cy - TL + Z1
             If Z2 <= 0 And AngleofTube.Text = 90 Then                        'GoTo Repeat
             Else
               Imgdemonstration.PSet (Xaxis + X2 * Ratio, Z2 * Ratio + LineLength), RGB (255, 0, 255)
             End If
         End If
      End If
   Next N

   Rate = ND / (NT - ND)

      Modistribution.Text = "No. pass directly= " & ND & "total No.= " & NT & _
      "direct/indirect= " & Rate

End Sub

Private Sub Predistribution_Click ()
Imgdemonstration.Cls                                              'clear the pictures each time
Call Prameter (pi, two_pi, center_x, center_y, TP, BM, R, LE, RE, Cc1, Cc2, TL, Dp, DD, NTT, Xaxis,
Ratio, OX, OY, AA1, BB1, LineLength)

Tubeangle = (AngleofTube.Text) * pi / 180
```

```
NT = 0
ND = 0

Step3 = R / 100
For I = 1 To 2000
number (I) = 0
Next                                                    'pre-set the step of co-center circle



For N = 1 To NTT
  RM = Sqr (Rnd)
  Theta = two_pi * Rnd
  X0 = RM * Cos (Theta)
  Y0 = RM * Sin (Theta)
  Z0 = 0                                                    'staring point position

Call DCEM (cx, cy, cz)
A = cx / cy
B = A * Y0 - X0
D = -(B / (1 + A * A))
E = A * Sqr (Abs ((B * B) - (1 + A * A))) / (1 + A * A)
Phi1 = Atn (-(D + E) / Sqr (-(D + E) * (D + E) + 1)) + 2 * Atn (1)
Phi2 = Atn (-(D - E) / Sqr (-(D - E) * (D - E) + 1)) + 2 * Atn (1)          'calculate renounce angle
If Abs (Phi1 - Theta) < pi Then Phi = Phi1
If Abs (Phi1 - Theta) > pi Then Phi = Phi2
X1 = Cos (Phi)
Y1 = Sin (Phi)
Z1 = ((Y1 - Y0) / cy) * cz
S0 = Sqr ((Y1 - Y0) ^ 2 + (X1 - X0) ^ 2)
  If Z1 <= 0 Then
  ElseIf Z1 >= (TL - (1 – Sin (Phi) / Tan (Tubeangle))) Then               'GoTo its_gone
    ND = ND + 1
    NT = NT + 1
    Xp = X0 + (Dp + TL - Z1) * (X1 - X0) / (Z1 - Z0)
    Yp = Y0 + (Dp + TL - Z1) * (Y1 - Y0) / (Z1 - Z0)
    I = Int (Sqr (Xp * Xp + Yp * Yp) * R / Step3)
    If I < 1 Then I = 1
    Number (I) = number (I) + 1#
  Else
    k1 = (Y1 - Y0) / (X1 - X0)
```

```
      k2 = Tan (Phi)
      Alpha = Abs (Atn (Abs ((k2 - k1) / (1 + k1 * k2))))

      Z1 = ((Y1 - Y0) / cy) * cz
      While (Z1 >= 0 And Z1 < (TL  - (1 – Sin (Phi) / Tan (Tubeangle))))
        X0 = X1
        Y0 = Y1
        Z0 = Z1
          If k2 >= k1 Then Phi = Phi - pi + 2 * Alpha                    'next renounce
          If k2 < k1 Then Phi = Phi + pi - 2 * Alpha
        X1 = Cos (Phi)
        Y1 = Sin (Phi)
        S1 = Sqr((Y1 - Y0) ^ 2 + (X1 - X0) ^ 2)
        Z1 = Z0 + Z0 * S1 / S0
        S0 = S1
      Wend
      If Z1 >= (TL - (1 – Sin (Phi) / Tan (Tubeangle))) Then                  'GoTo its_thru
        NT = NT + 1
        Xp = X0 + (Dp + TL  - Z1) * (X1 - X0) / (Z1 - Z0)
        Yp = Y0 + (Dp + TL  - Z1) * (Y1 - Y0) / (Z1 - Z0)
        I = Int (Sqr (Xp * Xp + Yp * Yp) * R / Step3)
        If I < 1 Then I = 1
        Number(I) = number (I) + 1#
      End If
    End If
  Next N

  Rate = ND / (NT - ND)

    Modistribution.Text = "No. pass directly= " & ND & "total No.= " & NT & _
    "direct/indirect= " & Rate

  For I = 1 To 2000
    Pressure (I) = number (I) / (pi * (2 * I - 1) * Step3 * Step3)
  Next

  For I = 1 To 2000
    Imgdemonstration.PSet (I * 10 + 200, Imgdemonstration.ScaleHeight – pressure (I) * 4000000 *
10000 / NTT - 100)
  Next
```

```
End Sub


Private Sub Projection_Click()
Imgdemonstration.Cls
Call Prameter (pi, two_pi, center_x, center_y, TP, BM, R, LE, RE, Cc1, Cc2, TL, Dp, DD, NTT, Xaxis,
Ratio, OX, OY, AA1, BB1, LineLength)

Tubeangle = (AngleofTube.Text) * pi / 180

Imgdemonstration.Line (LE, TP)-(RE, BM), , B                          'outshape of tube in pic1
Imgdemonstration.Circle (Cc1, Cc2), R, RGB (255, 0, 0)                 'draw circle in pic1
NT = 0                              '
ND = 0



  For N = 1 To NTT
    RM = Sqr (Rnd)
    Theta = two_pi * Rnd
    X0 = RM * Cos (Theta)
    Y0 = RM * Sin (Theta)
    Z0 = 0                                                           'staring point position
  Call DCEM (cx, cy, cz)
  A = cx / cy
  B = A * Y0 - X0
  D = -(B / (1 + A * A))
  E = A * Sqr (Abs ((B * B) - (1 + A * A))) / (1 + A * A)
  Phi1 = Atn (-(D + E) / Sqr (-(D + E) * (D + E) + 1)) + 2 * Atn (1)
  Phi2 = Atn (-(D - E) / Sqr (-(D - E) * (D - E) + 1)) + 2 * Atn (1)        'calculate renounce angle
  If Abs (Phi1 - Theta) < pi Then Phi = Phi1
  If Abs (Phi1 - Theta) > pi Then Phi = Phi2
  X1 = Cos (Phi)
  Y1 = Sin (Phi)
  Z1 = ((Y1 - Y0) / cy) * cz
  S0 = Sqr ((Y1 - Y0) ^ 2 + (X1 - X0) ^ 2)
  If Z1 <= 0 Then
    ElseIf Z1 >= (TL - (1 – Sin (Phi) / Tan (Tubeangle))) Then                'GoTo its_gone
      ND = ND + 1
      NT = NT + 1
```

```
      Imgdemonstration.Line (Cc1 + X0 * R, Cc2 - Y0 * R)-(Cc1 + X1 * R, Cc2 - Y1 * R), RGB (0, 255,
255)
      Imgdemonstration.Line (LE + Z0 * R, Cc2 - Y0 * R)-(LE + Z1 * R, Cc2 - Y1 * R), RGB (0, 0, 255)

    Else
      k1 = (Y1 - Y0) / (X1 - X0)
      k2 = Tan (Phi)
      Alpha = Abs (Atn (Abs((k2 - k1) / (1 + k1 * k2))))

      Z1 = ((Y1 - Y0) / cy) * cz
      While (Z1 >= 0 And Z1 < (TL  - (1 – Sin (Phi) / Tan (Tubeangle))))
        X0 = X1
        Y0 = Y1
        Z0 = Z1
          If k2 >= k1 Then Phi = Phi - pi + 2 * Alpha                        'next renounce
          If k2 < k1 Then Phi = Phi + pi - 2 * Alpha
        X1 = Cos (Phi)
        Y1 = Sin (Phi)
        S1 = Sqr ((Y1 - Y0) ^ 2 + (X1 - X0) ^ 2)
        Z1 = Z0 + Z0 * S1 / S0
        S0 = S1
        Imgdemonstration.Line (Cc1 + X0 * R, Cc2 - Y0 * R)-(Cc1 + X1 * R, Cc2 - Y1 * R), RGB (0,
255, 255)
        Imgdemonstration.Line (LE + Z0 * R, Cc2 - Y0 * R)-(LE + Z1 * R, Cc2 - Y1 * R), RGB (0, 0,
255)
      Wend
      If Z1 >= (TL - (1 – Sin (Phi) / Tan(Tubeangle))) Then                  'GoTo its_thru
        NT = NT + 1
        Imgdemonstration.Line (Cc1 + X0 * R, Cc2 - Y0 * R)-(Cc1 + X1 * R, Cc2 - Y1 * R), RGB (0,
255, 255)
        Imgdemonstration.Line (LE + Z0 * R, Cc2 - Y0 * R)-(LE + Z1 * R, Cc2 - Y1 * R), RGB (0, 0,
255)
      End If
    End If
  Next N

  Rate = ND / (NT - ND)

    Modistribution.Text = "No. pass directly= " & ND & "total No.= " & NT & _
    "direct/indirect= " & Rate
```

```
End Sub

Public Sub DCEM (cx, cy, cz)
cz = Sqr (Rnd)
AA = Sqr (1 - cz * cz)
BB = 2 * pi * Rnd
cx = AA * Cos (BB)
cy = AA * Sin (BB)
If cy = 0 Then
cy = 0.00001
End If
End Sub

Private Sub FadeForm (frm As Form, Red%, Green%, Blue%)
Dim SaveScale%, SaveStyle%, SaveRedraw%
Dim I&, J&, X&, y&, pixels%

'save current settings
SaveScale = frm.ScaleMode
SaveStyle = frm.DrawStyle
SaveRedraw = frm.AutoRedraw

'Paint screen
frm.ScaleMode = 3
pixels = Screen.Height / Screen.TwipsPerPixelY
X = pixels / 64# + 0.5
frm.DrawStyle = 5
frm.AutoRedraw = True
For J = 0 to pixels Step X
  y = 240 - 245 * J / pixels
    'Can tweak if required
    If y < 0 Then y = 0
    'Error trap
    frm.Line (-2, J - 2)-(Screen.Width + 2, J + X + 3), RGB (-Red * y, -Green * y, -Blue * y), BF
Next J

'Reset previous settings
frm.ScaleMode = SaveScale
frm.DrawStyle = SaveStyle
```

```
frm.AutoRedraw = SaveRedraw

End Sub

Private Sub Prameter (pi, two_pi, center_x, center_y, TP, BM, R, LE, RE, Cc1, Cc2, TL, Dp, DD, NTT,
Xaxis, Ratio, OX, OY, AA1, BB1, LineLength)
pi = 355 / 113
two_pi = 2 * pi                                 'dim the constant
center_x = Imgdemonstration.ScaleWidth / 2
center_y = Imgdemonstration.ScaleHeight / 2
TP = 0.6 * center_y
BM = 1.4 * center_y
R = (BM - TP) / 2
LE = 1# * center_x
RE = LE + TL * R
Cc1 = 0.5 * center_x
Cc2 = TP + R
TL = Val (LentoRad.Text)
Dp = Val (OutDistance.Text)                        'pre-set values
DD = Val (ProjectionDistance.Text)
NTT = Val (Nummolecule.Text)
Xaxis = Imgdemonstration.ScaleWidth / 2
Ratio = 200
OX = Imgdemonstration.ScaleWidth / 2
OY = Imgdemonstration.ScaleHeight / 2
AA1 = Xaxis - Ratio
BB1 = Xaxis + Ratio
LineLength = 800

End Sub
```

VITA

Xiaohu Tang was born in Chengdu, China on December 28, 1974. He graduated from *Huaiyuan High School*, in Sichuan, China in 1992; in the same year he entered the *Materials Science & Engineering* Department at the *Beijing University of Aeronautics & Astronautics* (BUAA), in Beijing, from which he received his bachelor and master degrees in 1996 and 2000 respectively. Meanwhile, Xiaohu established solid material science and engineering background and oriented his research interest toward the applications of electron microscopy.

In fall of 2000 he was admitted to the Metallurgical Engineering Ph.D. program in the *Materials Science and Engineering* Department at the *University of Tennessee, Knoxville* and joined Dr. David C. Joy's research team. Since then he has been involving in the field of the charging behavior on the surface of insulator and semiconductor in the presence of a gaseous environment. His research was recognized in 2002 with the presidential student award of the *Microscopy Society of America.* Xiaohu Tang has published paper in Scanning and poster presentations to conferences. He will graduate from the *University of Tennessee* in August 2004 with a Ph.D. degree in *Materials Science and Engineering.*